FACULTY OF TECHNOLOGY

DETERMINATION OF FRACTURE BEHAVIOR OF UHSS STEELS AT LOW TEMPERATURES

Anna Sipola

DEGREE PROGRAMME IN MECHANICAL ENGINEERING

Master's thesis

May 2023

ABSTRACT

Determination of fracture behavior of UHSS steels at low temperatures

Anna Sipola

University of Oulu, Degree Programme in Mechanical Engineering

Master's thesis 2023, 104 pp.

Supervisors at the university: Olli Nousiainen and Sakari Pallaspuro

Structural life and failure probability assessment has become increasingly common practice in modern structural engineering, when attempting to optimize the overall costs and service reliability of engineered structures. For same reasons, the use of ultrahigh-strength steels (UHSS) has also become more common in structural engineering. Lack of research, as well as relevant design and fabrication guidelines have however limited the applications of UHSS steels as structural engineering materials. In this thesis, aspects of fracture mechanical testing were examined for purposes of productizing the fracture toughness testing method considered. The theoretical background of fracture mechanics and the most essential testing standards were reviewed and fracture toughness of two ultrahigh-strength, quenched and tempered martensitic steels at low temperature were determined. Selected fracture toughness parameters were the crack-tip opening displacement and the ductile-to-brittle transition reference temperature. Fracture surface examinations were carried out with scanning electron microscope imaging. The studied tool steel was found to behave structurally brittle while the studied stainless steel behaved structurally ductile in the fracture toughness tests. Based on the standards and theory addressed in this work, working instructions for fracture toughness testing as well as spreadsheets for parameter calculations, and for determination of uncertainties of testing for one of the parameters, were prepared for productization of the test method.

Keywords: fracture mechanics, fracture toughness, ultrahigh-strength steel, crack-tip opening displacement, Master Curve, fracture toughness testing standard

TIIVISTELMÄ

UHSS terästen murtumiskäyttäytymisen määrittäminen matalissa lämpötiloissa

Anna Sipola

Oulun yliopisto, Konetekniikan tutkinto-ohjelma

Diplomityö 2023, 104 s.

Työn ohjaajat yliopistolla: Olli Nousiainen ja Sakari Pallaspuro

Rakenteiden käyttöiän sekä vioittumistodennäköisyyksien arvioinnit ovat käytäntönä entistä yleistyneempiä optimoitaessa rakenteiden kokonaiskustannuksia sekä huoltovarmuutta nykyaikaisessa rakennesuunnittelussa. Samoista syistä myös ultralujien terästen (UHSS) käyttö on yleistynyt rakennesuunnittelussa. Tutkimuksen sekä asiaankuuluvien suunnittelu- ja valmistusohjeiden puute on kuitenkin rajoittanut UHSS-terästen soveltamista materiaaleina rakennesuunnittelussa. Tässä diplomityössä perehdyttiin murtumismekaaniseen testaukseen murtumissitkeysmittausmenetelmän tuotteistamista varten. Työssä tarkasteltiin murtumismekaniikan teoreettista taustaa ja tärkeimpiä testausstandardeja, sekä määritettiin murtositkeys kahdelle ultralujalle, nuorrutetulle martensiittiselle teräkselle matalassa lämpötilassa. Valitut murtumissitkeysparametrit olivat särön kärjen avauma sekä sitkeä-hauras-siirtymän referenssilämpötila. Murtopintatutkimukset suoritettiin pyyhkäisyelektronimikroskoopilla. Työssä tutkitun työkaluteräksen havaittiin käyttäytyvän murtumissitkeys kokeissa hauraasti, tutkitun ruostumattoman teräksen puolestaan sitkeästi. Työssä tarkasteltujen standardien sekä teorian pohjalta laadittiin testausmenetelmän tuotteistamista varten työohje murtositkeystestauksen suorittamiselle sekä laskentataulukot murtumisparametrien laskentaa ja erään parametrin mittaepävarmuuden määrittämistä varten.

Asiasanat: murtumismekaniikka, murtumissitkeys, ultraluja teräs, särön kärjen avauma, Master Curve, standardi murtumissitkeyden määrittämiseksi

PREFACE

This Master's thesis was done as a collaboration between the University of Oulu and DEKRA Industrial Oy, as a part of DEKRA's objective to productize the fracture toughness testing procedure, and was carried out during the period of May 2022 till May in 2023. The work was conducted as a literature review, addressing the theoretical background of fracture mechanics and enlightening some aspects of the most common standardized fracture toughness testing procedures, combined with an experimental part, where fracture behavior of two ultrahigh-strength steels at low temperature were examined.

I wish to express my gratitude to DEKRA and to Prof. Jukka Kömi for providing me with this thesis opportunity. I also wish to express my gratitude to my supervisors, Sr. Lect. Olli Nousiainen and Dr. Sakari Pallaspuro at the university, and DI Jani Kantola at DEKRA, for their contribution, guidance and patience throughout this thesis. I would also like to thank DI Johannes Sainio, Mr. Ilpo Saarela and Mr. Tun Tun Nyo for guidance and help in laboratory work. And finally, I wish to thank my family, especially Toni who has had the delight of putting up with my endless rant on about things he probably could not care less about, for their great patience and support.

Oulu, 31.05.2023

Anna Sipola

TABLE OF CONTENTS

LIST OF SYMBOLS AND ABBREVIATIONS

1T	a standard size, 1 inch or 25,4 mm thick, specimen
A	crack area
A_m	stress amplitude for the *m*th term
a	crack length
a_0	initial crack length
a_f	final physical crack length
B	specimen thickness
b	specimen ligament length
ASTM	American Society for Testing and Materials
BCC	body-centered cubic
C	compliance
C_{exp}	experimental compliance
C_{theo}	theoretical elastic compliance
C_m	system compliance
ch.	chapter
CMOD	crack mouth opening displacement V
CT	compact tension
CTOA	crack-tip opening angle
CTOD	crack-tip opening displacement
DCG	double clip gage
DC(T)	disc-shaped compact
E	Young's modulus
e.g.	exempli gratia, for example
EPFM	elastic-plastic fracture mechanics
FCC	face-centered cubic lattice
FEM	finite element analyses
F_{fmax}	maximum fatigue force
F_{fmin}	minimum fatigue force
F_{max}	maximum force
FM	fracture mechanics
FT	fracture toughness
G	energy release rate, crack extension force, crack driving force

G_c	critical value of G, a measure of fracture toughness
HCP	hexagonal close-packed
HRR	proportionality of stress and strain distributions at the crack-tip, named after Hutchinson, Rice and Rosengren
i.e.	id est, that is
IfEP	Institut für Eignungsprüfung GmbH
ISO	International Institute of Standards
J	path independent contour integral around a crack, a measure of fracture toughness
J_c	J at onset of unstable crack extension or pop-in without prior significant stable crack extension
J_i	J at initiation of stable crack extension
J_{Ic}	J at 0,2 mm stable crack extension offset, an engineering parameter
J_m	J at the first attainment of maximum force plateau for fully plastic behavior
J_u	J at onset of unstable crack extension or pop-in after stable crack extension
J_{uc}	J at onset of unstable crack extension or pop-in when stable crack extension cannot be measured
$J_{0,2BL}$	J at 0,2 mm stable crack extension offset, an engineering parameter
JWES	Japan Welding Engineering Society (standards designated with WES)
K	stress intensity factor
K_0	Weibull fitting parameter, a scale parameter located at the 63,2% cumulative failure probability level
K_c	critical value of K, a measure of fracture toughness
K_{Ic}	plane strain fracture toughness, mode I loading
K_{Jc}	elastic-plastic equivalent critical stress intensity factor derived from J-integral at the point of onset of cleavage fracture J_c
$K_{Jc(1T)}$	size-adjusted elastic-plastic equivalent critical stress intensity factor
$K_{Jc(med)}$	median toughness for a data set
k	proportionality constant
L	longitudinal rolling direction of a plate
LEFM	linear elastic fracture mechanics
m	constrain factor
MC	Master Curve
NDTT	nil-ductility transition temperature

P	load
QT	quenched and tempered
R	resistance curve or a ratio of minimum-to-maximum force in fatigue cycle
$R_{p0,2}$	yield strength
R_m	ultimate tensile strength
r	distance from the crack-tip or a dimensionless constant, rotational factor
r_p	plastic rotational factor
r_y	displacement behind the effective crack-tip
S	span between outer loading points in a three-point bend test or short/normal direction of a plate
SEM	scanning electron microscopy
SENB	single-edge-notched bend
SRC	silicone rubber casting impression method
SZW	stretch zone width
T	transverse direction of a plate
T_0	ductile-to-brittle transition reference temperature
U	strain energy
U_c	absorbed energy
u_y	crack-tip opening displacement from crack plane, half of CTOD
UHSS	ultrahigh-strength steel
V	crack mouth opening displacement
W	specimen width
w_f	fracture energy
W_s	work required to create new surfaces
Y	correction factor for K, a dimensionless constant which depends on the geometry and the mode of loading
γ_s	surface energy per unit area
Δ	displacement or change
δ	crack-tip opening displacement
δ_c	δ at onset of unstable crack extension or pop-in without prior significant stable crack extension
δ_{el}	elastic component of crack-tip opening displacement
δ_i	δ at initiation of stable crack extension
δ_{Ic}	δ at 0,2 mm stable crack extension offset, an engineering parameter

δ_m	δ at the first attainment of maximum force plateau for fully plastic behavior
δ_{pl}	plastic component of crack-tip opening displacement
δ_u	δ at onset of unstable crack extension or pop-in after stable crack extension
δ_{uc}	δ at onset of unstable crack extension or pop-in when stable crack extension cannot be measured
$\delta_{0,2BL}$	δ at 0,2 mm stable crack extension offset, an engineering parameter
ε_{zz}	component of strain in z-direction
η	plastic geometry factor for J calculation
θ	angle from the crack plane
Π	potential energy supplied by internal strain energy and external forces
ρ	crack-tip radius
σ	remote stress
σ_c	theoretical cohesive strength
σ_e	effective stress at the plastic zone boundary
σ_f	theoretical fracture strength of a crystalline solid
σ_{xx}	component of stress in x-direction
σ_{YS}	yield strength
σ_{yy}	component of stress in y-direction
σ_{zz}	component of stress in z-direction

1 INTRODUCTION

Over the years, structural life and failure probability assessment has become increasingly common practice while assessing and optimizing the overall costs of engineered structure all the way from production to service and maintenance, and to the end of service life. This development has been further accelerated by the ever-growing need to produce more economical, more durable, reliable, and easier-to-maintain structures in order to meet the present-day challenges, such as those set by ever-spanning material and energy consumption, lessening availability and rising cost of natural sources, e.g. alloying elements, as well as the rapidly changing climate, i.e. the need to reduce CO_2-emissions related to manufacture and service life of structures. (Lipiäinen 2021, p. 1; Tomerlin et al. 2022, p. 2)

Also, to tackle the aforementioned challenges, as well as the technical challenges presented by constant scientific and technological advances, a wide range of materials with enhanced properties better suited for demands of modern structural design have been developed over the years and are widely adopted for structural engineering today. For this reason, the use of ultrahigh-strength steels (UHSS) has also become more common. (Heidarpour et al. 2014, p. 27; Ribeiro et al. 2021, p. 1) On the downside, UHSS steels tend to have lower ductility and have been reported to be more prone to fatigue, than more conventional structural steels, especially in the presence of flaws, and thus require a more accurate prediction of failure (Trondl & Sun 2015, p. 1; MacKenzie et al. 1977, p. 167; Pijpers et al. 2009, p. 14 – 16). Although these materials have been available by the steel industry for many years and the greater strength to weight ratio does enable the design of lighter and more durable steel structures, applications of UHSS steels as structural engineering materials have currently remain limited due to the lack of research, as well as relevant design and fabrication guidelines, supporting the use of these materials. The use of UHHSs has undoubtedly also been limited by their rather poorly documented fracture properties compared to more conventional steels covered by the codes (Wallin et al. 2015, p. 219).

The total structural life refers to a period which spans over the whole structural service time, including a crack initiation phase, followed by a phase of crack growth, till the time a crack eventually reaches a critical dimension and a sudden failure of the structure occurs. From a failure assessment viewpoint, the crack initiation phase falls within the

domain of fatigue investigations, while the crack growth is determined by the principles of fracture mechanics (FM) (Tomerlin et al. 2022, p. 2). Practically all engineering structures contain at least some pre-existing flaws that can act as triggers for failure, hence the need for determining valid criterions for fracture is relevant. In traditional fracture mechanics the failure criterion for precracked structure is formulated in terms of parameters, such as stress intensity factor K, J-integral and crack-tip opening displacement (CTOD, δ), that characterize the stress field in the vicinity of the crack (Kanvinde 2016, pp. 3 – 4). These parameters can then be employed in structural integrity and failure probability assessments, damage tolerance designs, fitness-for-service evaluation and residual strength analysis, e.g. for determination of a critical crack size for fracture or for fatigue or service life calculations, and can as well serve as a basis in material characterization, performance evaluation and quality assurance for typical engineering structures, such as nuclear power vessels and piping, petrochemical vessels and tanks, oil and gas pipelines, and automotive, ship and aircraft structures (Zhu & Joyce 2012, pp. 4).

Over the years many organizations throughout the world, such as American Society for Testing and Materials (ASTM) and International Institute of Standards (ISO), have presented a variety of standardized procedures for determining different fracture toughness parameters for metallic materials. From the parameters covered by the standards the stress intensity factor K (or its equivalent the energy release rate G), the J-integral, the crack-tip opening displacement (CTOD, δ), and the crack-tip opening angle (CTOA) are the most important and used in fracture mechanics (Zhu & Joyce 2012, p. 4). The parameters K ja J which describe the intensity of the singular crack-tip stress fields in elastic and elastic-plastic materials, respectively, provide a more mathematical approach for characterizing fracture behavior, whereas CTOD and CTOA offer more physical representations of FT. Studies conducted earlier (Presno-Vélez et al. 2019; Newman et al. 2002) suggest CTOD to be the most suited parameter for modeling stable crack growth and instability during the fracture process. In a study conducted by Vasco-Olmo et al. (2019) CTOD was also found to be a valid tool for characterizing fatigue crack growth rate. Thus it can also be valuable for examining UHSS structures, where the assessment of FT under cyclic loading is of especially great importance, since the absolute and relative stress variations under fatigue loading will be higher in UHSS structures compared to those in structures made of lower grade steels (Pijpers et al. 2007, p. 16).

Until quite recently, the formulae for determining fracture parameters presented in standards have fit rather poorly for heavily strain hardening steels and have provided unconservative values for FT, while for intermediate and low strain hardening steels, such as UHSS, same formulas tend to yield overly conservative values. However, also the standards go through revisions and evolve constantly as more knowledge and experience is gained. In the latest editions of standards ISO 12135:2021 and ISO 15653:2018, a formula for calculation of CTOD better suited for strain hardening materials has been adopted. ASTM standard has also been reviewed recently (2022, 2023) but since CTOD evaluation has been approached from different perspective, the same alterations have not been made.

In this work, fracture toughness (FT) of two steels, 1.4313 and a novel medium-carbon steel were investigated. Both of these steels are ultrahigh-strength steels (UHSS) with tensile strengths of about 850 MPa and 1400 MPa nominal, respectively. Both are quenched and tempered and have a martensitic microstructure, but 1.4313 is referred to as a soft martensitic steel while the medium-carbon steel is an engineering and tool steel, with a hardness of about 44 HRC.

The goal of the work was to get familiar with the theory and performance of fracture toughness testing as part of the process aiming to productize fracture toughness testing, and to perform FT measurements for a proficiency test to be participated in. Another objective was to investigate how the two selected steels would behave under quasistatic loading at low temperatures, as this topic did not appear to have been addressed in previous studies, although the materials in some of the proposed applications may well be exposed to such conditions. One more aspect was the need to form an understanding of the key differences between the most commonly used fracture toughness standards.

2 THEORETICAL BACKGROUND

The next chapters focus on viewing the theoretical foundation behind fracture mechanics. The most essential parameters are discussed as well as some fundamental concepts that intrinsically affect fracture mechanic behavior in metals.

Toughness is often defined as the ability of material to absorb energy and is usually characterized by the area under a stress-strain curve for a smooth (unnotched) tension specimen loaded slowly to fracture (Liaw 2000, p. 563). Fracture toughness on the other hand is described as a material's ability to resist crack extension under loading (Zhu & Joyce 2012, p. 4).

The fracture behavior of a metallic material depends on the microscopic fracture tendencies and the strength and deformation behavior of the material, as well as the constraint effect of the geometry of the body (Zhu & Joyce 2012, p. 4). The contribution of these aspects has been attempted to enlighten in the following chapters.

2.1 Materials failure

The terms ductile and brittle are often used to describe both the macroscopic behavior of a structure as well as the fracture micromechanisms. Structurally brittle indicates that fracture occurs without significant plasticity, whereas structurally ductile implies that fracture involves a large amount of plasticity. The term elastic-plastic, in turn, is used to describe structures that exhibit fracture behavior between these two extremes. Structural fracture behavior, however, does not directly indicate the fracture micromechanism. The structural behavior can be brittle although the fracture micromechanism may be ductile, and a brittle fracture micromechanism may result in an elastic-plastic fracture. A fully ductile structural behavior however indicates also a ductile micromechanism. (Wallin 2011, p. 5)

When micromechanisms of fracture are discussed, fractures of engineering materials are broadly categorized as ductile or brittle, but most structural steels can fail in either a ductile or a brittle manner (or both) depending on several conditions such as temperature, loading rate and constraint. (Zhu & Joyce 2012, p. 4; Anderson 2005, p. 247) High temperatures, slow loading rates and low stress constraint promote plastic flow and

consequently ductile microvoid growth and coalescence, whereas low temperatures, high loading rates and high stress constraint hamper plastic flow and increase stress, and hence promote the tendency to brittle cleavage fracture (Kanvinde 2016, p. 2).

2.1.1 Ductile fracture

When a ductile metal is subjected to uniaxial tensile stress and plastic deformation occurs, material loss at the cross-sectional area is first compensated by the strain hardening of the material. Eventually the stress state reaches a point after which strain hardening cannot keep up with the pace of the material loss in the cross-section and a necked region forms.

In ductile materials fractures form through stages of nucleation, growth, and coalescence of microscopic voids that initiate at inclusions, second-phase particles and in the absence of second-phase particles, at blocked slip bands. Void nucleation occurs as a free surface is formed around an inclusion or a second-phase particle either by interface decohesion as a sufficient stress is applied to break the interfacial bonds between the particle and the matrix, or by particle cracking. The details of the stages may vary widely in different materials and with the state of stress during deformation. The fractographic appearance of the final fracture surface is as well influenced by the same factors. In a material where inclusions and second-phase particles are well-bonded to the matrix, void nucleation is often the most critical stage and fracture occurs soon after the voids are formed. Whereas, in a material where void nucleation occurs with little difficulty, fracture properties are controlled by the growth and coalescence of microvoids. (Anderson 2005, pp. 219, 222; Van Stone et al. 1985, p. 158)

Once microvoids have formed, further plastic strain and hydrostatic stress cause the voids to grow through localized plastic deformation. If the initial volume fraction of microvoids is low, that is < 10%, each void can be assumed to grow independently, but as the growing voids reach a critical size relative to their spacing, neighboring microvoids begin to interact as plastic strain is concentrated along the ligaments between adjacent voids, and a local plastic instability (necking) develops between the voids. In real materials voids grow very rapidly when the void fraction reaches 10 to 20%, and the final stage in failure is very abrupt, since fracture occurs with only a minimal increase in the nominal strain. Eventually the growing microvoids coalesce resulting in failure. (Anderson 2005, pp. 219, 222, 230; Van Stone et al. 1985, pp. 164 – 171)

The formation of so-called *cup and cone* fracture surface, figure 1, results from a bimodal or trimodal particle distribution (i.e. a dispersion of different sized particles) and is commonly observed in uniaxial tensile tests. Because of the triaxial stress state in the center of the specimen, void nucleation and growth begin in the center in the larger particles, figure 1 (b). A penny-shaped flaw forms in the center of the specimen as the more closely spaced voids in center parts coalescence upon further strain, figure 1 (c). The penny-shaped flaw produces deformation bands, where the strain is concentrated, at 45° from the tensile axis, figure 1 (d), providing sufficient plasticity to nucleate voids also in the smaller, more numerous particles in the band region, figure 1 (e). The 45° angle between the fracture plane and the applied stress results in a combined Mode I and Mode II loading. Because these small particles are closely spaced, an instability occurs soon after the smaller voids are formed with just a modest increase in strain, resulting in a total fracture of the specimen and the cup and cone appearance of the matching surfaces, figure 1 (f). At low magnifications, the central region of the fracture surface has a fibrous appearance, typical for ductile fractures, but the outer region appears relatively smooth. (Anderson 2005, pp. 222 – 223)

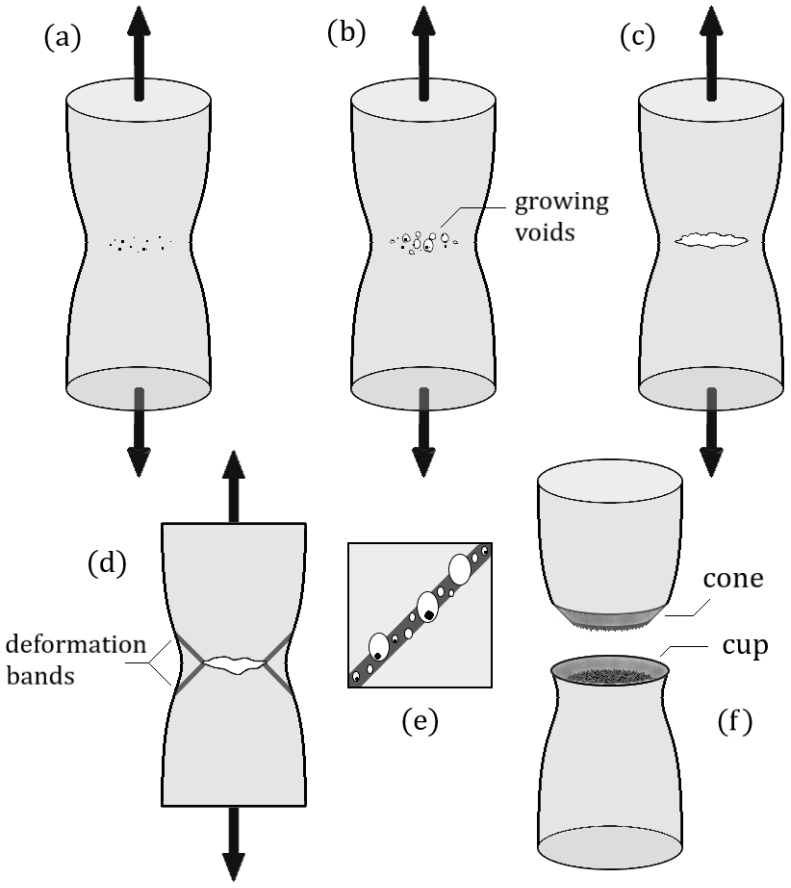

Figure 1. Schematic presentation of the formation of a cup and cone fracture.

Microvoid initiation, growth, and coalescence at the tip of a pre-existing crack is schematically illustrated in figure 2. As a cracked structure is loaded, local stress state at the tip of a crack becomes sufficient to nucleate voids: strain exhibits a singularity near the crack-tip, and stress reaches a peak at a distance of approximately two times the crack-tip opening displacement (CTOD, δ), that is ~2δ. Microvoid nucleation typically occurs when a particle is ~2δ from the crack-tip. Most of the microvoid growth, however, occurs much closer to the crack-tip, relative to CTOD: as the crack blunts, the void's distance from the crack-tip, relative to CTOD, decreases although it remains in approximately fixed place. Also the absolute distance from the crack-tip decreases as the crack grows. After nucleation, microvoids grow as the crack blunts, and eventually link with the main crack. More voids nucleate, grow and coalesce, thus growing the crack, as loading continues. The growth and coalescence of microvoids are usually the critical steps in ductile crack growth. As the ductile microvoid growth and coalescence tends to absorb more energy, ductile fracture behavior usually results in slow and stable crack extension producing a rising resistance curve, at least during the early stages of crack growth. (Anderson 2005, p. 232; Zhu & Joyce 2012, p. 4)

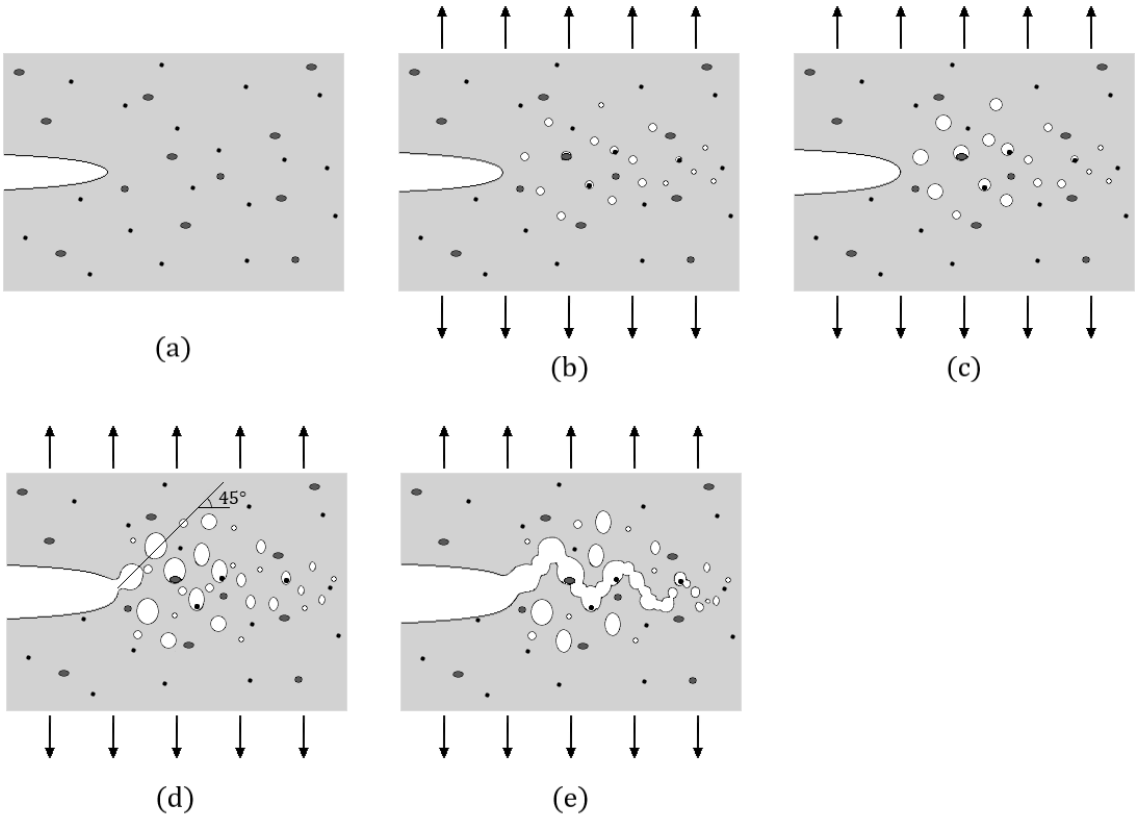

Figure 2. Mechanism for ductile crack growth: (a) initial state, (b) void formation at the crack-tip, (c) void growth, (d) coalescence of voids with the crack-tip, plane of maximum plastic strain at 45° angle, and (e) ductile crack growth in a 45° zigzag pattern.

Because of the through-thickness variation of stress triaxiality, an edge crack in a plate exhibits *a tunneling effect*, illustrated in figure 3, as it grows by microvoid coalescence: at the center of the plate where stress triaxiality is high, crack growth is fast, while near the plate edges, where triaxiality is lower, the growth lags behind. The faster growing crack at the center of the plate produces deformation bands near the free surfaces at a 45° angle from the maximum principal stress, enabling microvoid nucleation at smaller particles. Hence the crack growth near the edges occurs at a 45° angle, causing *shear lips*, which are very similar to *the cup and cone* features in uniaxial tensile specimens. (Anderson 2005, p. 232)

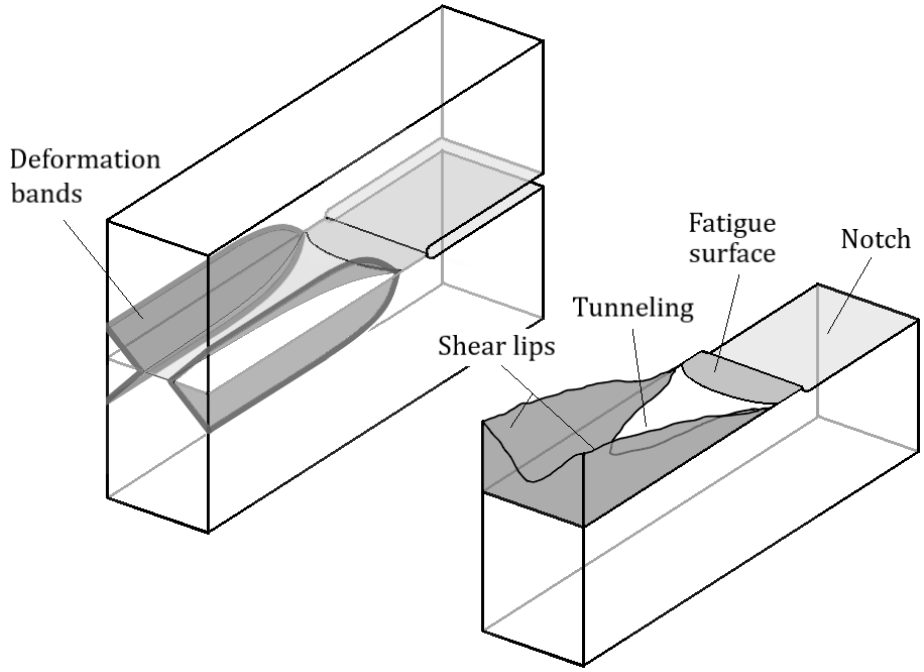

Figure 3**.** Ductile growth of an edge crack.

When a crack is subject to plane strain Mode I loading, the maximum plastic strain occurs at 45° angle from the crack plane, which on a local level is the preferred path for void coalescence and crack growth. The global constraints, however, require that the crack propagation remain in its original plane, normal to the applied stress. This leads to a compromise where the fracture path locally forms a zigzag pattern (by altering the path ±45° from the crack propagation direction) when viewed at higher magnifications, but in a global scale appears flat. The zigzag pattern, illustrated in figure 2(e), is often observed in ductile materials. (Suresh 1991, pp. 139, 335; Hansson & Melin 2008, p. 1400; Anderson 2005, p. 233)

2.1.2 Brittle fracture

Brittle fracture is considered the most critical failure mechanism. This is because the occurrence of brittle fracture is not related to the mechanical strength of the material and may lead to failure at unexpectedly low stress levels. In brittle fracture, fracture is typically preceded by a relatively low energy absorption through regions of small plastic deformation and there is usually no apparent plastic deformation or distortion of the shape of the part before the fracture event, when operating outside the material's ductile-brittle transition region. Brittle fracture often occurs at high speeds and propagates without remarkable increase in applied loading. Often it has a unique, well-defined point of crack initiation, corresponding to a sudden drop in load, and thus provides a measurement of a point value of FT (Zhu & Joyce 2012, p. 4). Brittle fracture is characterized by a shiny fracture surface with a grainy appearance, often featuring chevron patterns pointing back to the origin of failure. (Wallin 2011, p.115; Anderson 2005, p. 234; MacKenzie 2008, pp. 53 – 54)

Brittle fracture can be divided into two categories: transgranular cleavage fracture and intergranular, grain boundary fracture. In intergranular fracture, failure occurs by decohesion along grain boundaries, as illustrated in figure 4(a). Characterization of grain boundary fracture may be difficult as it can be either brittle stress controlled or ductile strain controlled. Although there is no single mechanism for intergranular fracture, a variety of circumstances that may lead to cracking along the grain boundaries, such as precipitation of a brittle phase on the grain boundary, intergranular corrosion, environmental cracking or grain boundary cavitation and cracking at high temperatures, exist. This type of failure mainly occurs in metals with higher level of impurities, and thus does not usually concern modern metals. (MacKenzie 2008, p. 59; Lynch 2019)

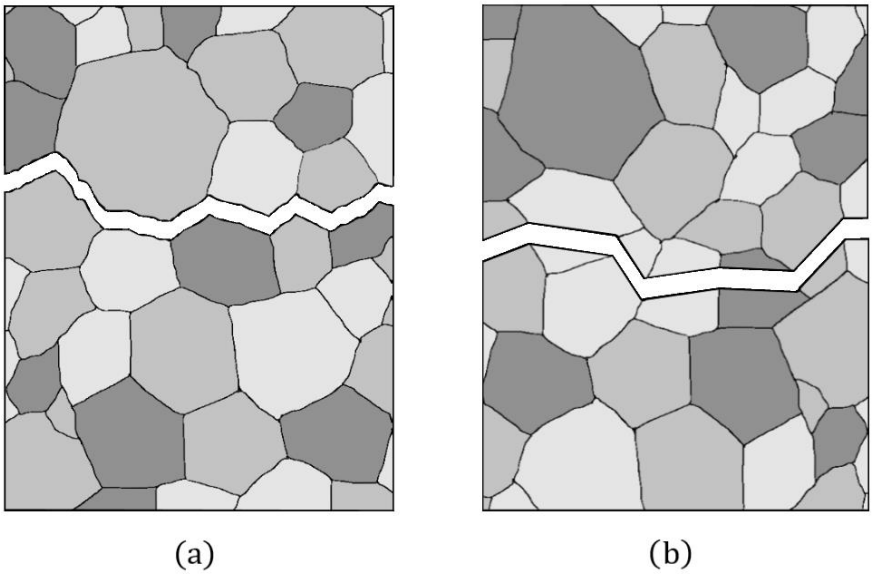

Figure 4. Fracture paths of brittle fracture a) intergranular fracture b) transgranular fracture.

Out of the two brittle fracture mechanism cleavage is the more commonly encountered mechanism and is usually referred to when the term brittle fracture is used. Cleavage fracture can be defined as a rapid crack propagation along specific crystallographic planes. The preferred cleavage planes are those with the lowest packing density as the distance between these planes is the greatest and there are fewer bonds to be broken, thus, less energy is needed for separation. For an example, in body-centered cubic (BCC) materials, such as ferritic steels, cleavage occurs along {100} planes. In the case of so called quasi-cleavage fracture, which especially concerns martensitic and bainitic steels, failure occurs also on {110} and {112} planes (ASM Handbook committee 1987, p. 20). In quasi-cleavage the fracture surface exhibits both cleavage and plastic deformation characteristics: fracture initiates at the central cleavage facets and as the crack radiates forming river patterns the cleavage facets blend into areas of dimple rupture and the cleavage steps become tear ridges (ASM Handbook committee 1987, p. 20). The river markings on opposing fracture surfaces match ridge-to-ridge rather than step-to-step as in cleavage (Martin et al. 2010, p. 1601). The underlying formation mechanisms of quasi-cleavage fracture features still remain unclear, although the subject has been addressed by many researchers in recent years (Cho et al. 2021 pp. 1 – 2; Martin et al. 2010). The micromechanism of cleavage on the other hand is rather well known and further depicted next.

Cleavage is most likely to occurs when the plastic flow of the material is restricted, that is, when only a limited number of active slip systems exist, as is the case with BCC metals at low temperature, or with polycrystalline hexagonal close-packed (HCP) metals, which only have three slip systems per grain. Face-centered cubic (FCC) metals, on the other hand, are generally not prone to cleavage since there are plenty of slip systems for ductile behavior to take place at all temperatures. (Anderson 2005, p. 234)

For a cleavage fracture to occur, stress must locally be sufficient to overcome the cohesive strength of the material to break the bonds between atoms. The theoretical fracture strength of a crystalline solid $\sigma_f \approx E/\pi$, where E is the Young's modulus. The stress peak at the distance of $\sim 2\delta$ from a (blunted) macrocrack-tip, however, is not adequately high to provide sufficient stress concentration to exceed the bond strength. Sufficient local stress concentration can be provided by local discontinuities ahead of the macroscopic crack, such as sharp microcracks, precipitates, inclusions or grain boundaries acting alone or in combination. Different mechanisms for microcrack formation have been proposed, such as microcrack formation at intersecting slip-planes by means of dislocation interaction (pile-up) or mechanisms provided by second-phase particles, e.g., carbides or inclusion, which are more common mechanism in steels. A second-phase particle ahead of the tip of a macrocrack is exposed to the local stress and strain concentrations caused by the macrocrack. Cleavage nucleates as the second-phase particle cracks because of the plastic strain in the surrounding matrix and then, providing a sufficiently high stress concentration ahead of the macrocrack exists, propagates into the ferritic matrix, causing failure by cleavage. The microstructural feature that nucleates cleavage depends on the material and heat treatments performed. For an example, in mild steels, cleavage initiation usually occurs at grain boundary carbides whereas, in quenched and tempered alloy steels, the critical feature is typically either a spherical carbide or an inclusion. (Anderson 2005, pp. 235 – 237, Wallin 2011, pp. 115 – 116)

In order to find a particle large enough to nucleate cleavage (weakest link), a finite volume of material ahead of the crack-tip must be sampled. The critical particle size depends on the magnitude of stress. Because the particle dispersion and the location of the critical fracture-triggering particle is random, two nominally identical specimens of the same material may display vastly different fracture toughness values as one specimen may sample the fracture-triggering particle near the crack-tip, while in the other it may lie further from the crack-tip. The latter specimen would thus produce a higher fracture

toughness as a higher load is required to elevate the stress at the particle to a critical value. This apparent randomness and the statistical nature of fracture explains why cleavage FT data tends to be widely scattered and leads to an apparent thickness effect on toughness: a thicker specimen is more likely to sample a large fracture triggering particle along the crack front and will thus, on average, display a lower fracture toughness than a thin specimen. (Anderson 2005, pp. 241 – 242)

The cleavage fracture path in polycrystalline materials is transgranular. Once the cleavage crack has nucleated, additional work must be performed in order to enable the propagation as the crack crosses randomly oriented grains, since the mismatch between grains in polycrystalline materials obstructs cleavage propagation. The nominal orientation of the propagating cleavage crack is fixed perpendicular to the maximum principal stress, which means the propagating crack has to change direction each time it crosses a grain boundary as it seeks the most favorably oriented cleavage plane in each grain, see figure 4 (b). This cleavage crack propagation process across variously oriented grains in a polycrystalline material, creates a multifaceted fracture surface, where each facet corresponds to a single grain. As the propagating crack encounters a grain or a subgrain boundary, where the nearest cleavage plane in the adjoining grain is oriented at a finite twist and/or tilt angle from the current cleavage plane, it may distribute on several parallel planes in order to accommodate the twist or tilt mismatch between the grains, as illustrated in figure 5. The propagation process of these multiple cracks, however, consumes more energy than a crack propagation on a single plane would, thus creating a tendency for the initially parallel cracks to converge into a single crack due tearing between parallel cleavage planes. The tendence of the propagating crack to continuously divide and converge as it passes through a polycrystalline material, creates multiple lines that converge to a single line, much like tributaries to a river, forming *river patterns*, which are a typical feature for a cleavage fracture. The direction of crack propagation can also be inferred from these river patterns. (Anderson 2005, pp. 234 – 235, 238, 244)

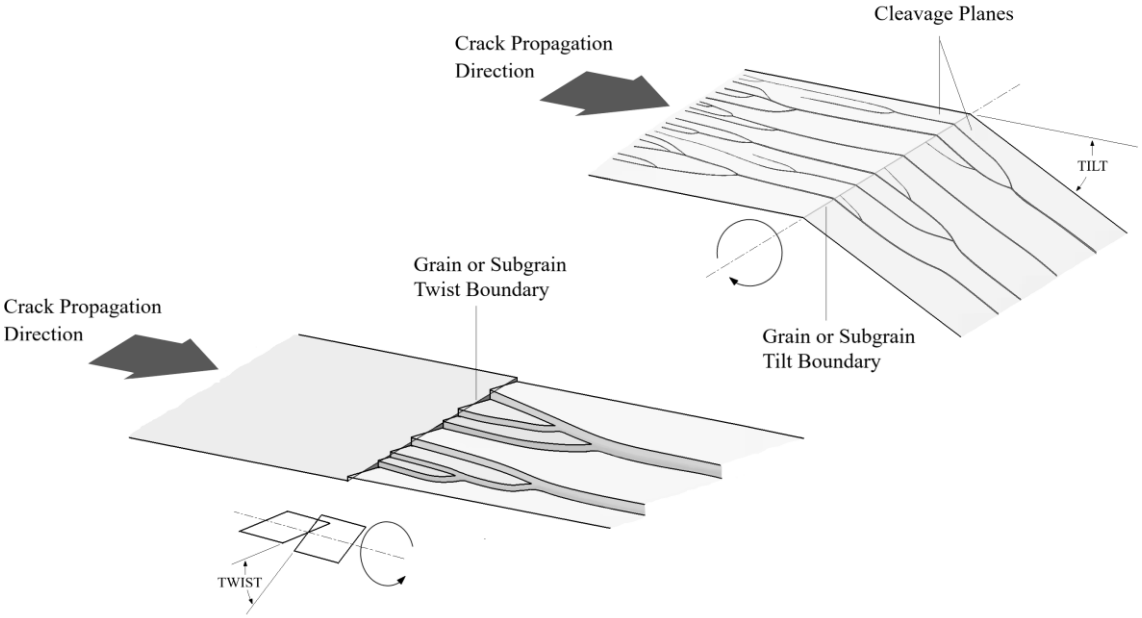

Figure 5. Formation of river patterns, as a result of a cleavage crack crossing a twist or a tilt boundary.

So, for a successful cleavage event to occur, after the initiation at a sufficient crack nucleation site, the driving force for fracture must be sufficiently high to overcome the possible barriers for propagation, e.g. particle/matrix interface, grain boundary or a steep stress gradient, otherwise the crack may arrest resulting in unsuccessful cleavage event.

Despite the fact that there is usually no apparent plastic deformation before the fracture event, and regardless of the nucleation mechanism, brittle fracture in metals practically always occurs through plastic deformation. Even in a case where a metal structure with a superficial crack is subjected to tensile stress, a plastic zone forms at the crack-tip. The significance of this plastic zone concerning brittle fracture is twofold: it rounds the tip of the crack, reducing the stress concentration caused by the crack and the risk of brittle fracture, but on the other hand, the plastic deformation itself nucleates microcracks in the plastic zone, which propagate when the stress caused by the macrocrack becomes high enough. Plastic deformation also occurs at the tip of the microcrack, making it difficult for the crack to progress. The easier the plastic deformation occurs in front of a microcrack and the more homogeneous it is, the easier the crack arrests and the tougher the metal. Based on this, brittle fracture is often considered to be controlled by crack propagation in many metals. (Hannula et al. 2020a, p. 95) However, depending on material, temperature, loading geometry and rate, different stages of cleavage process are

more likely to be most critical. For instance, for structural steels at lower shelf temperatures in the case of cracks with very steep stress distribution, propagation of microcrack to the ferrite matrix and advancing to surrounding grains is more difficult than initiation and thus tend to control the fracture process. Whereas at higher temperatures, where the steepness of stress distribution is lower, propagation becomes easier in relation to initiation and initiation becomes more dominant for the process. The initiation dominated temperature region is usually referred to as the transition region. In the case of fatigue precracked specimens the dominating stages of cleavage process may often be deduced by visually examining the fracture surface. At lower shelf temperatures, numerous initiation sites are often visible, whereas at higher temperatures, corresponding to transition region, usually only one or two initiation sites can be detected. Same however, does not apply for notched or plain specimens where only a few initiation sites can be seen even on the lower shelf. (Wallin 2011, p. 116)

2.1.3 The ductile-brittle transition

Body centered cubic materials may fracture both in a ductile or a brittle manner, depending on the temperature and the initial toughness of a given microstructure. The fracture toughness of ferritic steels, for instance, can change drastically over a small temperature range. At low temperatures, steel may be brittle and fails by cleavage but at higher temperatures, the material behaves in a ductile manner and fails by microvoid coalescence. In the transition region between brittle and ductile behavior, both micromechanisms of fracture can occur in the same sample. In the lower transition region, the fracture mechanism is pure cleavage, but material toughness increases rapidly with the rising temperature as cleavage becomes more difficult, whereas, in the upper transition region, a crack initiates by microvoid coalescence but ultimate failure occurs by cleavage. The fracture toughness in the transition region is governed by the statistical sampling effect: on initial loading in the upper transition region, cleavage does not occur as there are no critical particles near the crack-tip, but as the crack grows by ductile tearing, more material is sampled. Eventually, the growing crack samples a critical particle and cleavage occurs. This explains why the FT data in the transition region tends to be highly scattered. Furthermore, the transition region fracture toughness is also sensitive to constraint differences and the rate of loading. On the so-called lower shelf all the possible initiation sites are activated and initiation occurs as soon as the crack is loaded, making initiation event independent of the load level and subsequently of specimen thickness (Wallin 2011, p. 130). Thus cleavage fracture stress hardly shows any

temperature or strain rate dependence, but a triaxial stress state ahead of the tip of a sharp crack constraints the onset of yielding, meaning, yielding occurs at a higher stress than observed in uni- or biaxial stress state as schematically illustrated in figure 6. Cleavage becomes possible at temperatures higher than the material's transition temperature i.e. the material acts more brittle. Influence of loading rate on the other hand is illustrated in figure 7, where it can be observed that increasing loading rate causes a rise in the yield strength, moving the ductile-brittle transition temperature to higher values (Wallin et al. 2015, p. 223). (Anderson 2005, p. 247; Wallin 2011, ch. 4, ArcelorMittal)

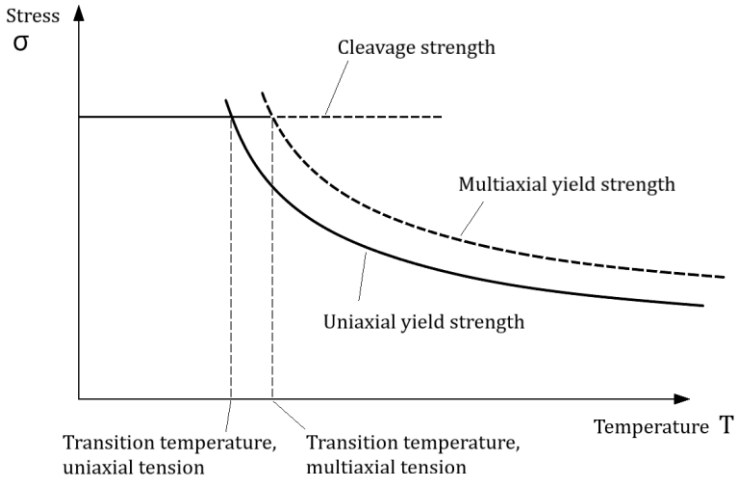

Figure 6. Effect of triaxiality on the transition temperature for a ferritic steel.

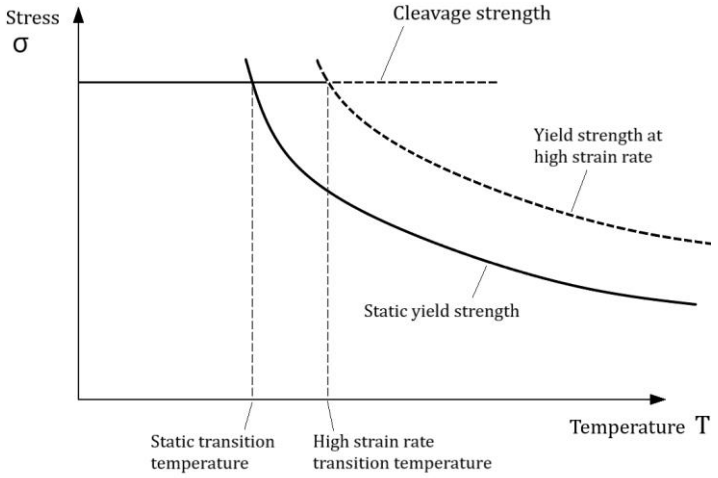

Figure 7. Influence of loading rate to the ductile-brittle transition temperature.

Specimen thickness, or rather the crack front length, also shows some influence. Generally the fracture toughness decreases with increasing crack front length in the transition region because initiation will be sufficiently difficult. However, as the crack front length increases, initiation becomes more and more likely and at some point, will no longer control the fracture event. The change from initiation to propagation control will be gradual with the size effect slowly vanishing as the crack front length increases, and varies with temperature, loading rate and specimen size. Estimation of the crack front length at which the size effect will disappear is thus impossible, as the experimental results would only reflect the controlling mechanism. (Wallin 2011, pp. 144 – 145)

So, as a recap, fracture toughness is dependent on a material (mechanical properties, microstructure, micromechanism of failure, homogeneity, residual stresses), geometry of the component (constraint), flaw size, temperature, and loading rate. Considering all these different factors, it is easy to gather that the FT data obtained from laboratory specimens may not directly describe the fracture behavior of real flawed structures. Thus, when testing in the transition region, it is advisable to apply methods, such as the Master Curve, that do consider all these different factors. (Wallin 2011, pp. 115 – 172, 393 – 430)

2.2 Fracture mechanics

Classical plasticity theory and mathematical descriptions of fracture events are full of simplifications, such as assumptions of either fully elastic or fully plastic nonhardening material behavior, small-scale yielding conditions or a case of a stationary crack and are often derived from two-dimensional approximations. (Anderson 2005, pp. 73, 169) For analysis purposes material under investigation is considered anisotropic and sufficiently homogeneous to be represented by a simple continuum mechanics description (Wallin 2011, p. 115). Furthermore, in order to simplify calculations, linear-elastic and elastic-plastic fracture mechanics assume a quasistatic process. What this means, is that work is applied to the specimen slow enough, as not to affect the material typical fracture behavior, and for the specimen to experience seemingly static, rate-independent deformation, meaning that dynamic fracture mechanical aspects, such as inertia forces, rate-dependent material behavior and reflected stress waves can be neglected (Anderson 2005, p.173). When the change is sufficiently slow, the system can be taken to be in equilibrium at all times, meaning intensive quantities of the system can be defined at

every instant during the process and the state of the system at any point can be expressed with the equations of equilibrium.

The simple formulae of classical fracture mechanics, although sufficiently applicable for some cases, are seldom rigorously correct, sometimes even provide a distorted view of reality and often result in slightly over conservative estimations of fracture toughness. In an effort to adapt these simplified descriptions of fracture to reflect reality as closely as possible, many improvements and corrections for the original crude descriptions have been developed and employed in practice as more precise techniques to assess fracture mechanic phenomena have become available over the years. Nowadays, three-dimensional finite element analyses (FEM) of components with cracks for instance, are commonplace (Anderson 2005, pp. 73, 169).

The primary assumption for fracture mechanic analysis is that a structure already contains a macrocrack-like defect which can act as a stress concentrator and a probable initiation point for fracture (Kanvinde 2016, p. 3). Thus, originally, the microscopic phenomena leading to fracture were not considered important for analysis and were often neglected in calculations. As macrocracks were considered to have a greater importance in light of fracture analyses purposes, the fracture behavior in the analyses is based on the global behavior of materials, and hence depends on mechanical properties of materials, such as yield strength σ_{YS} and Young's modulus E. Nowadays, it is well acknowledged that also the micromechanisms of fracture play a role in materials' fracture behavior.

Much of classical fracture mechanics is predicted on the assumption that fracture toughness is a material property and that there exists a single lower bound, geometry and specimen size independent FT value for a crack under plane-strain stress state, that can be expressed with a one-parameter continuum mechanics description of fracture criteria. (Anderson 2005, p. 40; Wallin 2011, p. 1)

Two competing crack growth parameters – driving force and material resistance – are compared in fracture mechanics. The driving force for fracture results from a combination of flaw size (geometry) and loading conditions, whereas material resistance reflects the material's ability to resist crack propagation. Fracture mechanical parameters describe the driving force, whereas characteristic or critical values of these parameters (i.e. of driving force) describe the tearing resistance of the material. (Wallin 2011, p. 8)

2.2.1 Flaw induced stress state

In practice, all structures contain some sort of material defects that can affect the structural integrity and eventually lead to failure. Therefore, a fracture is often triggered around sharp cracks, discontinuities and other stress concentrators in structures (Wciślik & Pała 2021, p. 2). For fracture mechanics analysis purposes, a crack is considered as a flat surface: scales are such that roughness of the crack surface is considered negligible and thus thought not to contribute to the outcome of the analysis (Liaw 2000, p. 563). Also an assumption of a through crack with a straight crack front is usually made. In reality, postulated flaws often have unrealistically long crack fronts compared to real structural flaws since their size is often based on a driving force perspective. When applied, the results derived from such specimens likely result in overly conservative estimates of structural integrity. (Wallin 2011, p. 147)

There are three types of loading, referred to as modes (illustrated in figure 8), that a crack can experience. On mode I loading, the crack tends to open as the principal load is applied normal to the crack plane. On mode II loading, where loading type corresponds to in-plane shear loading, one crack face tends to slide with respect to the other. And on mode III, crack faces also tend to slide with respect to one another, but the principal loading corresponds to out-of-plane shear. Any cracked structure loading case can be presented in analyses through any one of these modes, or a combination of two or three modes. (Anderson 2005, p.43; Liaw 2000, p. 563)

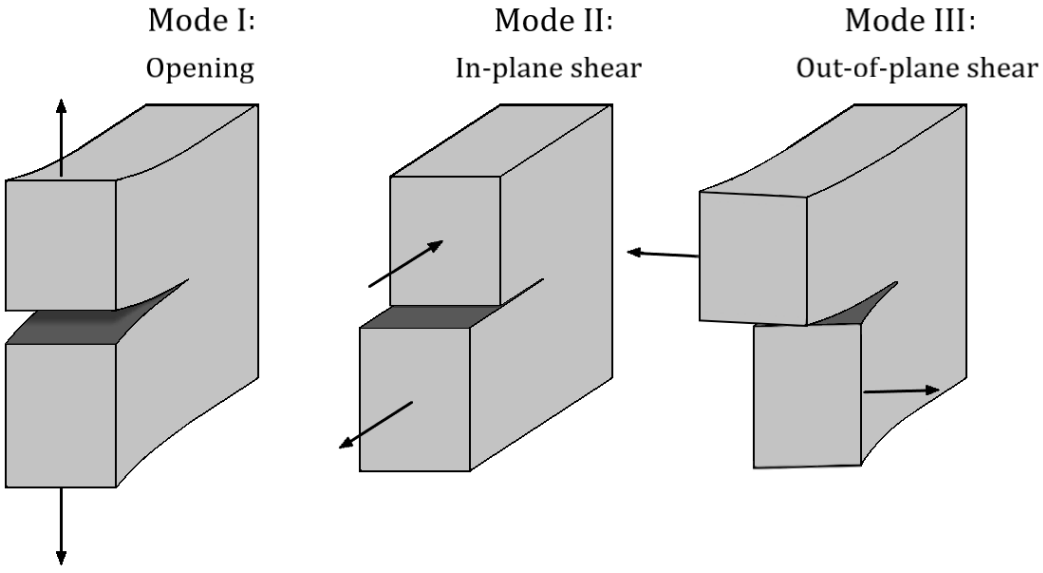

Figure 8. Three modes of loading that a crack can experience.

Fracture mechanics concepts for each mode are essentially the same, but the great majority of all actual cracking and fracture cases tend to shift to mode I problems. This is because a crack in the very early stage of development will turn into a direction in which it experiences only mode I loading, unless prevented from doing so by geometrical confinement. For this reason, fracture mechanics analyses are usually confined to mode I loading cases. (Liaw 2000, p. 563) Also, traditionally it has been assumed that the fracture toughness in mode I is lower than in modes II or III, and thus provides a more conservative estimate for FT, which is a valid assumption for the tensile stress state controlled brittle cleavage fracture. However, same is not always true for the critical failure strain controlled ductile fracture, where the shear fracture toughness may be considerably lower than mode I fracture toughness (Wallin 2011, p. 11).

The stress distribution of a loaded structure is influenced by the existence of a sharp crack like defect. When a structure, e.g. a plate, is loaded and there is no crack, the plate is in a state of plane stress. But once a crack is introduced, a stress concentration is formed ahead of the crack-tip, and the stress distribution in the plate is changed. Inglis provided the first quantitative evidence for the stress concentration effect of flaws in 1913. He analyzed elliptical holes that would begin to take on the appearance of a sharp crack in flat, infinitely large plates. An infinitely sharp crack, with a radius of $\rho = 0$, in a continuum is a mathematical abstraction that is not relevant to real materials where, even in the absence of plastic deformation, the minimum radius a crack-tip could have is on the order of the atomic radius. Results of his analysis predicted an infinite stress at the tip of an infinitely sharp crack, meaning that a material containing a sharp crack should thus theoretically fail upon the application of an infinitesimal load. This obviously is not the case in real materials where the continuum assumption, upon which the Inglis analysis is based on, is not valid at the atomic level. (Anderson 2005, pp. 25 – 29)

Much of the classical fracture mechanics theory is predicated on two-dimensional approximation, that is, either pure plane stress or pure plane strain is assumed. In reality these two-dimensional assumptions are often too simplistic and may give a distorted view of reality, although in some cases a two-dimensional model can be appropriate. (Anderson 2005, p. 73)

Stress distribution of a flawed structure is schematically illustrated in figure 9. The stress state in front of the crack is close to plane strain, but far away from the crack-tip, the plate is in a state of a plane stress. The global behavior of the structure is thus in a state between plane stress and plane strain. In case of plane stress, one component of stress is assumed zero, that is $\sigma_{zz} = 0$, and in case of plane strain, one component of strain is assumed zero, $\varepsilon_{zz} = 0$, meaning in plane strain material flow is restricted in the z direction. Thus, in a finite plate with a crack, material near the crack-tip is loaded to higher stresses than the surrounding material. Because of the high stress normal to the crack plane, σ_{yy} in figure 9, the material near the crack-tip tries to contract in the x and z directions but is prevented from doing so by the surrounding material. This *constraint* causes a triaxial state of stress near the crack-tip. The triaxiality of material near the crack-tip varies along the crack front, being highest in the middle of the plate, where stress component in the z direction, σ_{zz}, gets the highest values, and diminishing when nearing the free edges of the plate as $\sigma_{zz} \to 0$. This variation of triaxiality is illustrated in figure 10 as a schematic plot of the stress parallel to the crack front, σ_{zz}, in a plate depicted in figure 9. The stress state in the central region of the plate is essentially plane strain at distances from the crack-tip that are small compared to the plate thickness. Near the free surface, the stress triaxiality is lower, but a state of pure plane stress exists only at the free surface. (Anderson 2005, pp. 73 – 74) In real materials, where continuum mechanics description is not strictly valid, also the microstructural differences on the size scale of grains affect the stress distribution along the crack front length and there will be stochastic variation in local stresses and strains (Wallin, 2011 p. 115).

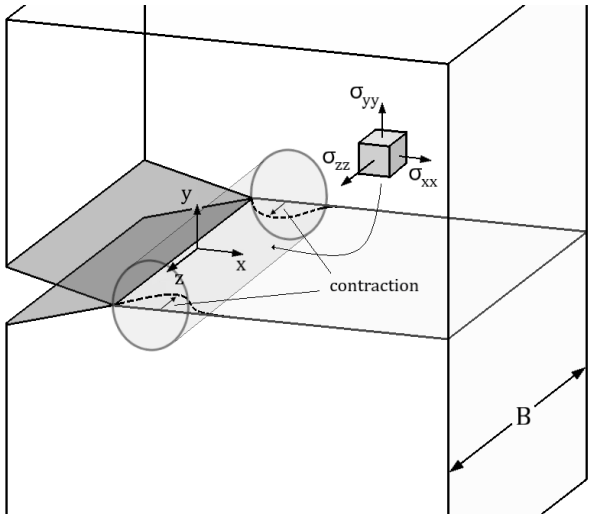

Figure 9. Three-dimensional deformation at the crack-tip. The high normal stress at the crack-tip causes material near side surfaces to contract, but material in the interior is constrained, causing a triaxial stress state.

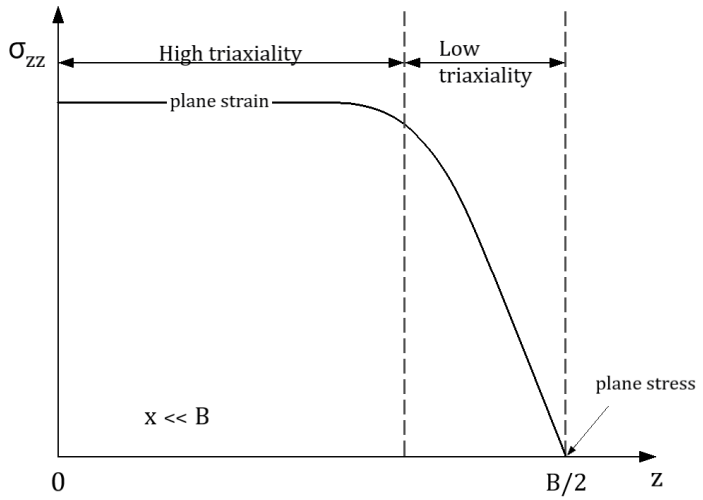

Figure 10. Schematic variation of transverse stress and strain through the thickness at near vicinity to the crack-tip.

As mentioned, triaxiality changes also along the x direction of the plate: material near the crack-tip front experiences high triaxiality, but when x is a significant fraction of the plate thickness $\sigma_{zz} = 0$. Thus, the stress state close to the crack-tip front is essentially plane strain in the interior of the plate, but plane stress conditions exist remote from the crack-tip front. (Anderson 2005, p. 74)

The triaxial stress state associated with plane strain results in higher stresses (2.5 times higher compared to plane stress on the crack plane) in the plastic zone. In materials with a ductile behavior, triaxial stresses assist ductile fracture processes such as microvoid coalescence and for fracture mechanisms that are governed by normal stress, e.g. cleavage in metals, the material will behave in a more brittle manner when subjected to a triaxial stress state. Thus the effect of stress state can affect the fracture behavior of a given material significantly. (Anderson 2005, pp. 73 – 75)

Because of the higher stress concentration (high triaxiality) in front of the crack, material yield strength is exceeded locally and a plastic zone is formed around the crack-tip. The size of the plastic zone depends on the material's strength, strain hardening tendency, geometry (constraint) and applied loading. The extent of plasticity is not the same at all directions. Theoretical estimates of the plastic zone radius r as a function of θ for both plane stress and plane strain in each loading mode are plotted in figure 11 and define the approximate boundary between elastic and plastic behavior.

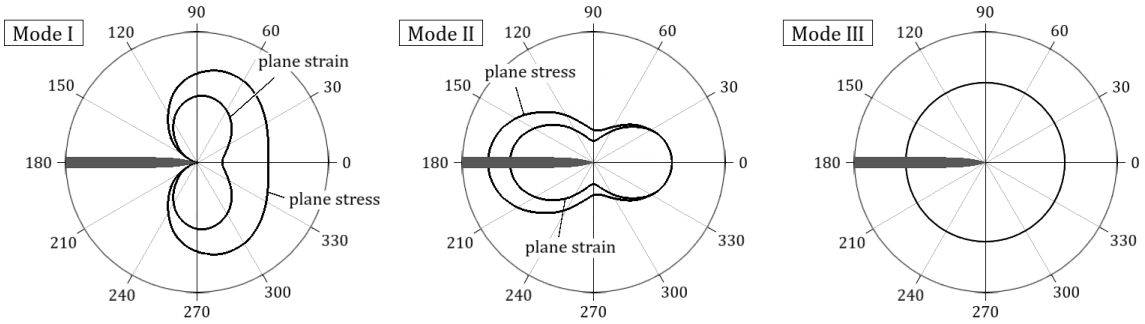

Figure 11. Theoretical crack-tip plastic zone shapes estimated from elastic stress solutions and von Mises yield criterion: (a) Mode I, (b) Mode II, and (c) Mode III.

As can be seen from figure 11 (a), there is a clear difference in plastic zone sizes between plane stress and plane strain conditions: plane strain suppresses yielding which results in a smaller plastic zone for a given stress intensity K_I value. A schematic presentation of three-dimensional slip planes of a mode I crack for both plane stress and plane strain are shown in figure 12. Due to the free surface effect, the three-dimensional plastic zone shape in a finite plate, takes on the form of a 'dog-bone', as schematically depicted in figure 13 (Wang 1996, p. 43). The theoretical estimates in figure 11 for plastic zone shape are strictly not correct, since they are based purely on elastic analysis and, for an example, do not consider stress redistribution caused by crack-tip plasticity or the effect of strain hardening of the material. They do, however, provide reasonable estimates of the plastic zone size and shape. The strain hardening effect on the plastic zone shape are schematically illustrated in figure 14. This illustration is an adaptation of a presentation provided by Anderson (2005), where a detailed elastic-plastic crack-tip stress solution obtained from finite element analysis is compared to the plane strain plastic zone shape estimate derived from the above mentioned elastic analysis (see Anderson 2005, p. 69). As illustrated in figure 14, a higher strain hardening rate results in a smaller plastic zone size because the material inside the plastic zone is capable of carrying higher stresses, and thus less stress distribution is required. (Anderson 2005, pp. 66 – 69)

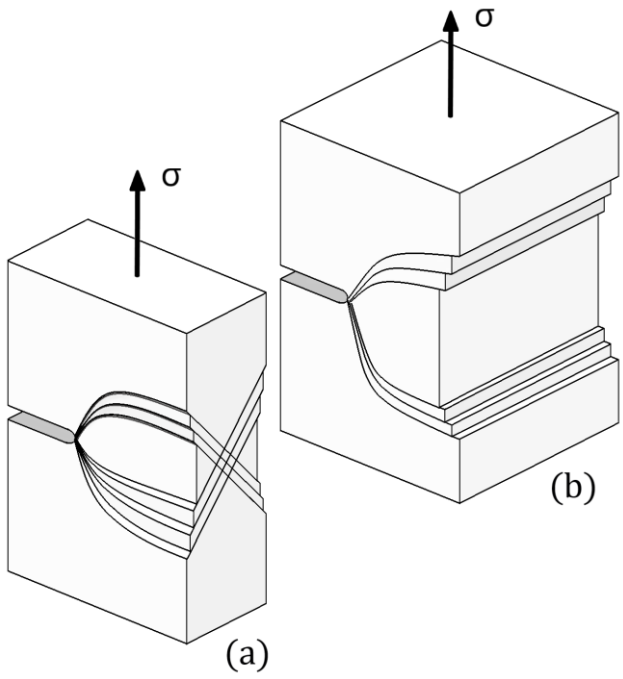

Figure 12. Slip planes around a mode I crack for (a) plane stress and (b) plane strain.

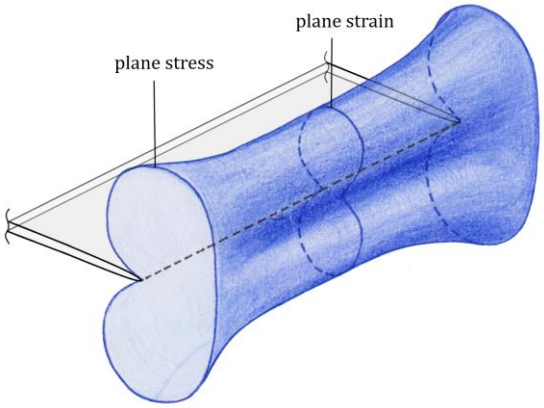

Figure 13. Schematic representation of the three-dimensional nature of the plastic zone around a crack-tip in finite plate.

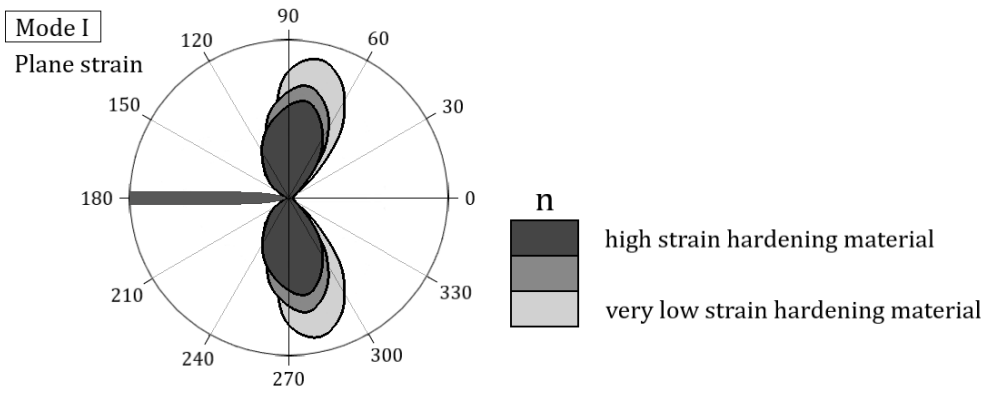

Figure 14. Effect of strain hardening on the Mode I plastic zone shape.

Despite the redistribution of stresses after considerable deformation, the triaxial stress state at the tip persist, even when the entire cross-section has yielded. The plastic zone takes on a plane stress shape when it grows to a significant fraction of the plate thickness, where $\sigma_{zz} = 0$, that is, approximately half the plate thickness. Although the stress state at the plastic zone boundary is plane stress when the plastic zone size is of the same order of magnitude as the plate thickness, a zone of high triaxiality persists at the crack-tip and can exist even in the presence of large-scale plasticity. (Anderson 2005, pp. 78 – 79)

Fracture mechanical parameters provide a description of the stress field ahead of a crack. These parameters can be divided into linear-elastic and elastic-plastic parameters. Elastic parameters can generally be considered as a special cases of elastic-plastic parameters, meaning elastic-plastic parameters can be used as such in the elastic regime. Elastic parameters, however, cannot be applied in elastic-plastic regime without some corrections. (Wallin 2011, p. 9)

2.2.2 Linear Elastic Fracture Mechanics

Originally linear elastic fracture mechanics (LEFM) analysis was restricted to structures whose global behavior was linear elastic. More advanced theories have been developed over the years to also account for nonlinear material behavior such as plasticity and viscoplasticity as well as dynamic effects, but these more advanced concepts are all extensions of linear elastic fracture mechanics. (Anderson 2005, p. 25)

At an atomic level, a material fractures when sufficient stress and work is applied to break the bonds, supplied by the attractive forces between atoms, that hold the atoms together. The theoretical cohesive strength σ_c of a material can be estimated to be approximately E/π, but experimental fracture strengths for brittle materials have been observed to be typically three or four orders of magnitude below this theoretical value, which has been acknowledged to be due to the flaws in actual materials. Since fracture cannot occur unless the stress at the atomic level exceeds the cohesive strength of the material, existing flaws must lower the global strength by magnifying the stress locally. (Anderson 2005, pp. 25 – 28)

The Griffith's model, published in 1920, is based on a global energy balance and dictates that for a fracture to occur, the energy stored in the structure must be sufficient to overcome the surface energy of the material. The Griffith energy balance for an incremental increase in the crack area dA, under equilibrium conditions, can be expressed as follows:

$$-\frac{d\Pi}{dA} = \frac{\mathrm{d}W_s}{\mathrm{d}A} \tag{1}$$

where Π is the potential energy supplied by the internal strain energy and external forces and W_s is the work required to create new surfaces. Since fracture involves breaking of bonds between atoms, the local stress intensification on the atomic level, which can be provided by flaws, must be equal to the cohesive stress σ_c. In other words, when the strain energy change that results from an increment of crack growth is sufficient to overcome the surface energy of the material, the flaw becomes unstable, and fracture occurs.

Since the Griffith's model assumes that the work of fracture comes exclusively from the surface energy of the material, the approach only applied to ideally brittle solids and failed to predict the relationship between strength and flaw size in metals, since plastic deformation at the crack-tip absorbs more applied energy than the surface energy. A modification to Griffith's model which extended the approach to metals by including the energy dissipated by local plastic flow was later proposed independently by both Irwin and Orowan. The modification could be further generalized to account for any type of energy dissipation by substituting the terms of surface energy with fracture energy w_f, which could include plastic, viscoelastic or viscoplastic effects as well as consider the

effects of crack meandering and branching, which increase the surface area of the crack. (Anderson 2005, pp. 29 – 33; Zhu and Joyce 2012, p. 7)

In 1956 Irwin defined a new parameter, *energy release rate* G, also known as *the crack extension force* or *the crack driving force*, which expresses the rate of change in potential energy Π with respect to the crack area A, and can be perceived as a measure of the potential energy available for an increment of crack extension or, that is released from a structure when the crack grows in an elastic material, and which therefore is valid for any elastic material. According to Griffith's model, for a through-thickness crack $2a$ long in an infinitely wide plate subjected to a remote tensile stress perpendicular to the major axis of the crack

$$G = -\frac{d\Pi}{dA} = \frac{\pi\sigma^2 a}{E} \tag{2}$$

and crack extension occurs when G reaches a critical value, that is when

$$\frac{\mathrm{d}W_s}{\mathrm{d}A} = 2\gamma_s = 2w_f = G_c \tag{3}$$

where γ_s is surface energy per unit area and G_c is *the fracture toughness* of the material. A plot of G vs. crack extension is called *the driving force curve*. The first fracture toughness tests for metals were performed using the parameter G, but it was soon replaced by the stress intensity factor K due to the simplicity of use. (Anderson 2005, pp. 34 – 41; Wallin 2011, pp. 9 – 10)

The potential energy of an elastic body depends on the strain energy stored in the body and by the work done by external forces which in turn depend on whether the structure is load or displacement controlled. The relation between force and displacement is defined as *the compliance* C,

$$C = \frac{\Delta}{P}, \tag{4}$$

where Δ is the displacement and P is the load. The system compliance $C_m = 0$ for pure displacement control and $C_m = \infty$ for pure load control. When compliance is incorporated in calculations of G for either load or displacement controlled case, it has been shown that the difference between absolute values of the strain energies $(dU)_P$ and $(dU)_\Delta$ is negligible, and thus, the energy release rate G, as defined in equation (2), is the

same for both load control and displacement control. In reality, most structures are subject to conditions between the extremes of pure load control and pure displacement control, meaning the system has a finite compliance. (Anderson 2005, pp. 35 – 38)

Crack extension occurs as

$$G = 2w_f = R, \tag{5}$$

where R is *the material resistance to crack extension*, and crack growth can be either stable or unstable depending on how G and w_f vary with crack size. A plot of R vs. crack extension is called R-*curve* or *a resistance curve*. Different materials exhibit different kind of R-curves, for example, ductile fracture in metals usually results in a rising R-curve, while for an ideally brittle material the R-curve is flat and some materials that fail by cleavage can even display a falling R-curve. Stability of crack growth can be assessed by comparing material's driving force curve to its resistance curve. When the resistance curve is flat, one can unambiguously define a critical value of energy release rate G_c, but a material with a rising R-curve, cannot be uniquely characterized with a single toughness value, though the value of G at the initiation of the crack growth can be determined. A flawed structure fails when the driving force curve is tangent to the R-curve. The point of tangency depends on the shape of the driving force curve, which in turn depends on the material behavior and, to a lesser extent, on the configuration of the structure. Crack growth is stable when

$$G = R$$

or

$$\frac{d\mathrm{G}}{da} \leq \frac{dR}{da} \tag{6}$$

and unstable when

$$\frac{d\mathrm{G}}{da} > \frac{dR}{da} \ . \tag{7}$$

As illustrated above, the stability of crack growth depends on the rate of change in G, i.e. the second derivative of potential energy. Although the driving force G is the same for both load control and displacement control, the rate of change of the driving force curve

depends on how the structure is loaded. Displacement control tends to be more stable than load control, which is why specimens are usually tested in displacement control, or as near to pure displacement control as is possible, when experimentally determining the R-curve. Most of the common test specimen geometries exhibit falling driving force curves in displacement control, which means it is possible to obtain a significant amount of stable crack growth, but when an instability occurs during the test, the R-curve cannot be defined beyond the point of ultimate failure. (Anderson 2005, pp. 38 – 41)

Ideally, the R-curve should only be a material property and not depend on size or shape of a cracked body, but size and geometry (constraint) of a cracked structure can exert some influence on the shape of the R-curve. For example, because of a low degree of stress triaxiality at the crack-tip in a thin sheet, a crack in a thin sheet tends to produce a steeper R-curve than a crack in a thick plate, where the material near the tip of the crack may be in plane strain. The R-curve can also be affected when a growing crack approaches a free boundary in the structure. Thus, two plates of the same material with a different width may exhibit a somewhat different crack growth resistance behavior.

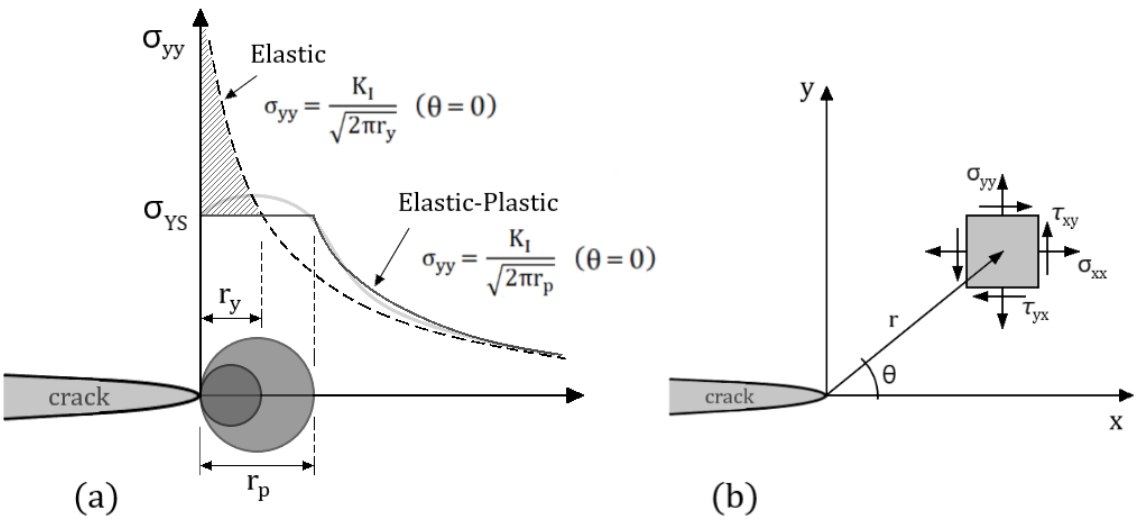

Figure 15. Crack-tip plasticity: a) Plastic zone and stress distribution at the crack tip. b) Definition of the coordinate axis ahead of a crack-tip. The z direction is normal to the page.

Figure 15 schematically presents the stress field in vicinity of a crack-tip in a linear elastic and elastic-plastic materials. The stress field in any linear elastic cracked body, such as represented in figure 15, is given by

$$\sigma_{ij} = \left(\frac{k}{\sqrt{r}}\right) f_{ij}(\theta) + \sum_{m=0}^{\infty} A_m r^{\frac{m}{2}} g_{ij}^{(m)}(\theta) \quad (8)$$

where σ_{ij} is a stress tensor

k is a proportionality constant

r and θ are as defined in figure 15

f_{ij} is a dimensionless function of θ in the leading term

A_m is the amplitude, and

$g_{ij}^{(m)}$ is a higher-order term, a dimensionless function of θ for the mth term.

The higher-order terms depend on geometry, but the solution for any given configuration contains a leading term that is proportional to $1 / \sqrt{r}$. As r $\rightarrow$ 0, the leading term approaches infinity, but the other terms remain finite or approach zero. Thus, regardless of the configuration of the cracked body, stress near the crack-tip varies with $1 / \sqrt{r}$, and displacement near the crack-tip varies with $\sqrt{r}$. Since stress is asymptotic to $r = 0$, equation (8) describes a stress *singularity*. A cracked body can be loaded in any one of the three modes of loading, or a combination of two or three modes. Each mode produces the $1 / \sqrt{r}$ *singularity* at the crack-tip, but the proportionality constants k and f_{ij} are mode dependent.

The proportionality constant k is replaced with *the stress intensity factor* K, which defines the amplitude of the crack-tip singularity as $K = k\sqrt{2\pi}$. Provided that the crack is stationary, all the stress and strain components near the crack-tip increase in proportion to K, and if K is known, all components of stress, strain, and displacement as a function of r and θ, can be solved. The mode of loading for stress intensity factor is usually denoted by a subscript K_I, K_{II}, or K_{III}. (Anderson 2005, pp. 42 – 45)

The stress field ahead of a crack-tip in an isotropic linear elastic material (under mode I loading) can be written as

$$\lim_{r \to 0} \sigma_{ij}^{(I)} = \frac{K_I}{\sqrt{2\pi r}} f_{ij}^{(I)}(\theta) \, . \quad (9)$$

When more than one loading mode is present, the principle of linear superposition applies and, the individual contributions to a given stress component are additive, that is

$$\sigma_{ij}^{(total)} = \sigma_{ij}^{(I)} + \sigma_{ij}^{(II)} + \sigma_{ij}^{(III)}. \quad (10)$$

Since all the stress components at all locations in linear elastic bodies increase in proportion to the remotely applied forces, the crack-tip stresses and K must also be proportional to the remote stress σ. This makes it possible to determine the stress intensity factor for a given body from remote loads and the geometry. (Anderson 2005, pp. 45 – 46, 95 – 97)

Much of fracture mechanics is based on the assumption that fracture toughness is a material property uninfluenced by the size of the structure, that is, the crack dimensions and plastic zone at the tip of a crack are thought to be negligible small compared to the dimensions of the structure and thus, crack-tip conditions are thought to be uninfluenced by external boundaries. Finite size of structures, however, sets some restrictions as the outer boundaries of a structure begin to exert an influence on the crack-tip as the crack size increases or the plate dimensions decrease. Defining a closed-form K solution for finite structures is usually not possible, but some techniques to approximate such boundary conditions do exist. Many stress intensity factor solutions for different kind of common configurations have been obtained from FEM analysis. For more complex configurations, stress intensity solutions can be built from simple cases for which the solutions are well established. This is possible since stress intensity factors, like the individual components of stress, strain, and displacement, are additive for linear elastic materials and the principle of superposition applies as long as the mode of loading is consistent. (Anderson 2005, pp. 48 – 50, 54 – 55) Although stress intensity factors are given in a variety of forms, K can always be related to the closed-form solution for K_I for a through crack in an infinite plate subjected to a remote tensile stress provided by Westergaard (1939) through the appropriate correction factor

$$K_{(I,II,III)} = Y\sigma\sqrt{\pi a} \quad (11)$$

where σ and a are the characteristic stress and characteristic crack dimensions, respectively, and Y is a dimensionless constant that depends on the geometry and the mode of loading (Anderson 2005, p. 53). For an example, K_I solution for a single-edge-

notched bend (SENB) specimen, the same form as used on fracture testing standards, such as ISO 12135 and ASTM E1821, to calculate K, is as follows

$$K_{\mathrm{I}} = \frac{F}{B\sqrt{W}}\left[\frac{3\frac{S}{W}\sqrt{\frac{a}{W}}}{2\left(1+2\frac{a}{W}\right)\left(1-\frac{a}{W}\right)^{3/2}}\right]\left[1.99 - \frac{a}{W}\left(1-\frac{a}{W}\right)\left\{2.15 - 3.93\left(\frac{a}{W}\right) + 2.7\left(\frac{a}{W}\right)^{2}\right\}\right] \quad (12)$$

where F is the applied force, B and W are the thickness and width of the specimen, respectively, and S is the span between outer loading points in a three-point bend test, also illustrated in figure 16.

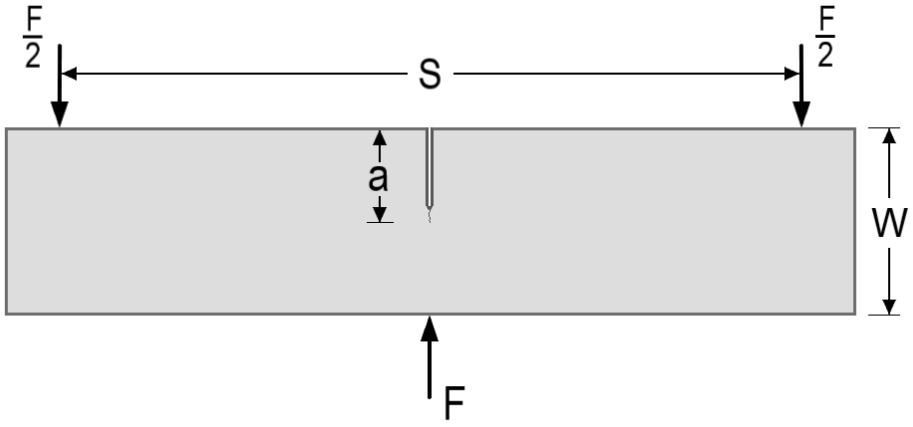

Figure 16. Single-edge-notched bend specimen.

At the point where stresses and strains in the material reach a state when material fails locally, stress intensity reaches a critical value K_{crit} or K_c, and crack extension occurs. K_c is a material constant, ideally independent of the size and geometry of the cracked body, and a measure of *fracture toughness*. The nomenclature for K_c is modified to include the loading mode, e. g. K_{Ic} for mode I. (Anderson 2005, pp. 69 – 71)

Both parameters G and K describe the behavior of a crack. The energy release rate describes the global behavior of a crack as it quantifies the net change in potential energy that accompanies an increment of crack extension, and the stress intensity factor is a local parameter that characterizes the stresses, strains, and displacements near the crack-tip.

Relationship between G and K_I for linearly elastic materials is

$$G = \frac{K_I^2}{E'} \tag{13}$$

where E' is E (Young's modulus) for plane stress and $\frac{E}{1-\nu^2}$ for plane strain, where ν is Poisson's ratio. The significance of this relationship is, that it connects the global energy concept to the more easily calculatable crack-tip parameter. Because of the relation between stress intensity and energy release rate, G also provides a single-parameter description of crack-tip conditions and the critical value G_c can be perceived as an alternative measure of FT for linear elastic material. (Anderson 2005, p. 58 – 61)

When evaluating measured K_c values for specimens with altering thicknesses, there seems to be an apparent thickness dependence of toughness in certain materials: the measured K_{crit} values decrease with increasing specimen thickness until a plateau is reached, after which the toughness appears relatively insensitive to further increase in thickness. The stress intensity toughness value obtained from this plateau region is referred to as *plane strain fracture toughness* K_{Ic} and is assumed to be a (specimen)size-independent material property. Generally the specimens that exhibit a decrease in apparent toughness with increasing specimen thickness correspond to materials in which the crack propagation is ductile and crack tunneling occurs: Because of the higher stresses in the region of high triaxiality, a crack growth is faster at the center of the specimen and lags behind on the outer regions where triaxiality is lower. The resulting fracture surface appears relatively flat in the center region, while shear lips are formed to the edges as fracture occurs at a 45° angle to the applied load, illustrated in figure 17. Fracture toughness tests on very thin specimens typically result in a 45° shear fracture, while at larger thicknesses, there is generally some mixture of both shear and flat fracture. This apparent thickness dependence is due to the relative portions of flat and shear fracture. The stress distribution illustrated in Figure 10 is typical for all section thicknesses, thus a central plane strain region exists even in thin specimens, as long as the distance from the crack-tip is sufficiently small. However, if the distance over which high triaxiality conditions exist is smaller than the fracture process zone, pure slant fracture occurs. The fracture process zone, where the micromechanical processes that lead to ductile crack extensions occur, is a function of microstructural parameters such as inclusion spacing and thus, is usually much smaller than the plastic zone. In very thin specimens, plane strain conditions do not exist at fracture process zone, but as the thickness increases, the size of the plane strain

zone increases relative to the low triaxiality zone near the free surfaces, resulting in varying fracture surface morphology with the specimen thickness, as illustrated in figure 17. The apparent thickness dependence of fracture toughness thus reflects the relative contributions of two distinct fracture mechanisms. Additionally, it might be worth mentioning, that there is no such thing as “plane stress fracture” (except perhaps in very thin foil) and there is nearly always some level of triaxiality along the crack front. (Anderson 2005, pp. 75 – 77)

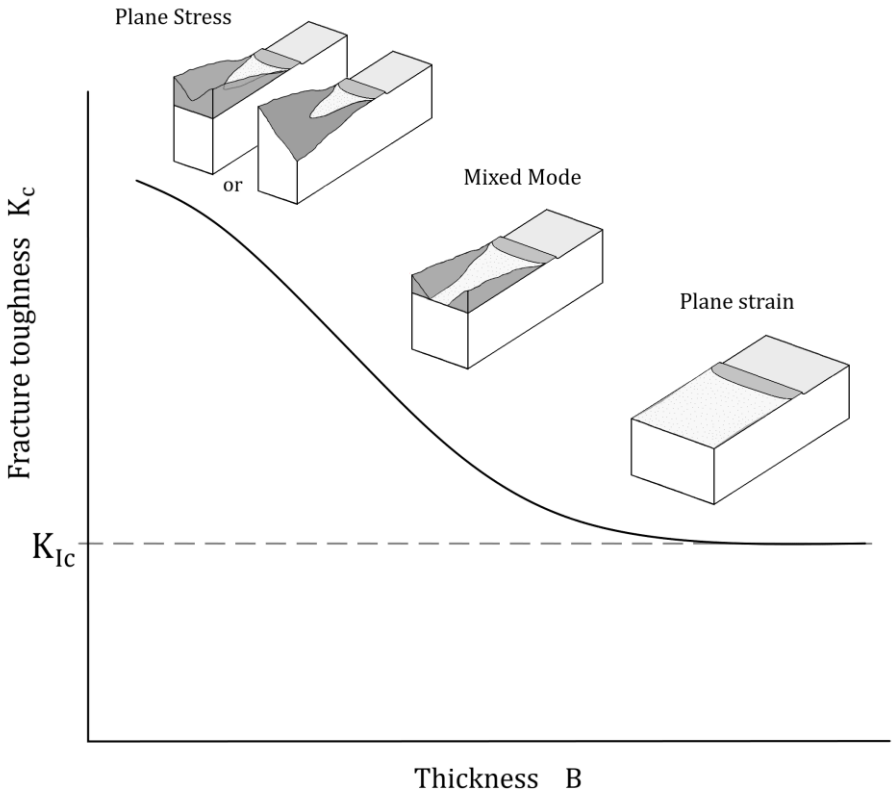

Figure 17. Effect of specimen thickness on fracture toughness.

Nowadays as fracture toughness testing is performed to materials that exhibit ductile crack growth, and where shear lips cause the apparent thickness dependence of toughness, side-grooved specimens are typically used. This specimen design eliminates shear lips thus providing an accurate measure of the resistance of the material to flat, ductile fracture. Though fracture toughness specimens that fail by cleavage usually do not form shear lips, cleavage FT does exhibit a slight thickness-dependence due to weakest link sampling effects. (Anderson 2005, pp. 77 – 78)

The following size requirements for K_{Ic} testing on standard specimens, have been adopted in ISO 12135:

$$a, B, (W - a) \geq 2.5 \left(\frac{K_{Ic}}{\sigma_{YS}}\right)^2. \quad (14)$$

Recall that the quantity $(K_I/\sigma_{YS})^2$ is proportional to the plastic zone size. The minimum requirements for the crack length and ligament length (W – a) are designed to ensure that the plastic zone is sufficiently small for fracture to be K-controlled. The thickness requirement in turn, is based on experimental data and is intended to ensure plane strain conditions along the crack front, although, the apparent thickness dependence in fracture toughness results from the relative mixtures of flat and shear fractures and could be eliminated by side-grooving. Also, it is far more stringent than actually necessary to ensure plane strain conditions along the majority of the crack front. Hence, the real reason for size criterion in the K_{Ic} standard stems purely from the need to be able to determine the fracture toughness based solely on load, which requires that the specimen be globally in the linear elastic regime. When this is not the case and excess plasticity occurs, the fracture toughness based on load underestimates the true fracture toughness. (Anderson 2005, p. 79; Wallin 2011, p. 34) In fact, the above presented requirement for a and B have been removed from corresponding ASTM standard E399 (2019), while for the ligament length it is still valid.

K is a fracture parameter that uniquely characterizes crack-tip conditions when the plastic zone at the crack-tip remains small and inside of the singularity-dominated zone. $1/\sqrt{r}$ singularity applies only to linear elastic materials and does not consider plasticity or other types of nonlinear materials behavior at the crack-tip. This means that equations for stress field components defined for isotropic, linear elastic materials do not describe the stress distribution inside the plastic zone. Fracture may not nucleate in the singularity zone, because the microscopic events that lead to fracture usually occur within the plastic zone, even if the zone is very small. However, K still uniquely characterizes crack-tip conditions as long as the plastic zone remains inside the singularity-dominated zone, i.e., in a region where the stress varies as $1/\sqrt{r}$. This is because the size of the plastic zone and the stress distribution inside the area (a free-body diagram construction), where boundary conditions are set by $1/\sqrt{r}$ singularity, are a function only of the boundary conditions and material property. (Anderson 2005, pp. 69 – 70)

2.2.3 Elastic – Plastic Fracture Mechanics

Since the theorems of linear elastic fracture mechanics only apply to materials where nonlinear material behavior, i.e. plastic deformation, is confined to a very small region surrounding the crack-tip, characterizing fracture behavior of materials, which exhibit such behavior, e. g. structural steels, becomes virtually impossible by the means of LEFM. To account for fracture behavior of materials that exhibit time-independent, nonlinear behavior, parameters of elastic-plastic fracture mechanics (EPFM) were derived.

Crack-tip opening displacement (CTOD) serves an engineering fracture parameter which can be used to describe both brittle and ductile failure in practical applications (Zhu & McGaughy 2018 p. 1). Wells (1963) was the first to propose the opening at the crack-tip as a measure of fracture toughness (Zhu & Joyce 2012, p. 3). While examining fracture behavior of structural steel specimens he observed that plastic deformation blunts an initially sharp crack prior to fracture and the degree of blunting increases in proportion to the toughness of the material. He related CTOD to K in the limit of small-scale yielding, through an approximate analysis utilizing Irwin's plastic zone adjustment. Irwin had postulated that the crack-tip plasticity makes the crack behave as if it were slightly longer and introduced the use of an effective crack length of $a + r_y$, where r_y is the displacement behind the effective crack-tip, as illustrated in figure 18.

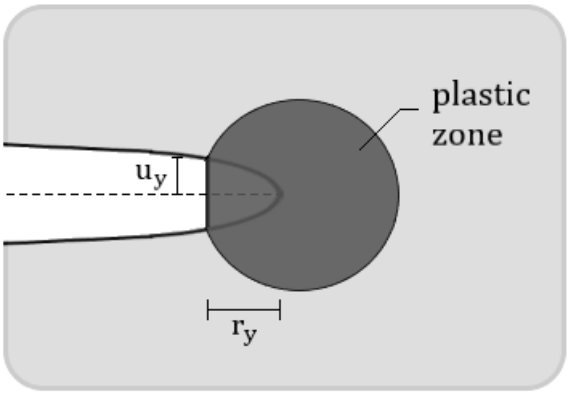

Figure 18. Estimation of CTOD from the displacement of the effective crack in the Irwin plastic zone correction.

Wells' estimate for CTOD is given by

$$\delta = 2u_y = \frac{4}{\pi}\frac{K_I^2}{\sigma_{YS}E} \tag{15}$$

where δ is the CTOD and u_y is a displacement as illustrated in figure 18. CTOD can further be related to G by application of equation (13)

$$\delta = \frac{4}{\pi}\frac{G}{\sigma_{YS}}. \tag{16}$$

Thus, he came to conclude that, as both G and K are related to CTOD in the limit of small-scale yielding, CTOD is an appropriate parameter to characterize crack-tip conditions when LEFM is no longer valid. (Anderson 2005, p. 103 – 104)

Another means to analyze CTOD is provided by the strip-yield model, where CTOD is defined as the crack-opening displacement at the end of the strip-yield zone. CTOD as derived from the strip-yield model, as $\sigma/\sigma_{YS} \rightarrow 0$, is given by

$$\delta = \frac{K_I^2}{\sigma_{YS}E} = \frac{G}{\sigma_{YS}} \tag{17}$$

which differs slightly from estimations concluded by Wells. The strip-yield model, however, assumes plane stress conditions and a nonhardening material, but the actual relationship between CTOD, K_I and G depends on the stress state and strain hardening of the material. The more general form of the relationship is expressed as

$$\delta = \frac{K_I^2}{m\sigma_{YS}E'} = \frac{G}{m\sigma_{YS}} \tag{18}$$

where m is a dimensionless constant known as constrain factor.

Several alternative definitions for CTOD exist, but the two most common ones are the displacement at the original crack-tip and the 90° intercept, of which the latter, suggested by Rice, is commonly used to infer CTOD in finite element measurements (Zhu & McGaughy 2018 p. 2). It is also worth mentioning that if the crack blunts in a semicircle, the two definitions are equivalent. Figure 19 illustrates these two definitions for CTOD. (Anderson 2005, pp. 104 – 105)

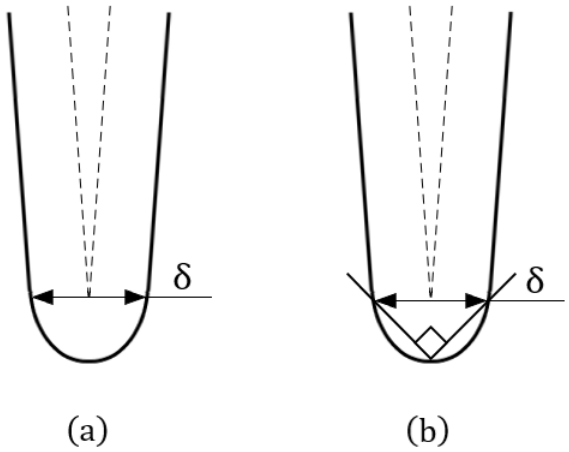

Figure 19. Alternative definitions of CTOD: (a) displacement at the original crack-tip and (b) displacement at the intersection of a 90° vertex with the crack flanks.

Today, most laboratory measurements of CTOD are made on edge-cracked specimens, loaded in three-point bending, and by measuring the opening displacement at the crack mouth (CMOD or V) with a clip gauge. CTOD is inferred from measured value of V by assuming the specimen halves are rigid and rotate about a hinge point, see figure 20. CTOD can be estimated from a similar triangles construction as follows

$$\frac{\delta}{r(W-a)} = \frac{V}{r(W-a)+a} \quad \rightarrow \quad \delta = \frac{r(W-a)V}{r(W-a)+a} \tag{19}$$

where r is a dimensionless constant between 0 and 1, and W is the width of the edge-notched bend specimen, as illustrated in figure 20. (Anderson 2005, pp. 105 – 106; Zhu & McGaughy 2018 p. 2)

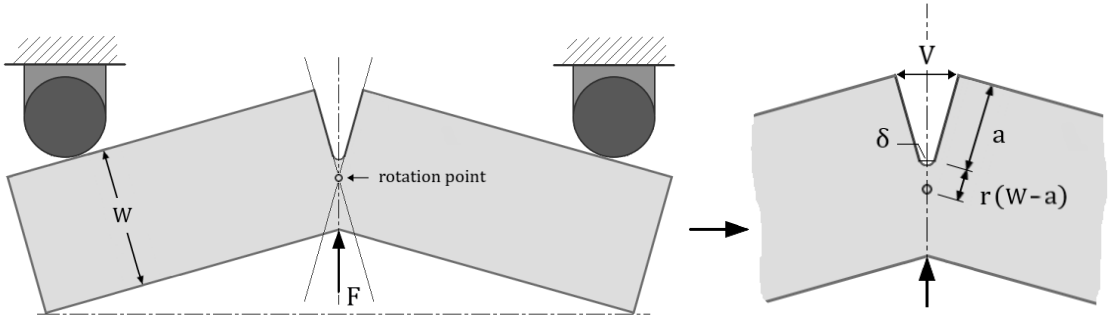

Figure 20. Principle of the hinge model for estimating CTOD from three-point bend specimen.

Because the hinge model is inaccurate when displacements are primarily elastic, a modified hinge model is typically adopted in standard methods for testing CTOD. In standard method analysis the displacements are separated into elastic and plastic components and the hinge assumption is applied only to plastic displacements

$$\delta = \delta_{el} + \delta_{pl} = \frac{K_I^2}{m\sigma_{YS}E'} = \frac{r_p(W-a)V_p}{r_p(W-a)+a} \quad (20)$$

where subscripts el and pl denote elastic and plastic components, respectively, K_I is the elastic stress intensity factor, calculated by inserting the load and specimen dimensions into the expression obtained from finite element analysis for selected specimen configuration, and r_p is the plastic rotational factor, which depends on crack size and specimen type and which for typical materials and test specimens, is approximately 0.44. (Anderson 2005, pp. 105 – 107; Zhu & McGaughy 2018 p. 3) In the latest ISO standards ISO 12135 and ISO 15653, a value of r_p = 0.43 has been adopted. However, both experimental and numerical investigations have shown that r_p is not in fact a constant during bending, but strongly depends on the a/W ratio and material strain hardening when a/W < 0,45 (Zhu & McGaughy 2018 p. 3). With the application of double clip gage (DCG) method to measure CTOD, the use of r_p correction becomes unnecessary however (Zhu & McGaughy 2018 p. 1).

Rice (1968) provided the basis for extending fracture mechanics methodology beyond the validity limits of LEFM. He idealized the elastic-plastic deformation as nonlinear elastic and defined a term *deformation plasticity* to describe this behavior which relates total strains to stresses in a material. This idealized material behavior is depicted in figure 21 where the uniaxial stress-strain behavior of both nonlinear elastic and elastic-plastic material is presented. The two display identical loading behavior as the stresses increase monotonically in both materials, but as unloading occurs, the material responses differ significantly from one another. (Anderson 2005, pp. 107 – 108)

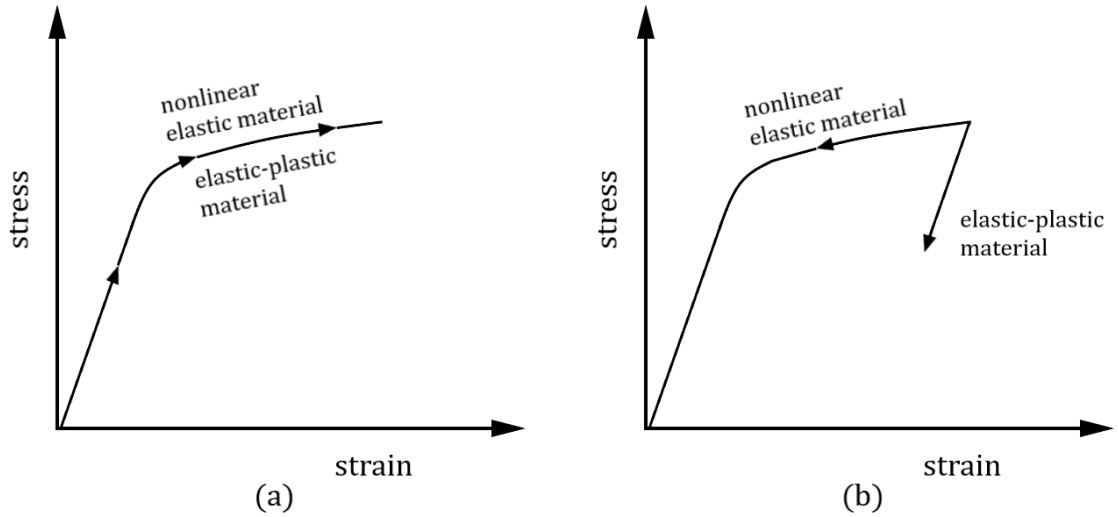

Figure 21. Schematic presentation of the stress-strain behavior of nonlinear elastic and elastic-plastic materials during a) loading and b) unloading.

While the nonlinear elastic material unloads along the same path it was loaded, the elastic-plastic material follows a linear unloading path with a slope equal to Young's modulus. So, while there is a unique relationship between stress and strain in an elastic material, in an elastic-plastic material the stress for given strain can take on different values if the material is unloaded or cyclically loaded. Thus, an analysis for an elastic-plastic material that assumes nonlinear elastic behavior may only be valid providing unloading does not occur. Also, as the problem is generalized to three dimensions, the loading behavior of nonlinear elastic and elastic-plastic materials may not necessarily be identical, but there are instances where this is a good assumption. (Anderson 2005, pp. 107 – 108)

Rice applied the principles of deformation plasticity to the analysis of a crack in a nonlinear material and introduced a new parameter, the J contour integral for analysis of cracks. He also provided a mathematical proof that the value of *J-integral* is independent of the path of integration around the crack, and later showed that the value of J-integral is equal to the energy release rate in a nonlinear elastic body containing a crack. (Anderson 2005, pp. 107 – 108, 156 – 159)

The energy release rate definition, equation (2), for linear materials holds also for nonlinear elastic materials, with the difference that G is replaced by J

$$J = -\frac{d\Pi}{dA}, \tag{21}$$

where A is the crack area and Π is the potential energy that is given by

$$\Pi = U - F, \tag{22}$$

where U is the strain energy stored in the body and F is the work done by external forces. Comparison of J values derived for a cracked plate in either load or displacement control leads to a conclusion that, since the difference between the strain energy values for the two cases is vanishingly small compared to overall strain energy, J for load control is equal to J for displacement control. The same result was obtained earlier for G, thus, J can be perceived as a more general version of the energy release rate. For a linear elastic material $J = G$, and for linear elastic mode I loading

$$J = \frac{K_I^2}{E'}. \tag{23}$$

However, the energy release rate concept has a rather different interpretation for elastic-plastic materials than for elastic material, where the energy release rate is usually defined as the potential energy released from the structure as the crack grows. In an elastic-plastic material a plastic wake is formed behind a growing crack and much of the strain energy absorbed is not recover as the crack grows or the specimen is unloaded. Thus, J is rather related to the difference in energy absorbed by specimens with neighboring crack sizes, though, the distinction between the two definitions is important only as the crack grows. (Anderson 2005, pp. 108 – 110)

Nonlinear elastic material behavior can be idealized by assuming a Ramberg-Osgood power law relationship between plastic strain and stress for a strain hardening material (Hutchinson 1968; Rice and Rosengren 1968). By expressing the stress solution as an infinite series and noting the stipulation for path-independency of J, it can be concluded, that the leading term in the series becomes proportional to $r^{-1/n+1}$ and dominates as $r \rightarrow 0$. This proportionality of the stress and strain distributions at the crack-tip is known as *the HRR singularity*, named after Hutchinson, Rice and Rosengren. Just like the stress intensity factor K characterizes the amplitude of the linear elastic singularity, the J

integral defines the amplitude of the HRR singularity and thus completely describes the stress conditions within the plastic zone where the linear elastic solution is invalid. Thus, a structure in small-scale yielding has two singularity-dominated zones, see figure 22: one in the elastic region, where stress varies as $1/\sqrt{r}$, and another in the plastic zone where stress varies as $r^{-1/n+1}$. The latter often persist long after the first one mentioned has been gulfed by the growing plastic zone at the crack-tip. (Anderson 2005, pp. 111 – 114, 159 – 162)

The HRR singularity solution dominates only very near the crack-tip, well within the plastic zone, but does not persist all the way to the tip. This is because the HRR solution is based on the small strain theory, which breaks down at strains greater than approximately 10 %, and therefore does not consider large strains near the crack-tip or effects caused by crack-tip blunting, which reduces the triaxiality locally. The finite strain region, where large deformations invalidate the HRR theory, occurs within approximately 2δ from the crack-tip. As the plastic zone size increases, the higher-order terms in the series become significant and loading often becomes nonproportional. This means a single-parameter description may no longer be possible and J no longer characterizes the crack-tip conditions adequately when crack-tip blunting occurs. However, similarly as with the validity of K as a crack-tip stress field describing parameter, as long as there is a region surrounding the crack-tip where stress fields can be described by the HRR singularity, J integral uniquely characterizes crack-tip conditions and a critical value J_c can be perceived as a size independent measure of fracture toughness. (Anderson 2005, pp. 111 – 114, 128, 159 – 162)

For linear elastic materials, calculation of J is relatively simple since $J = G$ and G can be computed from the load and crack size, assuming a K solution for chosen configuration is available. For a nonlinear material, however, the principle of superposition no longer applies and J is no more proportional to the applied load, thus a simple solution relating J, load and crack length, is usually not available. A generalized equation, expressing the J integral for a variety of configurations, can be written in the following form

$$J = \frac{\eta U_c}{Bb}, \tag{24}$$

where η is a plastic geometry factor that depends on the a/W ratio and specimen type (Zhu & McGaughy 2018 p. 4), U_c is the energy absorbed, B is the thickness of the

specimen and b is the length of the ligament in front of the growing crack. The generalized equation must further be separated into elastic and plastic components to apply for both elastic and elastic-plastic conditions (Zhu & McGaughy 2018 p. 3), that is

$$J = \frac{\eta_{el} U_{c(el)}}{Bb} + \frac{\eta_p U_p}{Bb}$$

$$= \frac{K_I^2}{E'} + \frac{\eta_p U_p}{Bb} \tag{25}$$

where subscripts el and p denote elastic and plastic components, respectively. (Anderson 2005, pp. 114 – 119) Additionally, because the J-integral was defined in terms of deformation theory of plasticity, the J estimation equation needs to be correct for crack growth for a quasistatic or growing crack (Zhu & McGaughy 2018 p. 4).

In the limit of small-scale yielding, the relationship between J and CTOD can be derived from the linear elastic relationship between CTOD and G, see equation (18), and from the notion that for linear elastic material $J = G$. Thus,

$$J = m\sigma_{YS}\delta \,, \tag{26}$$

where m is a dimensionless constant (constrain factor) that depends on the stress state and material properties. The term J-controlled fracture corresponds to a situation where the crack-tip conditions are completely characterized by J. Because of the unique relationship between J and CTOD, a J-controlled fracture implies a CTOD-controlled fracture. Though the relationships mentioned above are derived from LEFM theory, they have been shown to apply well beyond the validity limits of LEFM (Shih, 1981, p. 323) and thus, both J and CTOD parameters can be applied in the elastic-plastic regime. (Anderson 2005, pp. 120 – 123)

It is important to point out though, that the J-dominance at the crack-tip does not require the existence of a HRR singularity which is merely one possible solution to the more general requirement that J uniquely define crack-tip conditions. In reality, the flow properties of most materials do not conform to the idealization of a Ramberg-Osgood power law, upon which the HRR analysis is based. The leading term of the power law solution presented by Hutchinson, dominates as r → 0, but the higher-order terms become significant for moderate values of r and the computed stress field still scales with $J/(\sigma_0 r)$

though it deviates from the HRR field. J-dominance therefore does not necessarily imply agreement with the HRR fields. (Anderson 2005, p. 130)

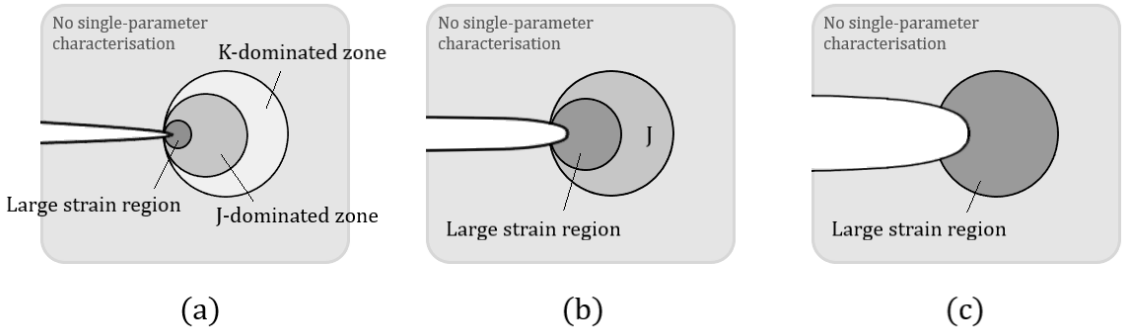

Figure 22. Effect of plasticity on the crack-tip stress fields: (a) small-scale yielding, (b) elastic-plastic conditions, and (c) large-scale yielding.

Figure 22 schematically illustrates the effect of plasticity on the crack-tip stresses of a stationary crack. Figure 22 (a) represents a small-scale yielding case, where both K and J -dominated region exist, and finite strain region, where the HRR theory is invalidated by large deformations, occurs within approximately 2δ from the crack-tip. Both K and J (CTOD as well) are valid parameters to characterize the crack-tip conditions in small-scale yielding. Figure 22 (b) in turn shows the elastic-plastic conditions, where J-dominated zone still persist but K-dominated region has disappeared as the plastic zone size has increased. Thus, J remains as an approximately valid parameter to characterize the crack-tip conditions as well as CTOD. Figure 22 (c) illustrates large-scale yielding. The size of the finite strain region has become significant relative to in-plane dimensions and the crack-tip conditions have evolved from plane strain to plane stress as the plastic zone size has grown to significant fraction of the thickness. The region uniquely characterized by J has disappeared. In large-scale yielding a single-parameter description of crack-tip conditions is no longer valid and the critical values of J exhibit a size and geometry dependence. For some configurations, where the K and J zones are vanishingly small, a single-parameter description is not possible except at very low loads. However, a single-parameter FM may be approximately valid even in the presence of significant plasticity if high level of triaxiality is maintained. (Anderson 2005, p.133)

As well as large plastic strains, also crack growth poses a problem for the calculations of J, since the equations (24) and (25) derived from the pseudo energy release rate definition of J are valid only for a stationary crack. When excessive plasticity or significant crack growth occurs in an elastic-plastic material, some of the energy that would be released is absorbed during deformation or is dissipated in a plastic wake that forms behind a growing crack. Also the specimen becomes less stiff and the compliance increases as the crack grows (Zhu and Joyce, 2012 p. 19). Thus fracture toughness and J – CTOD relationship become depended on the size and geometry of the structure or test specimen and critical values at instability can no longer be treated as a material property. (Anderson 2005, pp. 126 – 128) Therefore, when significant crack growth or plasticity occur, R-curves provide a better description of the fracture behavior of the material.

2.3 Fracture toughness testing

Various methods for evaluating fracture behavior have been developed over the years. Qualitative tests are quick and easy to execute and are well suited for internal quality control in production facilities but are not particularly accurate and do not describe the actual fracture properties of the material with sufficient accuracy. Methods based on fracture mechanics, on the other hand, are more accurate, but also much more complex and time consuming as well as more expensive to carry out (Presno-Vélez et al. 2019, p. 2). On the other hand, the ever growing need to pursue the most accurate methods to meet today's increasingly demanding design challenges, the importance of FM-based methods has been emphasized and are a subject of a growing interest.

2.3.1 Methods

The most common qualitative tests to evaluate material’s fracture properties still in use today are the Charpy impact test, Izod impact test and the Pellini drop weight test (also drop weight tear and dynamic tear tests). Both methods are still widely applied to structural materials. These methods provide a qualitative indication of material toughness and are cheaper and easier to perform than fracture mechanics based methods, but they lack the same mathematical precision and predictive capabilities. (Anderson 2005, pp. 340 – 341)

Charpy is a pendulum impact test that measures the energy of separation in notched metallic specimens. The procedure was first developed at the beginning of 20th century and it is still the most common standard test to evaluate material's fracture properties. Testing is conducted on relatively small specimens that do not consume much material and the test itself is quick and simple to perform making it a cost effective method for fracture testing. The most common notch geometries used today are the V- and the U-notch and the choice of notch configuration is usually connected to material type. For structural steels that exhibit ductile-to-brittle transition, such as ferritic steels, the V-notch is commonly used, whereas for brittle materials, such as cast irons, or tough materials like austenitic stainless steels, the U-notch is the normally chosen design. The main parameter determined in the test is the energy required to fracture the specimen. This fracture energy is believed to be indicative of a material's resistance to brittle fracture. The deficiency of a Charpy test is that it does not distinguish between the different events related to the fracture process, that is, the relative amounts of energy that is absorbed between crack initiation, propagation and the plastic deformation of the specimen cannot be determined. Both ASTM and ISO have provided standard methods for conducting the Charpy test. The Izod impact test is a variant of the Charpy impact test. The Charpy specimen is a simple notched beam that is impacted in three-point bending and the Izod specimen is a cantilever beam that is fixed at one end and impacted at the other. The main differences between Charpy test and FM test are that Charpy employs a blunt notch, while FM specimens have sharp fatigue cracks, Charpy uses subsize specimens which has a lower constraint compared to FM specimens, and Charpy applies impact loading, whereas most FM test are conducted under quasistatic conditions. These differences preclude forming simple relationships between qualitative and quantitative measures of fracture. Attempts on transforming the results from a simple Charpy test to be applied for FM based fracture toughness evaluations, with sufficient accuracy, have been studied over the years, but are yet to be seen. However, quantitative information from fatigue precracked Charpy specimens can be obtained if the impact striker is properly instrumented. Such an experiment turns essentially to a subsize dynamic FT test. (Wallin 2011, pp. 259 – 263; Anderson 2005, pp. 340 – 342; Presno-Vélez et al. 2019)

The Pellini drop weight test provides a qualitative measure of crack arrest toughness. The test was developed in 1950s and is still applied for structural materials. The procedure has been standardized by the ASTM and involves impacting a drop weight on a plate specimen with a notch in a brittle weld bead in three-point bending. A cleavage crack

initiates at the starter notch and either propagates into the parent metal or arrest, depending on material properties and temperature. In the test, a nil-ductility transition temperature (NDTT) is determined by performing a sequence of drop weight tests over a range of temperatures in small increments until a temperature at which two no-break results can be obtained is reached. Thus determined NDTT provides a qualitative estimate of crack arrest toughness above which an arrest is more likely to occur. (Anderson 2005, pp. 341 – 344; Hannula et al. 2020b, pp. 194 – 195)

Quantitative methods for assessing material's fracture properties are based on fracture mechanics and material behavioral aspects that were reviewed in chapters 2.1 and 2.2. These methods address material fracture in terms of fracture toughness and measure the resistance of a material to crack extension under quasistatic loading. These methods are further discussed in the following chapters which concern the most commonly used standard procedures.

2.3.2 Standards

A variety of standardized procedures for fracture toughness measurements have been published by different organizations throughout the world. The first standards for K and J testing were developed by the American Society for Testing and Materials (ASTM) in 1970 and 1981, respectively, and the first CTOD test method was published by the British Standards Institution (BSI) in 1979. The International Institute of Standards (ISO) and The Japan Welding Engineering Society (JWES/WES) have published their own standardized procedures as well. All of these existing fracture toughness standards are broadly consistent with one another, usually differing in minor details, and evolve continuously as the technology develops and more experience is gained. Today, the most widely used ones throughout the world are probably those published by ASTM and ISO, and the majority of fracture tests are conducted according to standards ISO 12135, ISO 15653 (for welds), ASTM E1820 and ASTM E1921. (Anderson 2005, p. 299; Zhu & McGaughy 2018, p. 3 – 5)

Majority of the standards for fracture toughness testing include several common features. Most have similar specimen designs and importance of addressing the specimen orientation relative to symmetry directions is emphasized. The five most commonly used specimen design types that are featured in standards are illustrated in figure 23. No single standard allows the use of all five figurations, however (Zhu & Joyce 2012, p. 6). The

vast majority of the tests are performed on single-edge-notched bend (SENB) and compact tension (CT) type specimens. In each standard, the test pieces are precracked by fatigue before testing, although the requirements for fatigue loads vary between standards. The basic instrumentation required for measuring load and displacement is common to most tests, though some do require additional instrumentation to monitor crack growth. (Anderson 2005, pp. 22, 299 – 300; ISO 12135 2021; ISO 15653 2018; ASTM E1820 2022; ASTM E1921 2022)

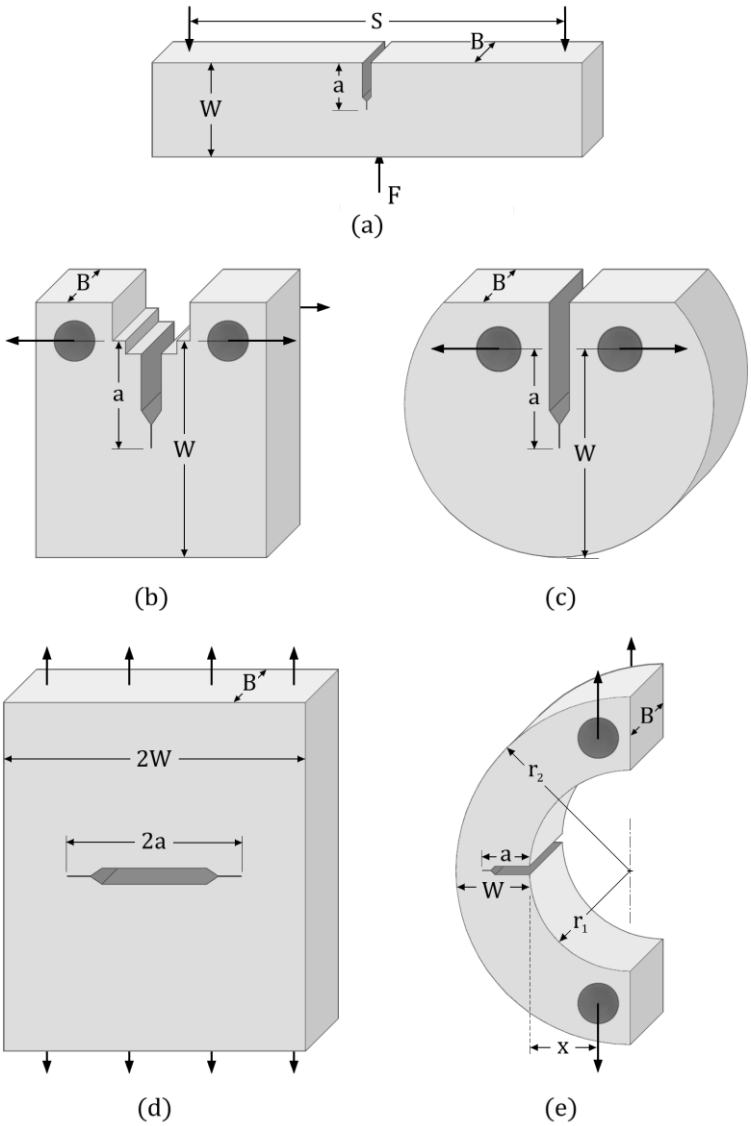

Figure 23. Standardized fracture mechanics test specimens: (a) single edge-notched bend (SEN(B)) specimen, (b) compact tension (C(T)), (c) disk-shaped compact tension (DC(T)), (d) middle-cracked tension(M(T) panel, and arc-shaped tension (A(T)) specimen.

2.3.3 ISO 12135 and ASTM E1820

The standard ISO 12135 provides a unified method for determining FT in terms of K, J, δ and R-curves for homogeneous metallic materials subjected to quasistatic loading. The first edition of this standard was published in December 2002 (corrected in January 2008), the second edition in November 2016 and the latest version, the third edition, in July 2021 (corrected in august 2022)(ISO 2023). Some corrections, additions and improvements have been made over the years as more knowledge and experience has been gained in the field, but the essentials of the standard have remained the same since the launch of the first edition. The most notable change to the earlier version is the replacement of formulae to calculate CTOD with those based on rigid rotation assumption throughout the standard, meaning, in the latest version, the formulae for CTOD calculations for determining R-curves is now also based on rigid rotation assumption whereas in the earlier edition it was based on CTOD values determined from J. Also the CTOD formulae for SENB specimens is now corrected for the material yield to tensile strength ratio, i.e. considering the variation of crack-tip blunting due to strain hardening, as based on recent research. This new correction was proposed by Kawabata et al. (2016) as a solution for the already well established (see, e.g. Tagawa et al. 2010; Tagawa et al. 2014) fact that when examining highly strain hardening steels, CTOD values obtained with the previous formulae were overly unconservative. The same correction had already been implemented a few years earlier (2018) to the ISO 15653 for welds.

The ASTM standard for measurement of fracture toughness dates further back than the corresponding ISO standard ISO 12135. Since the early 1970s, ASTM had over the years published several different fracture toughness standards for the different FT parameters, first being the E399-72 for the plane strain fracture toughness at or near to the onset of crack initiation, K_{Ic}. To follow were the E813-81 for the J-integral testing and E1152-82 for the J-R curves testing, both published in 1982, that later, in 1996, merged into a single standard E1737-96. In 1989 ASTM published a CTOD test standard E1290-89 similar to the earlier (1979) published BS 5762 standard by British Standards Institution, which adopted the plastic hinge model for the estimation of critical δ_c from CMOD measurements. ASTM E1820-96 was the first standard to combine these different standards to a single common test procedure for measurement of all these different fracture parameters. The first version of ASTM E1820(-96) was published in 1997 and has since undergone a series of revisions, the latest being the current version E1820-23, which was published in March 2023 just a year apart from the previous version, which

was also still active at the time of drafting of this thesis. In 1993, Kirk and Dodds showed that the J-converted CTOD values were insensitive to material strain hardening. Subsequently, in 2005, E1820 discarded the plastic hinge model and adopted the J conversion to determine the critical δ_c value, as it was felt as a better approach to tackle the issue of extending the standard to shallow crack geometries (Zhu and Joyce, 2012, p. 32).

In short, both standards provide a unified method of test for the determination of fracture toughness that characterizes the material's resistance to crack extension. Depending upon the level of plasticity realized in the specimen during the test, fracture toughness is presented either in terms of specific, single point values (that define the onset of unstable crack extension or describe stable crack extension or ductile crack instability) or a continuous curve relating fracture resistance to crack extension over a limited range of crack extension (in cases where crack grows in a stable manner under ductile tearing conditions). The standards provide both the procedure for determining specific point values and alternative procedures for R-curve determination. Regardless of the predicted outcome, all specimens are notched, fatigue precracked, and tested under slowly increasing displacement while measuring the displacements and forces realized during the test. The measured values are then used in conjunction with some pre- and post-test specimen measurements to determine the fracture toughness of the chosen material. The advantage of the test procedure for determining point values is that the test can be performed even to an unknown material without any prior assumption about its fracture behavior (provided that the tensile properties of said material are known or can be determined), and the most suitable parameters to characterize its fracture behavior can be selected according to the observed material response during the test.

The standards also provide general information, instructions and requirements on fracture parameters, test specimens, specimen preparation (material condition, crack plane orientation, machining), fatigue precracking, side-grooving, pre-test measurements, test apparatus (calibration, force application, displacement measurement, test fixtures), test requirements (test temperature, recording, testing rates and analysis), post-test measurements and reporting of the results as well as some additional information and instructions regarding the aforementioned (matters) in the appendixes included.

Fracture parameters determined by the methods covered by the standards ISO 12135 and ASTM E1820 are shown in table 1. Corresponding parameters can be found on both standards, with the exception of the K_{Ic} parameter, which has been removed from the E1820 standard to avoid duplication among similar ASTM standards, and for which the reader is hence advised to refer to ASTM E399 instead (ASTM E1820-22). K_{Ic}, δ_c, J_c, δ_u, J_u, δ_{uc}, J_{uc}, δ_m and J_m, of which the parameter K_{Ic} (in ISO 12135) is considered a size insensitive value and the rest as size sensitive i.e. specific for the thickness tested, are point values determined through the basic procedure. Initiation parameters $\delta_{0,2BL}$ and $J_{0,2BL}$ (ISO) and corresponding parameters δ_{Ic} and J_{Ic} (ASTM) in turn are determined graphically from δ-Δa and J-Δa resistance curves, respectively, which are either determined through multiple- or single-specimen procedures. Multiple-specimen procedure involves testing on series of at least six nominally identical specimens, which are loaded to selected displacement levels, each providing a data point on the R-curve. The corresponding amounts of crack extension are then measured and corresponding values of δ or J determined. The data may then be used in tabular form or as a plotted graph to form the R-curve from which parameters $K_{J0,2BL}$, $\delta_{0,2BL}$ and $J_{0,2BL}$ can be graphically determined. Single-specimen procedure in turn enables determining the R-curve by making use of elastic compliance or other techniques, such as electrical potential techniques, to obtain multiple points on the R-curve from the test of a single specimen. The parameters $K_{J0,2BL}$ and K_{JIc} can then be evaluated from the predetermined $J_{0,2BL}$ and J_{Ic} values, respectively. ISO 12135 also covers two additional parameters, the initiation toughness parameters δ_i and J_i, which are determined by performing stretch zone width (SZW) measurement for fracture tested specimens using scanning electron microscopy (SEM) and by combining these results with the data from δ-Δa or J-Δa determination procedures. (ISO 12135 2021; ASTM E1820 2022)

Table 1. Fracture toughness symbols from the standards ISO 12135 and ASTM E1820.

Parameter	Size insensitive quantities	Size sensitive quantities (specific to thickness B tested)
K	K_{Ic} $K_{J0,2BL}$	
δ	δ_i (ISO), δ_{Ic} (ASTM) $\delta_{0,2BL}$	$\delta_{c(B)}$ $\delta_{0,2BL(B)}$ $\delta_{u(B)}$, $\delta_{uc(B)}$, $\delta_{m(B)}$ (ISO)
J	J_i $J_{0,2BL}$	$J_{c(B)}$ $J_{0,2BL(B)}$ $J_{u(B)}$, $J_{uc(B)}$, $J_{m(B)}$ (ISO)

Both standards allow the use of two specimen designs, CT and SENB, and provides proportional dimension and tolerance requirements for both, as well as other details regarding the specimens design, machining, fixtures, fatigue precracking, etc. ASTM E1821 also includes the disc-shaped compact DC(T) specimen design, but only the two designs included in both standards are addressed here, although many aspects discussed here apply for the DC(T) design as well. The bend specimen design maintains a relatively high level of triaxiality (high constraint) under fully plastic conditions such that the crack-tip conditions are similar to the small-scale yielding case, meaning, even in the presence of significant plasticity (and well beyond the general yield load), a single-parameter description of fracture toughness persists approximately valid as the specimen remains in contained yielding. This explains why most laboratory measurements of fracture toughness are performed with bend-type specimens, such as the compact and three-point bend geometries: it is simply because these specimen types present the fewest experimental difficulties (Anderson 2005, pp. 133 – 134, Wallin 2011, p.72).

The two specimen types have other benefits as well. Both designs are quite simple and thus easy and quick to machine. The compact geometry consumes less material and may thus be more economical when testing plate material or forging, although it requires some extra material in width direction due to the pinning holes. On the other hand, since the compact specimen is pin-loaded by special clevises and requires separate testing fixtures for each specimen size, it usually limits the number of specimen sizes that can be tested. Also, friction between the loading pins and the sample is a common error source with CT specimens and may affect the measured compliance by up to 10% (Wallin 2011, p. 79). The simple geometry of SENB specimen, in turn, may be preferable for weldment testing as it consumes less weld metal in some orientations. Also the fixture for SENB specimen testing is usually designed such a way that it can be adjusted continuously to any value within its capacity in order to correspond the standard loading span of 4W, thus making it possible to test a wider range of specimen dimensions with a single fixture. (Anderson 2005, p. 301) Both bend designs have historically been considered to produce similar FT values, but since the CT specimen has a slightly higher geometrical constraint than the SENB specimen, SENB specimens tend to yield higher fracture toughness values than CT specimens. However, since the bend specimen types have generally higher constraint than any structural component, they both provide conservative estimates of fracture toughness for structural integrity purposes. (Wallin 2011, p. 160 – 161)

As the CT specimen is pin-loaded in tension, it experiences close to 85% bending load and 15 % tension load. The actual proportions between bending and tension components depend on the crack length. The bending component that the ligament experiences increases proportionally, the longer the crack length is. Also, CT specimens are poorly suited for shallow flaw testing as it has a second axis of moment, which encourages the crack to deviate from the fatigue crack plane, especially if the material is textured and has weak planes. Other problem with testing shallow cracks is that the load on the pins grow large very easily. SENB specimens, however, are not as prone to non-planar crack growth as they lack the tensile component and are hence better suited for shallow crack testing. The major error source in SENB testing in turn comes from friction, rotation and sliding of the outer roller pins. The movement of outer rolls will reduce span length in large displacements, whereas for very large displacements, the rolls may start to glide causing an increase in the span length. (Wallin 2011, pp. 77 – 79, 90)

The standards recommend the use of a specimen width-to-thickness ratio (W/B) of 2 as preferred for both allowed specimen designs, but allows values ranging from 1 to 4 for bend specimens. For compact specimens ISO standard allows values ranging from 0,8 to 4 and ASTM from 2 to 4. As stated in the ISO standard, evidence gained over the years has suggested that specimen proportions of W/B = 4 yields slightly higher R-curves than the lesser proportions of W/B = 2. This is mainly due to the crack tunneling effect, which is enhanced in slim samples where, in a plane-sided specimen, the ductile crack growth is suppressed at the side surfaces and occurs mainly in the center of the specimen. This results in a steepening of the tearing resistance curve and increases the value of stress intensity for maximum load. However, this only becomes a problem when the crack growth is significantly larger than 2 % and can be avoided with the use of side-grooving. (Wallin 2011, pp. 31 – 33)

The standards set some limits and requirements for crack starter notch geometries as well. The dimensional requirements for the machined notch are designed such as to promote nucleation of a stable and uniform crack in a delimited area during fatiguing, as required for fracture testing (Presno-Vélez et al. 2019, p. 2). The minimum length requirement for the fatigue precrack, in turn, is designed such as to ensure the fatigue crack front effectively samples enough grains to smear out the microstructural variability of the material, thereby attaining similitude conditions necessary for the application of the theorems of LEFM and/or EPFM for fracture toughness determination (Castelluccio &

McDowell 2016, p. 521). The crack geometry also affects the number of grains required along the crack front to reach this condition. As stated on the standards, the allowed ratio between the initial crack length a, consisting of the machined starter notch and fatigue precrack, and specimen width W is $0{,}45 \leq a/W \leq 0{,}70$ except for the K_{Ic} determination, when $0{,}45 \leq a/W \leq 0{,}55$ is required by the ISO standard. K_{Ic} determination has been removed from the ASTM E1820-22 standard in order to avoid duplication, and the user is advised to refer to the standard ASTM E399 where the ratio $a/W = 0{,}5$ is recommended. Crack length influences elastic-plastic fracture toughness in two ways, through the proportional crack length, which affects the overall constraint of the specimen, and through the absolute ligament length, which affects the measuring capacity of the specimen. Effect of proportional crack length is not the same for both ductile and brittle fracture, but shows a similar trend, that is, short cracks tend to produce higher fracture toughness values compared to long cracks. Also, it is only marginal for ductile tearing resistance curve with crack lengths larger than $a/W \geq 0{,}5$ and for the ductile fracture toughness values close to initiation. The proportional crack length effect is usually enhanced with high strength materials. For standard geometry bend specimens, the loss of constraint is almost entirely controlled by the absolute ligament length, which controls the specimens measuring capacity with respect to the fracture mechanical parameters in question. The thickness of a specimen starts to affect constraint only after the loss of constraint due to ligament size has occurred. Since fracture toughness measuring capacity is dependent on the fracture mechanism, the effects of absolute ligament length on brittle and ductile fracture are not the same, but opposite. After the measuring capacity is exceeded, the brittle fracture toughness increases, whereas the ductile tearing resistance usually decreases. (Wallin 2011, p. 58 – 59, 157 – 158)

Specimens should be machined from material in its finally heat treated and/or mechanically worked condition (ISO 12135; ASTM E1820). The anisotropy of engineering materials must be taken consideration when choosing the specimen orientation, as the microstructural, and consequently mechanical properties of a material are often sensitive to direction. This sensitivity to orientation affects the fracture toughness measurements, since the microstructure in the preferred orientation may contain planes of weakness, making crack propagation relatively easy. If the purpose of the test is a general material characterization or screening, a low toughness orientation, where crack propagates in the rolling direction, that is, T – L or S – L, should be chosen (see figure 24), whereas, if the purpose is to simulate conditions of a specific flawed

structure, the chosen crack orientation should match that of the structural flaw. (Anderson 2005, pp. 301, 303)

It has also been pointed out (Wallin et al. 2015; Neimitz et al. 2014) that UHSS steels may exhibit non-homogeneity of the fracture properties through the thickness of the plate. This is suggested by Neimitz et al. (2014) to be due to microstructural variations through the plate thickness caused by the thermo-mechanical treatments (tempering) applied in order to achieve those high strength properties pursued after. What this suggests, is that if one were to extract specimens of different thicknesses in the T – L direction, this would lead to an apparent size effect, if the thin specimens concentrate to the weaker center region of the plate. Thus, in order to guarantee the specimens crack fronts lie in similar material, either T – S or L – S orientation should be applied. However, also the geometrical constraints must be considered as they may preclude some orientations. For an example, S – T and S – L orientations may only be practical in thick sections, as well as T – S or L – S orientations, especially if integral knife edges are to be used. (Anderson 2005, p. 303) Considering the aforementioned, and assuming the fracture toughness results to be measured are to be used for structural life assessment, meaning the as-conservative-a-result-as-possible is preferred, perhaps the low toughness T – L orientation should be preferred, at least, when the specimen thickness B can be fitted to the thickness of the plate to be tested.

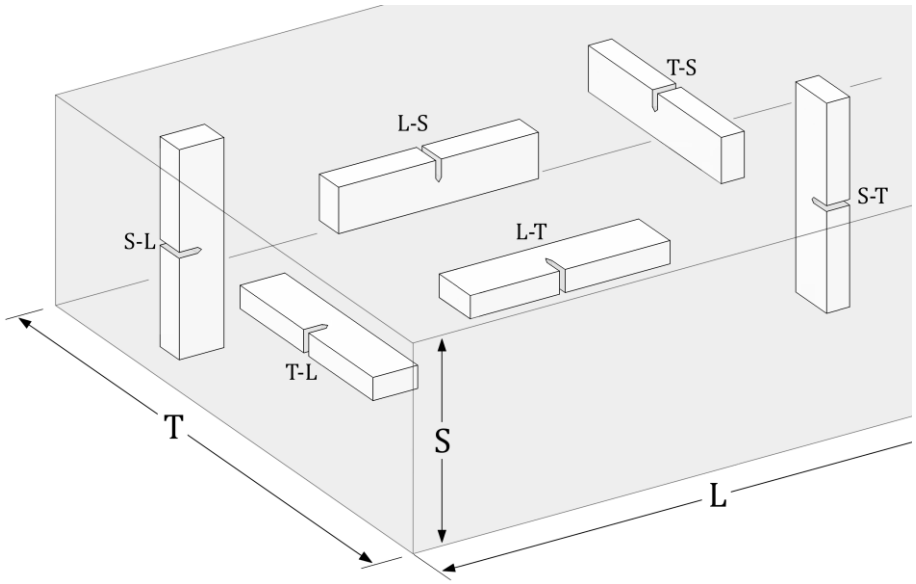

Figure 24. Crack plane orientations (basic identification), where L = Longitudinal direction (direction of principal deformation/maximum grain flow), S = Short transverse direction (direction of least deformation) and T = Transverse direction (direction normal to L-S plane). Note that the orientations L-T-S in standards ISO12135 and ISO15653 are marked by X-Y-Z and N-P-Z, respectively.

Both standards also address the use of side-grooving with some minor detail differences. Side-grooving can be done to avoid shear lips and crack tunneling, thereby to diminish crack front bowing. However, the use of too steep side grooves produces lateral singularities which cause the crack to grow more rapidly at the outer edges and thus should be concerned. (Anderson 2005, pp. 307 – 308) Hence the standards have set some limiting factors to be followed. ISO 12135 standard states that specimens for the determination of point values may be either plane-sided or side-grooved but the specimens for R-curve testing shall all be side-grooved. ASTM E1820 in turn highly recommends that side-grooving is done when the compliance method of crack size prediction is implemented. Both standards state, that side-grooving shall be carried out after fatigue precracking. However, the ISO standard allows shallow side grooves (i.e. less than 5 %) prior to fatiguing, if done as an aid to precracking some materials, and are to be extended to their full depth after fatiguing. Rather similar limiting values for the total thickness reduction (0.2B – 0.25B), and for the root radii and included angles of the side grooves are also set in the standards.

Specimens for fracture testing must be precracked by fatigue before fracture testing. This is done in order to create a sufficiently sharp crack to adequately satisfy the validity of fracture mechanics theory that applies only to infinitely sharp cracks impossible to produce in practice. As straight a crack front as achievable is desired in order to ensure comparatively uniform stress state along the entire crack front (Wallin, 2011 p. 422). The most efficient way to produce such a crack is by cyclic loading. (Anderson 2005, p. 303) The ratio of minimum-to-maximum force ($R = \frac{F_{fmin}}{F_{fmax}}$) in the fatigue cycle shall be in the range of 0 to 0.1 except that to expedite crack initiation one or more cycles of R = – 1.0 may be first applied. Also the maximum allowed force applied during fatigue precracking is determined from equations provided in the standards. The force maximum value is determined to ensure that the plastic zone, which inevitably forms during fatiguing, does not grow as large as to significantly affect the material characterizing FT values determined in the fracture test. Because the crack produced during cyclic loading also has a finite radius, it must be made sure that the crack-tip radius at failure is larger than the initial fatigue crack radius in order for the fracture toughness to reflect true material properties. (Anderson 2005, p. 304)

The crack mouth opening displacement (CMOD or V) measurements are carried out with a displacement gauge, such as an extensometer, that can be attached to the specimen with knife-edges either integral or attached. The standards also provide instructions for measuring the load-line displacements if appropriate. The observed displacements during the test are recorded as well as corresponding force data.

After the test, specimens are broken open and the initial crack length a_0 is measured from the fracture surfaces of failed specimens. Measurements are carried out as instructed in the standard and the value of a_0 is obtained using the nine-point averaging procedure where first the two surface measurements made at positions 0.001B inward from the surface (or from the side groove roots) are averaged, and then averaging these values with the sum of the seven equispaced inner measurements as follows:

$$a_0 = \frac{1}{8}\left(\frac{a_1+a_9}{2} + \sum_{i=2}^{8} a_i\right). \quad (27)$$

Measurement of the initial crack length a is the most remarkable error source for FT determination.

The measured initial crack length data, combined with the recorded force and displacement data, are used in calculations of the pursued fracture toughness parameters. Interpretation of the recorded test data and selection of the force and displacement values to be used in calculations depends on the material's observed fracture behavior during the test. Sometimes pop-in behavior is observed during the test. The term *pop-in* refers to an abrupt discontinuity in the force – displacement record, typically featuring a sudden increase in the displacement record and, generally, a simultaneous drop of force, after which the test record may continue on to higher forces and increased displacements still. If a pop-in results from an arrested unstable brittle crack extension in the plane of the precrack, the corresponding results must be considered as characteristic of the material tested and need to be considered in calculations. Pop-in behavior may also arise from other sources, such as delaminations or splits normal to the precrack plane, roller or pin slippage in bend or compact specimen load trains, respectively, improper seating of displacement gauges in knife edges, ice cracking in low-temperature testing, or electrical interference in the instrument circuitry of force and displacement measuring and recording devices, in which case it can be ignored. Examination of fracture surface may be needed to establish the cause of a pop-in, although not insisted in the standards except

for weld specimens. However, methods to evaluate the significance of pop-ins are presented in the standards.

The main differences between the standards lie in the calculation formulae for fracture toughness parameters. Formulae to calculate point values for K, and point and resistance curve values for J, are the same in both standards, but formulae for determination of CTOD differ from one another remarkably. In ISO standard the formulae to calculate CTOD are based on modified rigid rotation assumption, while in ASTM, CTOD is converted from J-integral. Additionally, J values are corrected for crack growth in the ASTM standard while in the ISO standard they are not. Based on this, fracture toughness values determined in terms of CTOD or J are likely to differ at some extent when calculated values are compared between the two standard methods. In fact, the difference between the CTOD results determined with different standards have been shown (Tagawa et al. 2010; Tagawa et al. 2014; Khor et al. 2017, pp. 12 – 13) to depend on material strain hardening rate or yield-to-tensile ratios, and the ASTM CTOD estimate has been shown to always provide underestimates when compared to actual CTOD values obtained with silicone rubber casting (SRC) impression method, thus providing slightly conservative values for CTOD. In a study conducted by Khor et al. (2017) it was observed that both the latest ISO and the ASTM estimate of CTOD gave consistent but conservative estimations of CTOD for materials with yield-to-tensile ratios between 0.44 to 0.98, with the latest ISO estimate being fractionally closer to the SRC values of CTOD as well as FEM modeled prediction of CTOD.

Other small differences between the standards can additionally be found on the specimen tolerance bounds and formulae for maximum fatigue precracking force. It is also worth to mention that the standards provide slightly different definitions for the theoretical elastic compliance used in calculations. Formulae for elastic compliance are otherwise the same, but in the ISO standard, plane strain stress state is applied, while in the ASTM, plane stress state is assumed. While the crack-tip region in detailed elastic-plastic finite element analysis has been found to be closer to plane strain, the global response of the specimen (measured by the compliance) is closer to plane stress. Wallin (2011, pp. 73, 196) also points out that it has been found most appropriate to use the plain stress form of modulus of elasticity in the compliance equations. In light of this, and since both standards allow the compliance to be referred from the measured load and displacement data, one should preferably apply the experimental compliance for calculations rather

than the calculated theoretical elastic compliance. ASTM E1820 also provides some other methods or means, which are not covered by the corresponding ISO standard, such as a method for rapid-load J-integral fracture toughness testing, a normalization data reduction technique, method for fracture toughness tests at impact loading rates using precracked Charpy-type specimens and guidelines for measuring FT of materials with shallow cracks. Although ISO 12135 does not cover shallow flaw FT testing, it is covered in the ISO 15356, which is a complementary document for the standard ISO 12135, and provides special testing requirements and analysis procedures necessary for the testing of weldments. ASTM has also published a similar standard for welds, ASTM E2818-11, which draws heavily from the corresponding ISO -standard (ISO 12135 (2021); ASTM E1820 (2022); ASTM).

2.3.4 ASTM E1921

When examining ferritic steels that undergo cleavage fracture in the ductile-to-brittle transition, both ASTM E1820 and ISO 12135 recommend the application of procedures proposed in ASTM E1921. The Master Curve (MC) Standard E1921 provides methods to characterize the fracture toughness scatter, statistical size effects and empirically found temperature dependence, both for the transition region and the lower shelf, with a single-parameter description (Walli, 2011, p. 117). The MC method was developed specifically to analyze data sets of highly variable cleavage fracture instability values to evaluate the ductile-to-brittle transition reference temperature T_0, which defines the onset of lower shelf cleavage behavior in ferritic structural steels (Zhu and Joyce 2012, p. 21), and corresponds to the temperature where a 25,4 mm thick specimen (1T) has the mean fracture toughness of 100 $MPam^{0,5}$ (Wallin et al. 2015, p. 219).

The test procedure follows the same pattern as in ISO 12135 and ASTM E1820, but a minimum of six uncensored individual tests is required for data analysis in this method. From the test results, the J-integral value J_c at instability, i.e. at onset of cleavage fracture, is calculated for each datum and converted into equivalent elastic-plastic stress intensity factor, K_{Jc}, values. Censoring limits are then applied to the K_{Jc} data, with respect to the measuring capacity of the specimens and in case cleavage fracture was preceded by stable crack growth. Scatter among individual test results is expected. Weakest link statistics combined with conditional cleavage propagation criterion are used to treat the data scatter and model specimen size effects in the transition range between lower shelf and upper shelf fracture toughness. Individual K_{Jc} values, both censored and uncensored, are size-

adjusted and converted to 1T size equivalents. Then a provisional T_0 value, T_{0Q}, is determined. If tests are conducted at multiple temperatures this requires application of an iterative procedure, but if all test are conducted at a single temperature, a direct evaluation of scale parameter K_0, median fracture toughness $K_{Jc(med)}$ and T_{0Q}, is possible. The basic temperature dependence expression for MC employs empirically determined constants, that were originally chosen such as to ensure a median fracture toughness of 100 $MPam^{0,5}$ at T_0. The standard MC with these fixed constants is applicable for steels with T_0 in the range -100 °C to +50 °C. In ASTM E1921 the MC is fitted to the data in the temperature range -50 °C < T_0 < +50 °C and will thus provide a satisfactory description of the fracture toughness in this temperature region. Hence, as long as test temperature T satisfies the condition -50 °C < T – T_{0Q} < +50 °C, the provisional T_{0Q} value can be considered as a valid T_0 value. Then a material homogeneity screening evaluation is performed to establish conservative lower bound type fracture toughness estimates, and to account for the increased uncertainty related to small data sets. After screening, the transition temperature curve, i.e. Master Curve, is established employing the tuned values derived from screening, if appropriate. Lastly, upper and lower tolerance bounds can be determined and margin adjusted, i.e. an upward temperature shift of the tolerance bound curve can be added, to cover the uncertainty associated with the use of only a few specimens to establish T_0. The Master Curve determined by this method can be used to define a transition temperature shift related to metallurgical damage mechanisms. (ASTM E1921 2022; Wallin 2011, pp. 152 – 156, 175 – 177)

3 MATERIALS AND METHODS

3.1 Materials

Fracture toughness of two steels, martensitic stainless steel, 1.4313, and a medium carbon tool steel, were studied in this work. Both are UHSS steels with tensile strengths of about 850 MPa and 1400 MPa, respectively. Both of these steels are quenched and tempered and have a martensitic microstructure, but 1.4313 is refed to as a soft martensitic steel whereas the medium-carbon steel is an engineering and tool steel, with a hardness of about 44 HRC. 1.4313 was chosen for this study, as it was the material examined in a proficiency test which DEKRA was to participate in. Also, it shall later be used in the company's quality control concerning this method. The other steel studied is a relatively novel material that cannot be found on standard material listings. It has a higher strength and hardness than the other chosen steel, with a same sort of microstructure and heat treatment history. Very little research data on the fracture toughness of base material seems to be available for this specific steel.

3.1.1 Martensitic stainless steel

Little information about the other test material was known before the tests. Material code 1.4313 was provided and could be found in seven different EN standards (SFS-EN 10028-7, SFS-EN 10088-1, SFS-EN 10088-2, SFS-EN 10088-3, SFS-EN 10272, SFS-EN 10250-4). Tensile properties at room temperature were revealed, but exact product form and condition were not provided. Material condition was assumed QT as deduced from the material code and the information listed in the standards which included the material. Tensile properties for the material, as provided by Institut für Eignungsprüfung GmbH (IfEP), are gathered in the table 4. Chemical composition of the material was as well deduced from the material code and is presented in table 5. Orientation of the 1.4313 samples was unknown as the sample blanks were delivered as premachined sample bars without notation of orientation.

Table 4. Mechanical properties of 1.4313 at room temperature, obtained from IfEP.

Tensile properties	Yield strength	Tensile strength	Young's modulus	Poisson's ratio	Elongation	Impact toughness	Hardness
Steel	$R_{p0.2}$ MPa	R_m MPa	E GPa	ν	A %	KV2 J	
1.4313 (X3CrNiMo13-4)	802	863	206	0.3	14	70	–

Table 5. Chemical compositions of 1.4313, obtained from SFS-EN 10028-7 (2006).

Chemical compositions	by mass								
	C	Si	Mn	P	S	Cr	Mo	Ni	N
Steel	≤ %	≤ %	≤ %	≤ %	≤ %	%	%	%	≥ %
1.4313 (X3CrNiMo13-4)	0.05	0.70	1.50	0.04	0.015	12.0 – 14.0	0.30 – 0.70	3.50 – 4.50	0.020

The material code 1.4313 corresponds to designation X3CrNiMo13-4. Equivalent grades include steels such as UNS S41500, F6NM, F 6NM, 13Cr-4Ni, UNS J91540, CA-6NM, SS 2384, UNS S42400, SCS5, X5CrNi13-4, and AISI 415. These steels are classified as martensitic stainless steels. 1.4313 has been reported to be a typical representative of the group of soft martensitic steels (Koster et al. 2013 p. 90). Generally, steels of this group (soft martensitic steels) are characterized by a low carbon content of around 0.05 wt% which leads to a decrease of hardness and to an increasing fracture toughness and corrosion resistance. They are also associated with a high strength combined with good ductility as well as good cavitation erosion resistance, excellent weldability and good castability (Koster et al. 2013 p. 90; Foroozmehr et al. 2017, p. 262; Thibault et al. 2014, p. 6). Due to their chemical composition, soft martensitic steels have been reported to generally undergo a martensitic transformation even when cooled in air. By performing additional heat treatments, a microstructure that consists mainly of martensitic, austenitic and ferritic phases can be achieved. The favorable, so called “tempered” martensitic microstructure, combines high strength with high strain at failure (Koster et al. 2013 p. 90). According to Foroozmehr et al. (2017), the microstructure of quenched and tempered 13Cr-4Ni/1.4313 steels typically consists of a combination of lath martensite, stable reformed austenite and a small amount of delta ferrite. In their study (2017) they found that the finely-dispersed austenite phase was in the form of lamellae located within the laths of martensitic matrix.

Due to their favorable properties, soft martensitic steels are often used for demanding applications where the material may be exposed to complex loading conditions in service, such as for production of pumps, compressors, centrifuges and turbines, in nuclear engineering, chemical engineering and for marine constructions (Koster et al. 2013 p. 90 – 91; Foroozmehr et al. 2017 p. 262).

Most of the studies conducted in recent years concerning X3CrNiMo13-4 steels have addressed fatigue related subject such as cyclic behavior, reformed austenite, effect on hydrogen embrittlement, brazed and weld joints and welding residual stresses (Hassanipour et al. 2016; Hassanipour et al. 2017; Thibault et al. 2011; Thibault et al 2014; Fan et al. 2017; Brück et al. 2018; Schindler et al. 2009; Ghafoori-Ahangar & Verreman 2019; Baser et al. 2010). Other studies also addressed welding, cavitation erosion, slurry erosion and corrosion behavior of these materials (Sarafan et al. 2017; Sarafan et al. 2020; Thibault et. al 2010; Wiednig & Enzinger 2017; Roa et al. 2021; Grewal et al. 2013). Studies where quasistatic fracture toughness had been investigated, though not many could be found, concerned welded and brazed joints as well as bulk material (Foroozmehr et al. 2017; Foroozmehr & Bocher, 2021; Leinenbach et al. 2010; Paucar Casas et al. 2009; Chen et al. 2013).

3.1.2 Medium-carbon ultrahigh-strength steel

The studied medium-carbon ultrahigh-strength steel is a modern typically quenched and tempered (QT) low alloyed engineering and tool steel with a fine-grained tempered martensitic structure. The fine lath martensitic structure and consequently the remarkably well mechanical properties of the steel, shown in Table 2, are obtained by meticulous choice of alloying elements combined with a careful selection of parameters for thermo-mechanical treatments (e.g. the temperature of hot plastic deformation or cooling rate)(Mandal et al. 2022; Nowacki et al. 2016; Ahlblom et al. 2007; Ozgowicz & Kalinowska-Ozgowicz 2008). The chemical composition is presented in Table 3. Mechanical properties and chemical composition for this steel were obtained from the material certificate.

Table 2. Mechanical properties of the studied medium-carbon ultrahigh-strength steel at room temperature, obtained from a material certificate.

Mechanical properties	Yield strength $R_{p0.2}$ MPa	Tensile strength R_m MPa	Young's modulus E GPa	Poisson's ratio ν	Elongation A200 %	Impact toughness Charpy-V J	Hardness HRC
Steel							
Medium-C tool steel	1284	1410	210	0.3	9	22	44

Table 3. Chemical composition of the studied medium-carbon ultrahigh-strength steel, obtained from a material certificate.

Chemical compositions	by mass								
	C %	Si %	Mn %	P %	S %	Cr %	Mo %	Ni %	N %
	0.32	1.06	0.79	0.008	0.001	1.35	0.795	0.67	0.004
Steel	V %	Ti %	Cu %	Al %	Nb %	B %			
Medium-C tool steel	0.138	0.011	0.02	0.003	0.017	0.002			

The steel seems to have been used mainly for manufacturing of plastic injection molds and forging dies, as well as pressure casting and plate forming tools. It is also stated to be suitable for machine components, wear-related parts, rail guides and applications at elevated temperatures (Ribeiro et al. 2021). Consequently it appears, that recent studies concerning this specific material have mainly been focused on subjects regarding either tool and mold/die (also micro-mold) manufacturing (i.e., machining, surface quality, microstructural changes, and wear and thermal fatigue resistance at elevated temperatures), or welding (Ribeiro et al. 2021; Schneider et al. 2008; Schneider et al. 2011; Hernandez et al. 2015). Studies conducted on similar steels seemed to concern same subjects as well (Nowacki et al. 2016; Mandolfino et al. 2013; Pijpers et al. 2007; Krum et al. 2017). Similarly, studies concerning fracture toughness testing conducted for similar steels, seem to be focused on weld details (Wallin et al. 2015), and only one was found where fracture toughness test was conducted only on similar base material (Melo et al. 2019). All and all, research material on this specific steel was scarce to be found and some seemed vague enough to be considered as a reliable research source.

3.2 Testing and fractography

SENB specimen design was chosen, as required for proficiency test, and the 1.4313 samples were machined to the nominal dimensions requested. Machining of 1.4313 samples was done in DEKRA's metals laboratory in Oulu, except for the EDM wire cutting (electrical discharge machining) of the starter notch, which was executed by the Future Manufacturing Technologies (FMT) group in ELME studio in Nivala. Machining of medium-carbon tool steel samples had been conducted earlier and samples were received as machined conforming to ASTM E1820. The 1.4313 sample blanks were delivered as premachined close to the target dimension, and orientation of the samples was not revealed. Orientation of the medium-carbon steel samples was L-T (see figure 24).

The nominal dimension for 1.4313 SENB specimens were thickness B = 15 mm, width W = 30 mm and span S = 120 mm (total length of the specimen was 138 mm). Starter notch was machined to a depth of about 13 mm and fatigue precracking was done in order to achieve a combined original crack length a_0 of 15 mm.

The nominal dimension for the medium-carbon steel SENB specimens were thickness B = 10 mm, width W = 20 mm and span S = 80 mm (total length of the specimen was 90 mm). Starter notch was machined to a depth of about 8 mm and fatigue precracking was done in order to achieve a combined original crack length a_0 of 10 mm.

Tensile properties at test temperature were determined from the room temperature tensile data with appropriate formulas, presented in the standard ISO 15653. The determined tensile properties for both studied steels are presented in table 6.

Table 6. Tensile properties for the studied ultrahigh-strength steels.

Test temperature	Tensile properties At room temperature		Tensile properties At test temperature	
0 °C	Yield strength	Ultimate tensile strenght	Yield strength	Ultimate tensile strenght
Steel	$R_{p0,2}$ [MPa]	R_m [MPa]	$R_{p0,2}$ [MPa]	R_m [MPa]
1.4313	802	863	817	887
Medium-C UHSS	1284	1410	1299	1449

Fatigue precracking of SENB specimens was performed at the University of Oulu with a Zwick / Roell Vibrophone 100 high-frequency pulsator using three-point bending fixtures. Fatiguing was performed in ambient room temperature. Maximum fatigue precracking force was determined according to ISO 12135 standard, and an appropriate value well below the determined maximum value was adopted for the actual maximum force value of prefatiguing.

Fracture toughness testing was also conducted at the University of Oulu with a Zwick / Roell Z100 universal testing machine using three-point bending fixtures. In total, five 1.4313 and eight medium-carbon steel samples were tested. Tests were carried out under crosshead-displacement control. Required ambient temperature for testing on low temperatures was achieved by using environmental chamber, Severn Thermal Solutions Model EC75D. Temperature for all tests performed was 0 °C as required for proficiency test. Crack mouth opening displacement CMOD was measured with a clip-on extensometer, Sandner EXRC5+6x. Test procedure was followed according to the instructions presented in the ISO 12135 standard for both materials. Consequently the requirements presented in the standard also satisfied the requirements of the ASTM E1820 standard. Calculations of CTOD for both test materials were done according to both ISO 12135 (as required by the proficiency test) and ASTM E1820 standards, whereas for the T_0 determination, the measured test results were dealt with according to the ASTM E1921 standard.

All samples were measured before the tests as required in ISO 12135. After tests samples were broken open and original crack lengths were measured from the fracture surfaces with a laser microscope as instructed in ISO 12135. Measured values for 1.4313 and the medium-carbon UHSS samples are combined in tables 7 and 8, respectively. For 1.4313 samples #3 and #4, fatigue crack length at one of the near-surface measuring points did not quite fulfill the minimum length requirement of 1,3 mm set in the ISO 12135 standard. For medium-carbon UHSS sample #1 fatigue crack length at any of the nine measuring points did not fulfill the minimum length requirement set in the ISO 12135 standard, neither did the fatigue crack lengths at both of the near-surface measuring points on sample #2. However, all the fatigue crack length measurements in all the tested samples fulfilled the minimum fatigue crack length requirements set in the ASTM E1820 standard. Thus none of the samples were excluded from further calculations in this thesis, although for the proficiency test, only valid results were submitted.

Table 7. Measured values for martensitic stainless steel samples.

Specimen	Dimensions				
	Thickness B [mm]	Width W [mm]	Span S [mm]	Crack length a_0 [mm]	a_0/W
1.4313 #1	15,082	30,02	120,00	14,78	0,49
1.4313 #2	15,068	30,08	120,00	14,70	0,49
1.4313 #3	15,028	30,08	120,00	14,67	0,49
1.4313 #4	15,065	30,07	120,00	14,82	0,49
1.4313 #5	15,036	30,06	120,00	14,67	0,49

Table 8. Measured values for the medium-carbon UHSS samples.

Specimen	Dimensions				
	Thickness B [mm]	Width W [mm]	Span S [mm]	Crack length a_0 [mm]	a_0/W
TS10 #1	10,04	19,99	80,00	8,90	0,45
TS10 #2	10,02	20,05	80,00	9,23	0,46
TS10 #3	10,00	19,99	80,00	9,88	0,49
TS10 #4	10,01	20,07	80,00	10,13	0,50
TS10 #5	9,99	20,05	80,00	9,85	0,49
TS10 #6	9,98	19,99	80,00	9,60	0,48
TS10 #7	10,00	20,00	80,00	9,91	0,50
TS10 #8	10,00	20,03	80,00	9,75	0,49

Fracture surfaces of one martensitic stainless steel (1.4313) sample and of three medium-carbon tool steel samples were examined with scanning electron microscope, Zeiss Σigma FESEM, to establish the fracture micromechanisms that occurred during the fracture tests.

4 RESULTS

4.1 Martensitic stainless steel

In 1.4313 samples fracture instability did not took place, but fracture occurred through stable tearing. The load – displacement curves obtained from the fracture toughness tests conducted on the 1.4313 samples are combined in figure 25. Force maximum values and corresponding displacement values for each sample are shown in table 9.

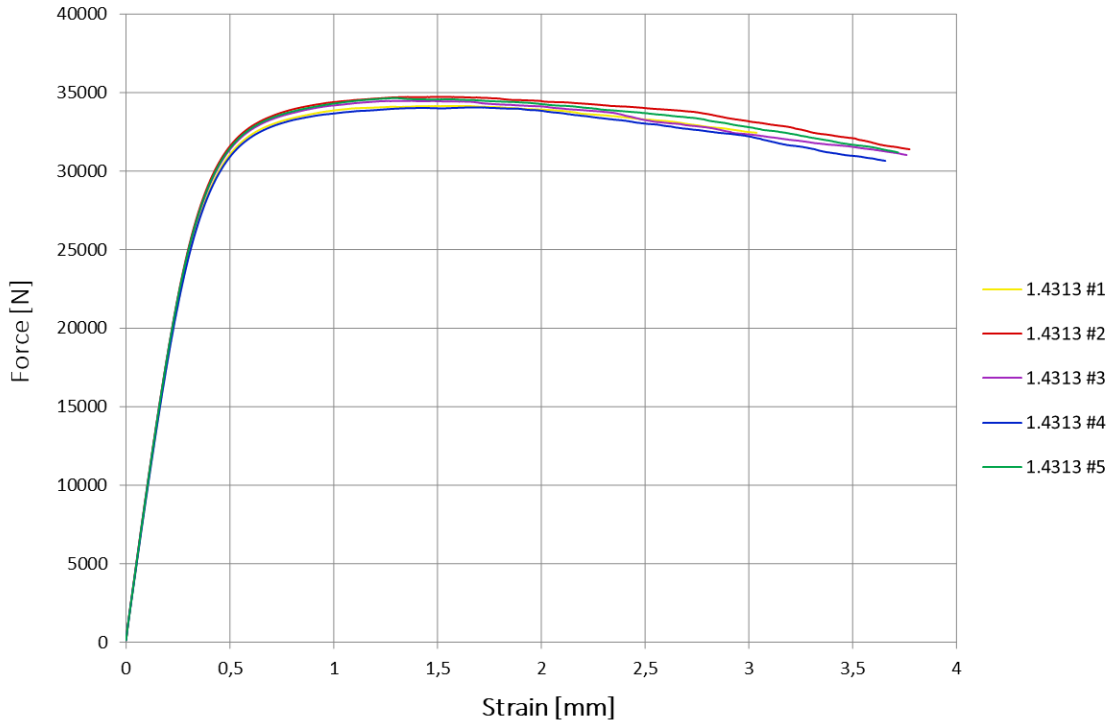

Figure 25. Load – displacement curves for 1.4313 samples.

For 1.4313 samples, CTOD was determined both according to ISO 12135 and according to ASTM E1820, see table 9. In samples #3 and #4, the measured fatigue precrack lengths at one of the near-surface measuring points did not meet the required 1.3 mm minimum length, thus marked with asterisk (*). However, as corresponding requirements in ASTM E1820 are not as strict, the minimum crack length requirements at all measuring points in all samples were easily met. For comparison, the CTOD determined according to the ISO standard has been calculated using both theoretical elastic compliance, C_{theo}, and experimental compliance, C_{exp}. Values calculated with the theoretical elastic compliance

yielded slightly larger estimates for CTOD. The CTOD calculated according to ASTM was determined through the J-integral, but unlike the standard states, the J values have not been corrected for crack growth Δa, because the final physical crack size a_f values had not been determined. However, had the J values been corrected for crack growth, the CTOD estimates would have decreased further from their current values. Results show that CTOD values determined according to ASTM E1820 provide more conservative estimates than values determined according to ISO 12135, which is in line with previously observed trend.

Table 9. Combined test data, and crack-tip opening displacement values calculated according to standards ISO 12135 and ASTM E1820.

Fracture toughness	Test data			ISO 12135		ASTM 1820
				with theor. elastic compliance	with experim. compliance	with experim. compliance
	Force	CMOD		CTOD	CTOD	CTOD
Specimen	F_{max}	V		$\delta_{m(15)}$	$\delta_{m(15)}$	δ
	[N]	[mm]		[mm]	[mm]	[mm]
1.4313	34414	1,50	Mean	0,449	0,433	0,350
			Median	0,454	0,439	0,356
			Standard deviation	0,054	0,054	0,044
1.4313 #1	34151	1,63		0,490	0,474	0,384
1.4313 #2	34733	1,51		0,454	0,439	0,356
1.4313 #3 *	34478	1,38		0,410	0,393	0,317
1.4313 #4 *	34057	1,70		0,511	0,494	0,400
1.4313 #5	34653	1,29		0,382	0,366	0,295

Calculations were also made to assess whether fracture toughness of 1.4313 could be evaluated by the MC method, although the observed ductile macroscopic behavior during fracture tests already suggests this to be unlikely. Calculated K_{Jc} values and corresponding limit values for each 1.4313 sample are gathered in table 10. As can be seen from the results, all of the calculated individual K_{Jc} values exceeded the corresponding $K_{Jclimit}$ values, indicating the method would not be suitable for this material, as expected. Hence calculations were not carried out further.

Table 10. Calculated K_{Jc} values and corresponding limit values for 1.4313 samples.

Specimen	Test data: Force F_{max} [N]	Test data: CMOD V [mm]	Calculated values: $K_{Jclimit}$ [MPa$\sqrt{m}$]	Calculated values: K_{Jc} [MPa$\sqrt{m}$]
1.4313 #1	34151,1	1,63	306,5	356,8
1.4313 #2	34732,9	1,51	307,9	343,3
1.4313 #3	34478,0	1,38	308,2	323,8
1.4313 #4	34057,2	1,70	306,6	364,2
1.4313 #5	34652,9	1,29	308,0	312,6

Since all 1.4313 samples showed rather similar behavior during the fracture test, only one sample was chosen for fracture surface examination. Fracture surface appearance obtained with FESEM can be seen in figures 26 – 28. Fracture surface examination confirmed that fracture mechanisms during the fracture test was ductile in this steel. Figure 26 shows an overview of the ductile fracture surface and figure 27 displays a closer view of the surface, where ductile dimples are shown more clearly.

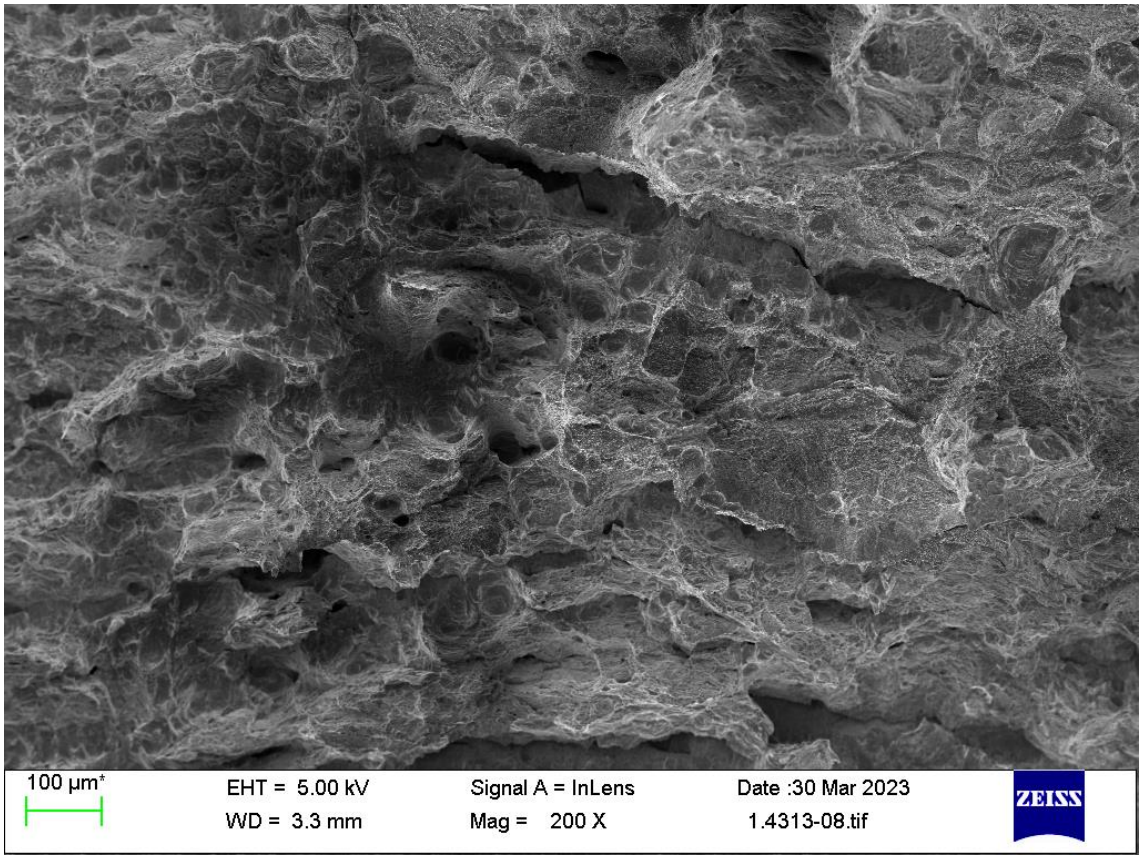

Figure 26. Overview of the fracture surface in martensitic stainless steel.

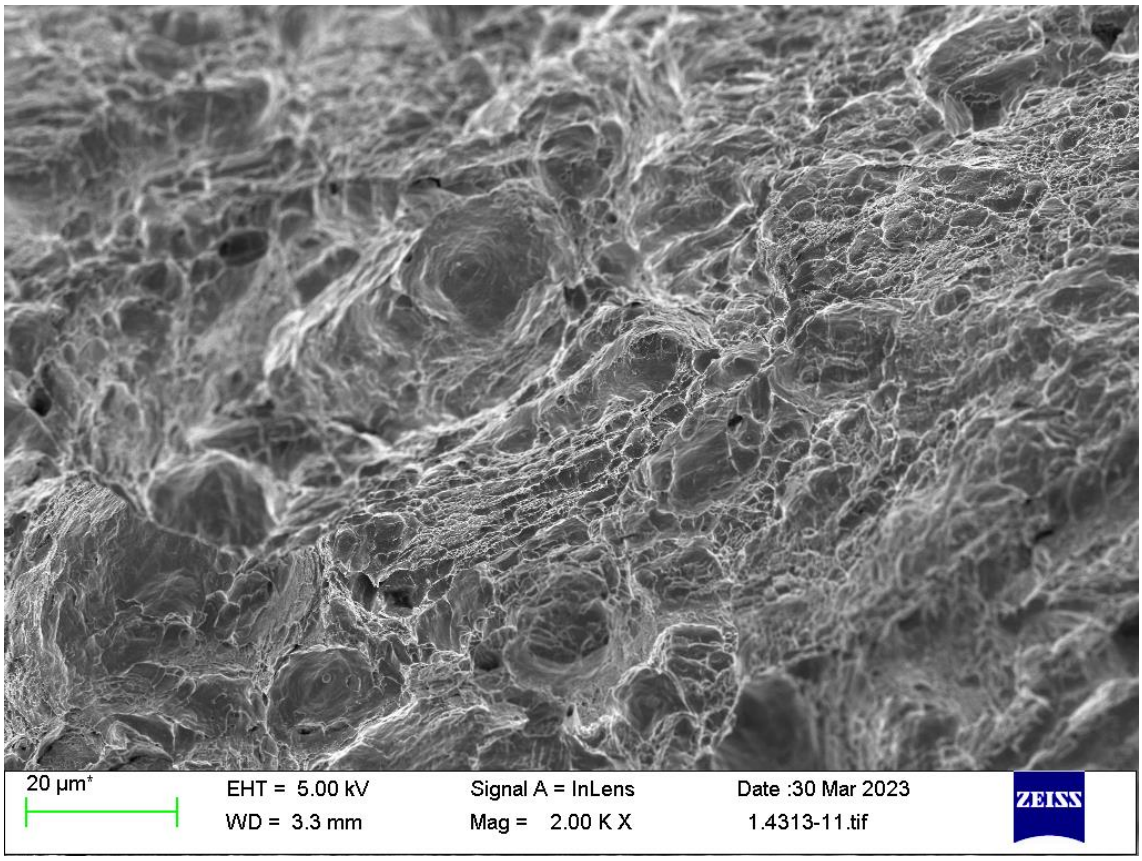

Figure 27. Close-up of the fracture surface with ductile dimples.

Crack propagation during the test is demonstrated in figure 28. SEM pictures (a) and (c) in figure 28 are taken from outer regions of the sample, about 2 – 3 mm inward from outer surfaces, as schematically illustrated, and (b) is combined from two different pictures taken from the center region and shows the length of the crack propagation in the middle of the sample. As can be observed, crack growth during the test in the center area of the sample was clearly faster compared to growth in the outer regions of the sample.

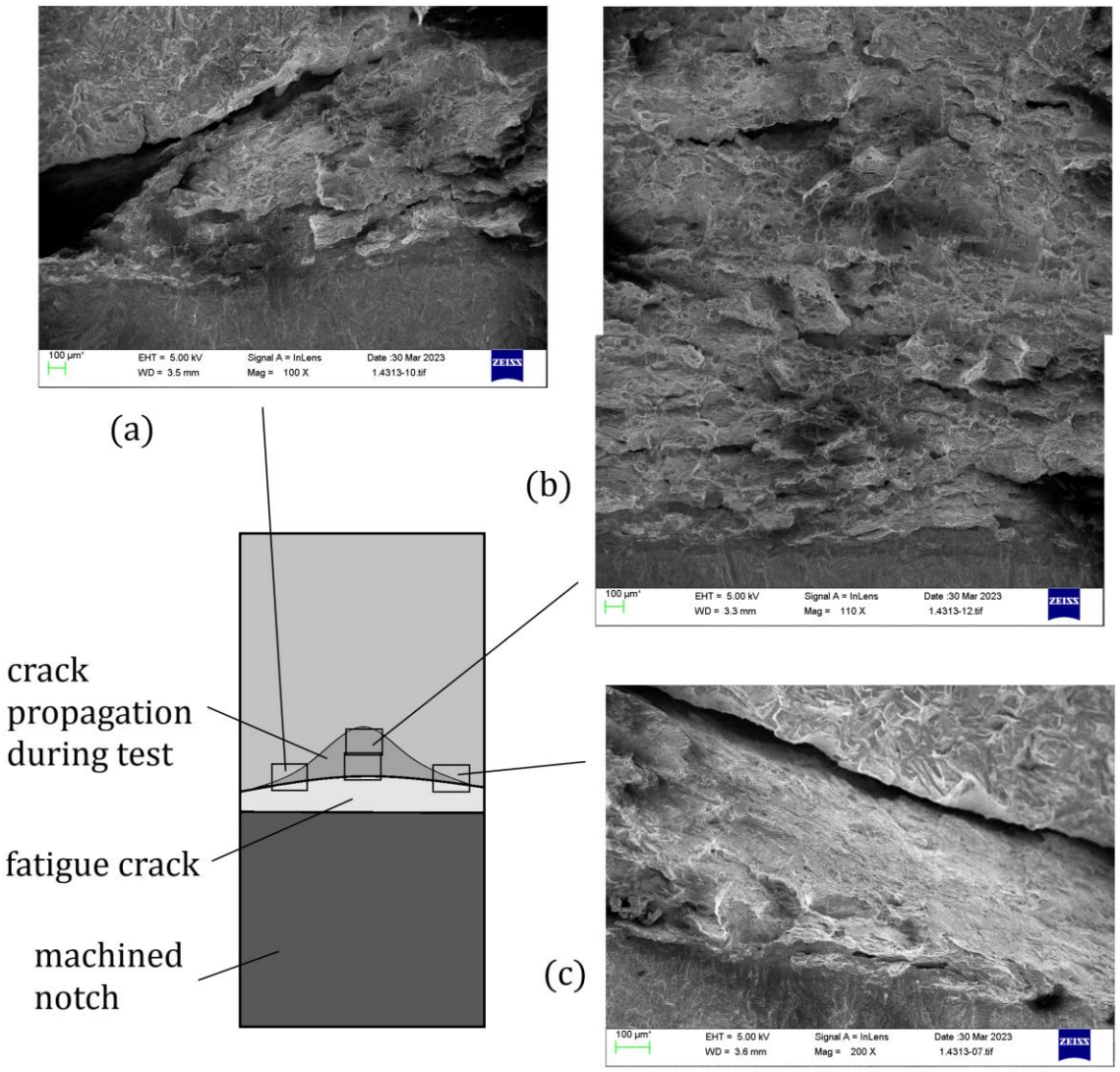

Figure 28. Fracture surface of the propagated crack in martensitic stainless steel sample.

4.2 Medium-carbon ultrahigh-strength steel

In the medium-carbon steel samples macroscopic fracture behavior was brittle and fracture occurred without significant stable crack growth. Load – displacement records for two of the samples showed significant pop-in behavior during the test. The load – displacement curves obtained from the fracture toughness tests conducted on the medium-carbon UHSS samples are combined in figure 29. Some scatter can be observed in the load – displacement records.

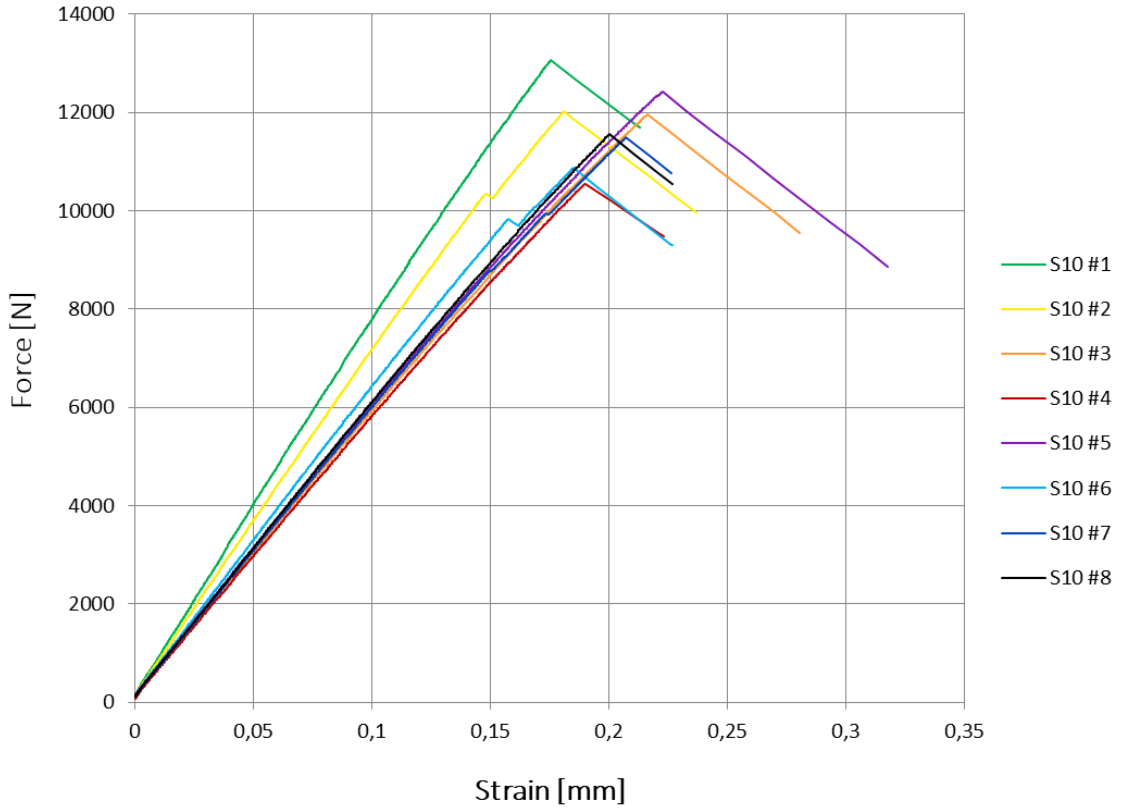

Figure 29. Load – displacement curves for the medium-carbon UHSS samples.

Since this material was known to undergo ductile-to-brittle transition, fracture toughness calculations were carried out according to ASTM E1921 which provides a method for determination of reference temperature T_0 for ferritic steels in the transition range. Force and corresponding displacement data as well as calculated values for Master Curve determination have been combined in table 11. Force values ending with asterisk * correspond to force values determined at the first significant pop-in for the sample, other force values correspond to obtained maximum force at fracture instability. The calculated values in table 11 have been determined according to standard ASTM E1921. In this data set, there were no censored data as none of the generated K_{Jc} values violated the censoring criteria. Calculations were conducted according to a single temperature analysis procedure as all test were carried out at 0 °C. Size of the data set was rather small, only eight samples. Hence the homogeneity screening procedure suggested for small data sets was applied.

Table 11. Calculated values for Master Curve.

Specimen	Test data: Force F_{max} [N]	Test data: CMOD V [mm]	Calculated values: K_{Jc} [MPa√m]	Calculated values: $K_{Jc(1T)}$ [MPa√m]	K_0 [MPa√m]	$K_{Jc(med)}$ [MPa√m]
TS10 #1	13056,2	0,18	85,5	72,0	71,5	66,9
TS10 #2	10334,6*	0,15	58,1	50,2		
TS10 #3	11946,4	0,22	92,6	77,5	T_0 [°C]	
TS10 #4	10544,3	0,19	82,4	69,5		
TS10 #5	12420,8	0,22	95,5	79,8		
TS10 #6	9823,7*	0,16	64,3	55,1	33,7	
TS10 #7	11489,4	0,21	89,9	75,4		
TS10 #8	11555,6	0,20	86,3	72,5		

Figure 30 represents the determined Master Curve with 95 % and 5 % tolerance bounds for the 1T specimens of the studied medium-carbon ultrahigh-strength steel. The figure also contains the size adjusted K_{Jc} data for each sample tested.

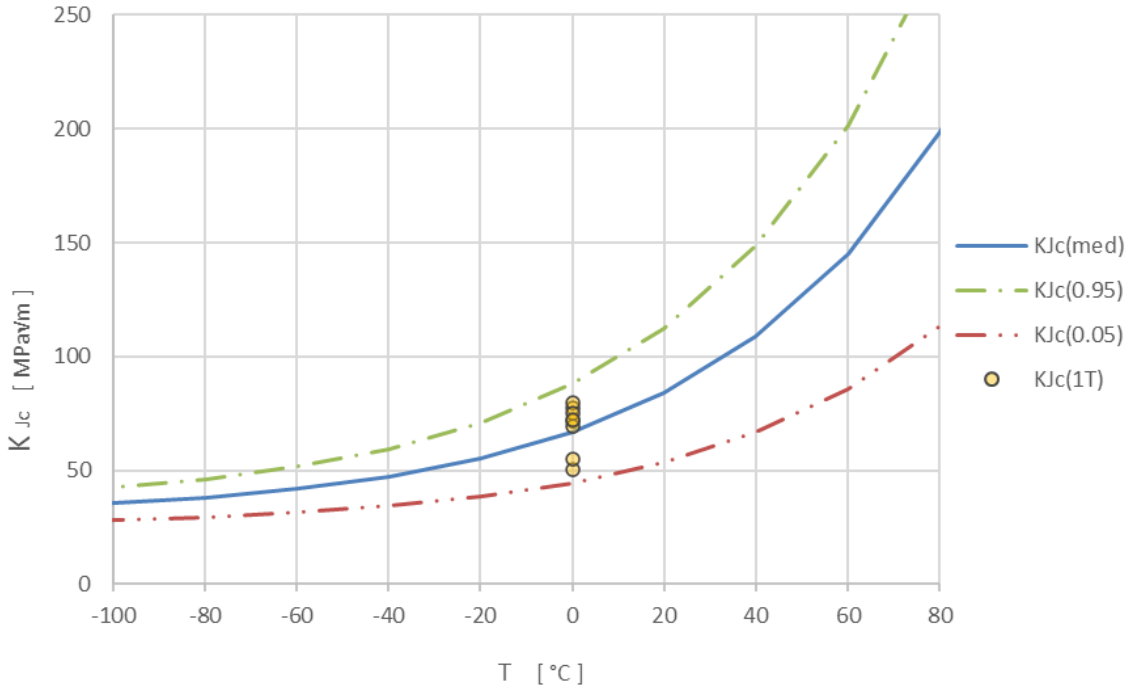

Figure 30. Master Curve for 1T specimens of medium-carbon UHSS.

CTOD calculations were carried out also for the medium-carbon steel samples. Again, CTOD was determined according to both ISO 12135 and ASTM E1820, see table 12. The measured fatigue precrack lengths did not meet the required 1.3 mm minimum length at any of the measuring points in sample #1, nor were they met, at either of the near-surface measuring points in sample #2, thus marked with asterisk (*). But again, the measured fatigue precrack lengths at all measuring points in all samples did fulfill the minimum crack length requirements stated in ASTM E1820. Also here, the CTOD values determined according to the ISO standard were calculated using both theoretical elastic compliance and experimental compliance. Again, values calculated with the theoretical elastic compliance yielded slightly larger estimates for CTOD. The CTOD values calculated according to ASTM were determined through the J-integral, without relevant crack growth corrections. However, since stable crack growth before fracture was practically nonexistent, the correction would not have made any perceivable difference.

Table 12. Combined test data, and crack-tip opening displacement values calculated according to standards ISO 12135 and ASTM E1820.

Fracture toughness	Test data			ISO 12135		ASTM 1820
				with theor. elastic compliance	with experim. compliance	with experim. compliance
Specimen	Force F_{max} [N]	CMOD V [mm]		CTOD δ [mm]	CTOD δ [mm]	CTOD δ [mm]
Medium-C	11396	0,19	Mean	0,021	0,014	0,013
			Median	0,023	0,015	0,014
			Standard deviation	0,005	0,004	0,003
TS10 #1 *	13056	0,18		0,022	0,015	0,014
TS10 #2 *	10335	0,15		0,015	0,009	0,009
TS10 #3	11946	0,22		0,026	0,019	0,016
TS10 #4	10544	0,19		0,018	0,014	0,013
TS10 #5	12421	0,22		0,028	0,020	0,017
TS10 #6	9824	0,16		0,015	0,010	0,010
TS10 #7	11489	0,21		0,024	0,018	0,015
TS10 #8	11556	0,20		0,024	0,016	0,014

Three medium-carbon steel samples were selected for fracture surface examinations, two of which exhibited pop-in behavior during the fracture test and one which did not. Fracture surface appearance obtained with FESEM for the studied medium-carbon steel can be seen in figures 31 – 35. Fracture surface examination revealed that fracture mechanisms during the fracture toughness test showed both brittle and ductile

characteristics in this steel. Fracture surface examination of the two samples, that exhibited pop-ins during fracture test, did not reveal any particular reason for the observed pop-in behavior.

Fracture surfaces of all studied medium-carbon UHSS samples showed similar features. In the central region of the samples, deep secondary cracks were found in front of the fatigue crack front, figures 31 and 32 (a) and (c), surrounded by regions of mostly ductile fracture, figures 31 and 32 (b), (d), and (e). These locations were considered as likely initiation sites for fracture. Secondary cracks with ductile fracture surfaces were also visible every here and there on the examined fracture surfaces, figure 33. Figure 33 (a) and (b), taken from samples #1 and #2, present the mostly brittle fracture surfaces with secondary cracks. Figure 33 (c) was taken at the edge of one of the secondary cracks found on sample #6. Here, the dark area at the right edge is the secondary crack, the light area in the middle is the upright fracture surface of the secondary crack garnished with ductile fracture features and the slightly darker area on the left side of the picture shows the fracture surface consisting of both brittle and ductile features.

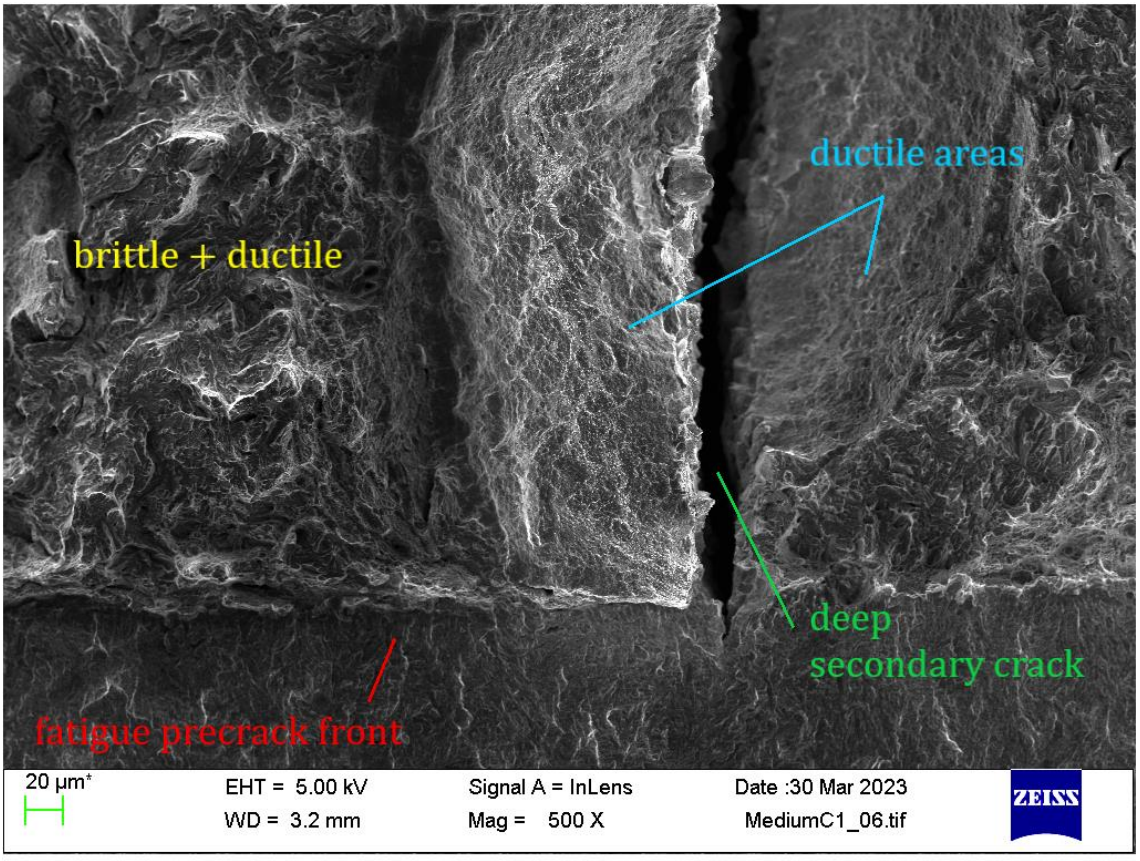

Figure 31. Overview of the fracture surface at vicinity of a deep secondary crack ahead of the fatigue precrack front in medium-carbon steel sample #1.

Medium-carbon steel,
sample #2

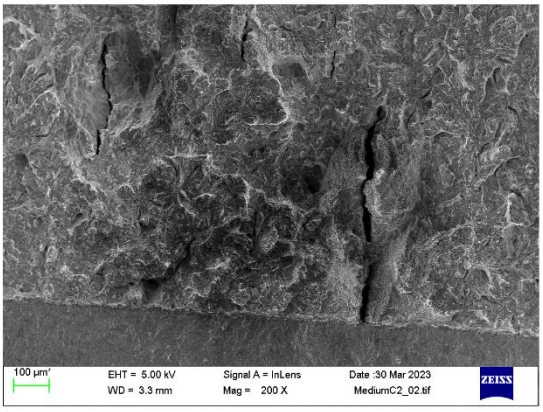

(a)

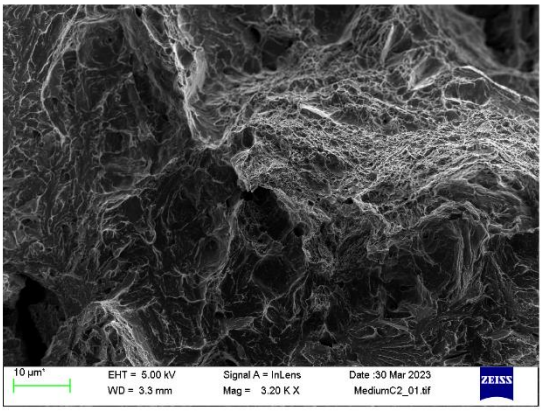

(b)

Medium-carbon steel,
sample #6

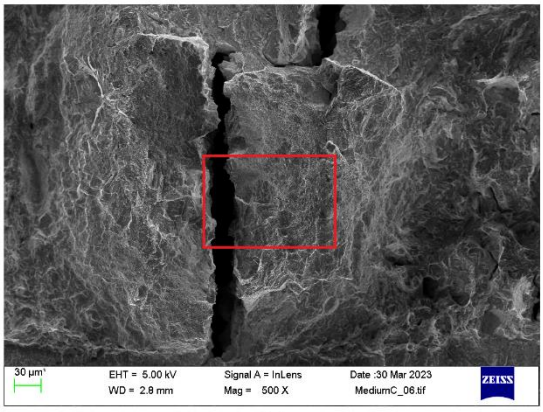

(c)

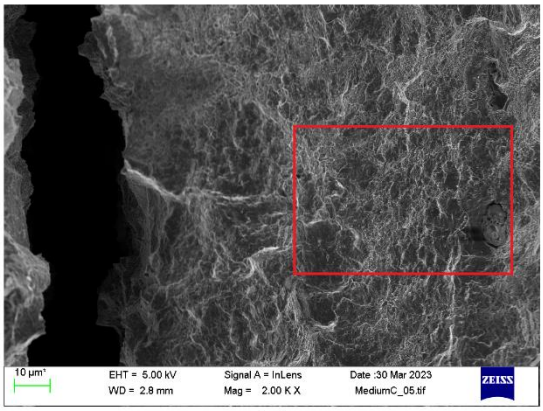

(d)

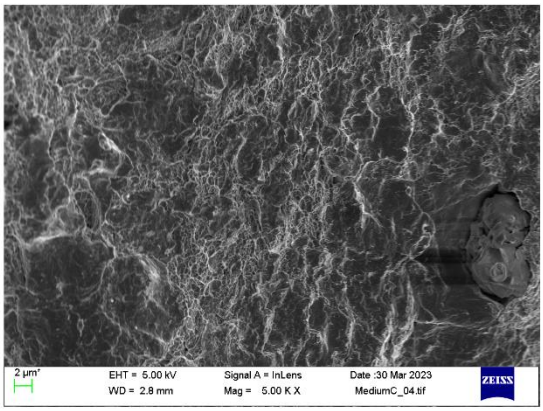

(e)

Figure 32. Deep secondary cracks found ahead of the fatigue crack front in medium-carbon steel: a) sample #2, b) close-up of the ductile area at near vicinity of the deep secondary crack at fatigue crack front shown in a), c) sample #6, d) close-up of the area highlighted in c), and e) close-up of the area highlighted in d), showing ductile dimples.

Medium-carbon steel,
sample #1

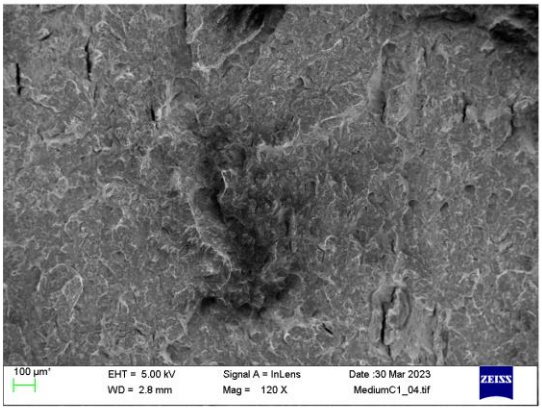

(a)

Medium-carbon steel,
sample #2

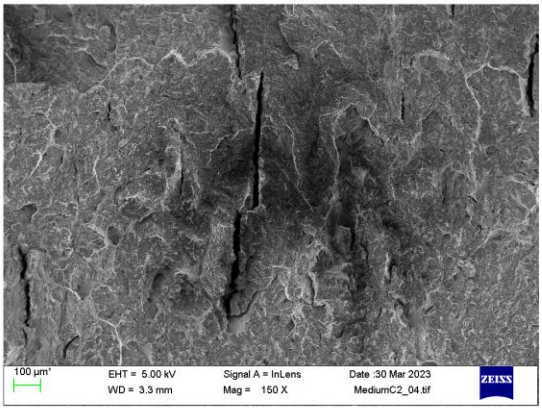

(b)

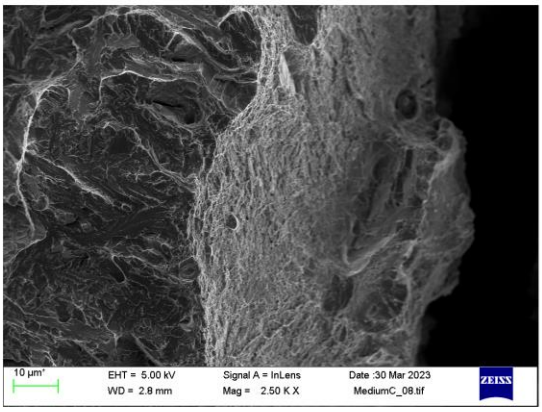

(c)

Figure 33. Overview of the mostly brittle fracture surfaces with ductile secondary cracks, taken a) at the central region of the fracture surface formed at fracture instability in sample #1, b) at the central region of the fracture surface in sample #2, and c) at an edge of a secondary crack found on sample #6.

Macroscopically fracture surface had a shiny, grainy appearance, characteristic of brittle fracture. Closer examinations revealed a fracture surface consisting of mostly brittle characteristics accompanied by ductile features. Ductile tearing ridges could be observed here and there, between which brittle cleavage facets dominated the fracture surface, figure 34.

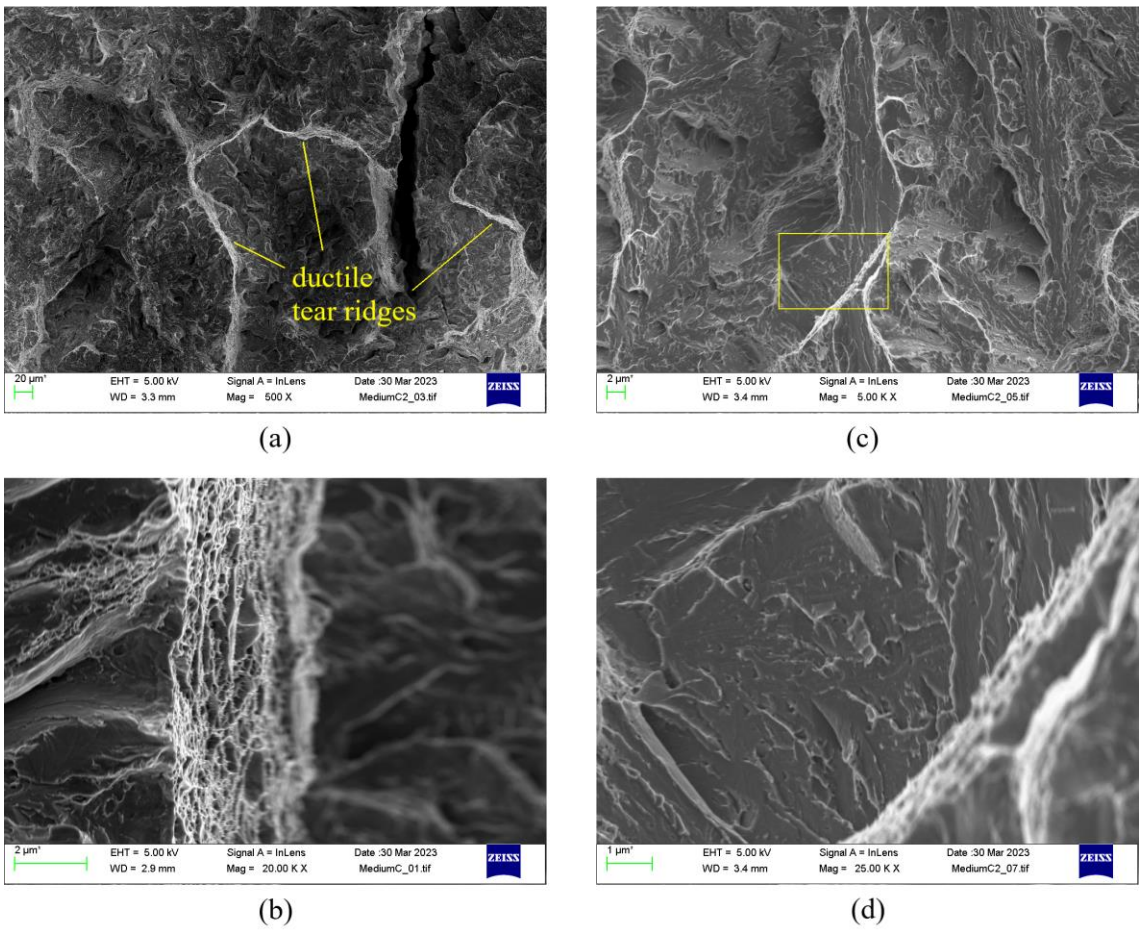

Figure 34. Brittle and ductile features on fracture surfaces of medium-carbon steel, a) mostly brittle surface with ductile tear ridges, b) closer view of a ductile tear ridge, c) closer view of the brittle fracture surface showing mostly cleavage facets, but also small ductile regions, and d) close-up of one of the facets in the highlighted area in c) showing ductile dimples on the facets.

The border between the fracture surface created at fracture instability during the test and the one formed during the final opening of the sample after test, proved very challenging to distinguish, since no heat tinting nor fatigue cycling after fracture tests were performed, making the deduction of the length of unstable crack extension at the end of the test very unreliable. However, it appeared that the surface created at the final opening of the samples, figure 35 (a), appeared somewhat less coarse and more even compared to the fracture surface created at fracture instability, figure 35 (b), although same fracture features were presents in both surfaces. Secondary cracks were more numerous and deeper at fracture surface created at fracture instability. Crack extension at instability, although not easily detectible, appeared to be rather even along the whole crack front.

The primary initiation sites of the macroscopically brittle failure could not be indisputably identified.

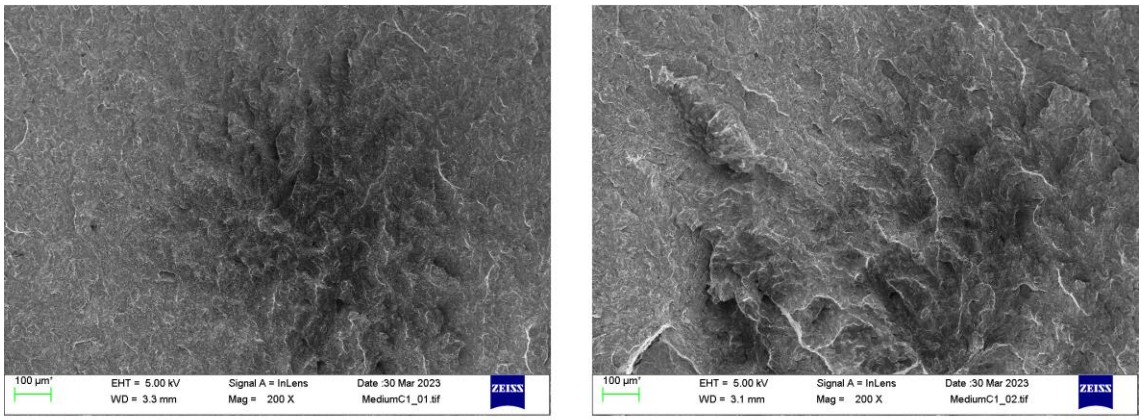

(a) (b)

Figure 35. Fracture surface a) formed at the final opening of the samples and b) formed at fracture instability during fracture test.

5 DISCUSSION

The chemical compositions and mechanical properties of the two studied ultrahigh-strength steels were quite different, and although both of these materials had a lath martensitic microstructure, they behaved very differently on fracture toughness tests conduct at 0 °C. The fracture behavior of the martensitic stainless steel was structurally very ductile, whereas the medium-carbon tool steel behaved structurally brittle in fracture tests. Fracture surface examinations with SEM confirmed that the fracture micromechanism in the martensitic stainless steel was ductile, as expected, whereas for the medium-carbon tool steel, although being structurally brittle, fracture seemed to have involved a mixture of both brittle and ductile micromechanisms, likely initiating with ductile micromechanism but propagating mainly by brittle mechanisms. This was well in line with what was discussed in section 2.1, being that the structural fracture behavior does not directly indicate the fracture micromechanism.

In the martensitic stainless steel samples fracture was found to have experienced tunneling. Although final physical crack lengths were not measured, it is likely that if they had been measured, some of the lengths would have violated the deviation requirements set in the standards. Although the standards do not insist the use of side grooves when determining point values for ductile materials, side-grooving is either insisted or highly recommended for R-curve determination. From this view, it might be appropriate to use side-grooving also for the determination of point values when testing very ductile materials, as a more even crack extension along the thickness would perhaps result in somewhat different load-displacement record and thus affect the values obtained by calculations.

Measurement of the initial crack length was identified in the literature as the most significant source for uncertainty. In this work it was as well found rather cumbersome and probably the most time consuming individual step during the whole process. In the future, ways to facilitate this step should be looked into.

Some of the fatigue precracks were found not to fulfill the minimum length requirements set in the ISO standard, although same prefatiguing specs were applied for all the samples belonging to the same set. Deviation in fatigue precrack lengths between specimens was not remarkably large in martensitic stainless steel specimens, while among the medium-

carbon tool steel specimens it was notable. In the future, fatigue precrack growth should be monitored more carefully and fatiguing be continued further as necessary.

It was also found, that distinguishing the boundary between the fracture surface created during the fracture test, and the surface formed when opening the samples after tests, was not practical with either the used laser microscope, where the depth resolution is not sufficient, or with SEM. Thus it would be advisable to perform either heat tinting or fatigue cycling on the samples after fracture tests, as suggested in the standards, if a_f is to be measured. That is at least the case with the two materials studied here.

CTOD calculated according to ISO 12135 utilizing theoretical elastic compliance yielded the highest values, i.e. the least conservative estimates, for fracture toughness. CTOD calculated according to ASTM E1820 in turn yielded the smallest values, providing the most conservative estimates of the lot. For the ductile martensitic stainless steel, the difference between CTOD values calculated with C_{theo} and C_{exp} according to the ISO standard was smaller than the difference between CTOD values calculated according to ISO and ASTM standards using C_{exp}. For the medium-carbon tool steel showing structurally brittle behavior, the difference between CTOD values calculated according to the ISO standard with different compliances was clearly larger than the difference between CTOD values calculated using C_{exp} between the two standards. For this steel, the difference between CTOD values calculated using C_{exp} between the two standards was about 8 % whereas for the ductile martensitic stainless steel it was about 20 %. Based on this, it seems, that the difference between the CTOD values calculated between the two standards using $C_{exp,}$ may increase with increasing ductile behavior. For 1.4313, the standard deviations of the differently calculated CTOD values were of the same order, about 12 – 12,5 %. For the tool steel, standard deviations were expectedly higher as brittle materials are known to show more scatter in the FT data, but also deviated more between the differently calculated CTODs. CTOD results calculated according to ASTM showed the smallest standard deviation, about 21 %, while the highest standard deviation was with the CTOD values calculated according to ISO using C_{exp}, about 29 %. For both materials CTOD calculated using the C_{theo} yielded the greatest, i.e. the least conservative values of FT. In light of this, it might be more appropriate to use the C_{exp} for calculations.

MC calculations for the studied tool steel suggest the possibility of cleavage to be present at normal operating temperatures, i.e. at room temperature.

All and all, fracture toughness determination process with all the different stages from specimen machining and preparation all the way to FT parameter determination truly is time consuming. From the viewpoint of productization it is essential to optimize the time used for the whole process and for each individual step. The entire procedure, starting from extracting and machining the samples, ending to the calculation, should be planned aforehand, and assessment is to be made throughout the procedure, in case anything unexpected arises that needs to be considered before continuing further. In each step, it is crucial to ensure all individual tasks are carried out with attentiveness, making sure all essential requirements are met before proceeding to the next stage. To ease and to speed up the calculations, use of spreadsheets is necessary.

It is important for the tester to be aware of the effects on fracture toughness arising from factors such as specimen geometry, temperature and loading rate. Such knowledge is useful for example when assessing which specimen geometry would be most suitable for the case at hand, which parameters would provide the most appropriate or useful data on fracture toughness for the case, or where lies the most critical sources for uncertainty. Same factors, such as testing rate as a function of stress intensity factor or actual success of prefatiguing and initial crack size, are truly known only after test and/or final opening of the samples, which inflicts some uncertainty for testing. Since the fracture behavior of materials is affected by so many different factors, the tester should be familiar with the backgrounds of fracture mechanics. An understanding of material engineering and metallurgy is also beneficial, especially for testing of welds. Comprehension of fracture micromechanisms and identifying different mechanisms and mechanism typical features on fracture surfaces, is valuable. Although the standard procedures in principle enables testing of unknown materials, choosing the right specs for testing may require an educated guess, and thus, in practice, requires practice, and knowledge of the FM theory as well as materials is beneficial for the tester. It is also useful to distinguish the differences, as well as the connections, between different fracture toughness parameters.

Testing standards set the limits within which the results are likely to be representative of the materials fracture toughness, but the grounds for the given limits are not much clarified. The set limits provide primary certainty, but knowledge of the FMs backgrounds brings additional reassurance for the interpretation of the test data and assessing the soundness of the results, as well as aids the selection of most appropriate fracture toughness parameters.

6 CONCLUSIONS

For purposes of productizing the fracture toughness testing method, aspects of fracture mechanical testing were examined. Theoretical background of fracture mechanics and fracture toughness testing was reviewed in this work, and fracture toughness of two martensitic ultrahigh-strength steels at low temperature was investigated. Initially the plan was to perform fracture toughness testing just for the martensitic stainless steel at several low temperatures, but the plan had to be altered and the other material was introduced as the delivery of the stainless steel samples was delayed remarkably. In the end, the long waited samples did arrive, but as the number of specimens at that point was limited and results of the fracture toughness tests for proficiency test had to be transmitted on rather a tight schedule, the initial idea of multiple temperature testing was abandoned to save time. Based on all examinations the following conclusions were made:

- The studied martensitic stainless steel showed ductile behavior in the fracture toughness tests conducted at 0 °C. Micromechanisms of fracture was as well found to be ductile, as could be expected.
- For the martensitic stainless steel, fracture toughness at 0 °C was determined in terms of CTOD. If these results were to be used in the future, e.g. for failure probability assessment analysis, orientation of the samples used should be determined. Values calculated using C_{exp} should be preferred instead of values calculated using C_{theo}.
- The medium-carbon tool steel behaved structurally brittle during the fracture tests conducted at 0 °C. It was found that in this steel fracture occurred through both brittle and ductile micromechanisms at the investigated temperature.
- For the medium-carbon tool steel fracture toughness was determined in terms of both CTOD and MC. Since some scatter appeared among the test results, MC likely provides a more suitable parameter to characterize fracture toughness in this material.
- MC calculations for the studied tool steel suggest the possibility of cleavage to be present at normal operating temperatures, i.e. at room temperature.
- The addressed testing standards ISO 12135 and ASTM E1820 had many common features and differed from one another mainly on the calculation formulas for the CTOD parameter.

- Fracture toughness testing in all is a time consuming process that involves multiple different stages, the execution of each of which requires attentiveness. From the productization viewpoint, ways to optimize the time used in the process should be looked into.
- It is advisable to use spreadsheets to aid and speed up calculations.
- In the future, fatigue precrack growth should be monitored more carefully and fatiguing be continued further as necessary.
- Also in the future, heat tinting or fatiguing should be applied after fracture test to aid measurement of final physical crack length.
- When testing ductile materials, side-grooving is advisable to prevent excess tunneling.
- Experimentally determined compliance values should be preferred for parameter calculations instead of theoretical compliance values.
- It is beneficial for the tester to be familiar with the theory of fracture mechanics in order to distinguish the differences and connections between different FT characterizing parameters and to recognize the limits in which each parameter can be considered as a valid representative for fracture toughness. It is also important to understand the effects of different factors (such as temperature, specimen geometry and loading rate) affecting fracture toughness.

Based on the standards and theory addressed in this work, working instructions for fracture toughness testing as well as spreadsheets for parameter calculations, and for determination of uncertainties of testing for the parameters, were prepared for productization of the test method, but on grounds of company confidentiality policy are not included here. In the future, a procedure based on the working instructions composed along this work will be used for fracture toughness determination at DEKRA.

REFERENCES

Ahlblom, B., Hansson, P., & Narström, T., 2007. Martensitic Structural Steels for Increased Strength and Wear Resistance [online document]. Materials Science Forum, vols. 539-543, pp. 4515 – 4520. Trans Tech Publications, Switzerland. Available: https://doi.org/10.4028/www.scientific.net/MSF.539-543.4515 [Accessed 26.09.2022]

ArcelorMittal, 2023. ArcelorMittal, Toughness and resistance to brittle fracture [online document]. Luxembourg: ArcelorMittal Europe Communications. Available: https://constructalia.arcelormittal.com/en/sica-steel-academy/properties-of-steel/toughness-and-resistance-to-brittle-fracture [Accessed 20.03.2023].

ASM Handbook committee, 1987. Metals Handbook – Volume 12 Fractography, Nineth Edition. Metals Park, Ohio: ASM International, 517 p. ISBN: 0-87170-007-7

ASTM E1820, 2022. Standard Test Method for Measurement of Fracture Toughness. West Conshohocken, US-PA: ASTM International, 15 + 50 pp.

ASTM E1921, 2022. Standard Test Method for Determination of Reference Temperature, T0, for Ferritic Steels in the Transition Range. West Conshohocken, US-PA: ASTM International, 21 + 19 pp.

Baser, T., Leinenbach, C., and Schindler, H.-J., 2010. Fracture Behaviour of Brazed Soft Martensitic Stainless Steel Joints under Cyclic Loading [online document]. Materials Science Forum Vols. 636-637, pp. 1490-1495 Trans Tech Publications Ldt, Switzerland. Available: https://doi.org/10.4028/www.scientific.net/MSF.636-637.1490 [Accessed 05.10.2022]

Brück, S., Schippl, V., Schwarz, M., Christ, H.-J., Fritzen, C.-P. & Weihe, S., 2018. Hydrogen Embrittlement Mechanism in Fatigue Behavior of Austenitic and Martensitic Stainless Steels [online document]. Metals 2018 Vol. 8, Iss. 5. Available: https://www.researchgate.net/publication/325086541_Hydrogen_Embrittlement_Mechanism_in_Fatigue_Behavior_of_Austenitic_and_Martensitic_Stainless_Steels [Accessed 17.10.2022]

Castelluccio, G. M., & McDowell, D. L., 2016. Microstructure-sensitive small fatigue crack growth assessment: Effect of strain ratio, multiaxial strain state, and geometric discontinuities [online document]. International Journal of Fatigue, 82, pp. 521–529. Available: https://doi.org/10.1016/j.ijfatigue.2015.09.007 [Accessed 29.02.2022]

Chen, J., Verreman, Y. & Lanteigne, J., 2013. On fracture toughness J_{IC} testing of martensitic stainless steels [online document]. 13th International Conference on Fracture, 2013, pp. 16 – 21, Beijing, China. Available: https://scholar.google.fi/scholar?cluster=2896338553812198135&hl=fi&as_sdt=0,5&as_vis=1 [Accessed 17.10.2022]

Cho, L., P.E. Bradley, P.E., Lauria, D.S., Martin, M.L., Connolly, M.J., Benzing, J.T., Seo, E.J., Findley, K.O., Speer, J.G. & Slifka, A.J., 2021. Characteristics and mechanisms of hydrogen-induced quasi-cleavage fracture of lath martensitic steel [online document]. Acta Materialia, Vol. 206, 116635, ISSN 1359-6454. Elsevier Ltd. Available: https://doi.org/10.1016/j.actamat.2021.116635. [Accessed 24.01.2023]

Deschênes, P.-A., Lanteigne, J., Verreman, Y., Paquet, D., Lévesque, J.-B. & Brochu, M., 2017. A new experimental method to study the influence of welding residual stresses on fatigue crack propagation [online document]. International Journal of Fatigue, Vol. 100, Part 1,pp. 444 – 452, ISSN 0142-1123. Available: https://doi.org/10.1016/j.ijfatigue.2017.01.031. [Accessed 17.10.2022]

Fan, Y. H., Zhang, B., Yi, H. L., Hao, G. S., Sun, Y. Y., Wang, J. Q., Han, E.-H. & Ke, W., 2017. The role of reversed austenite in hydrogen embrittlement fracture of S41500 martensitic stainless steel [online document]. Acta Materialia Vol. 139, pp. 188 – 195. Available: https://doi.org/10.1016/j.actamat.2017.08.011 [Accessed 17.10.2022]

Foroozmehr, F., Verreman, Y., Chen, J., Thibault, D. & Bocher, P., 2017. Effect of inclusions on fracture behavior of cast and wrought 13% Cr-4% Ni martensitic stainless steels [online document]. Engineering Fracture Mechanics Vol. 175, pp. 262 – 278 Available: https://doi.org/10.1016/j.engfracmech.2017.02.002 [Accessed 17.10.2022]

Foroozmehr, F. & Bocher, P., 2021. An investigation on fracture toughness of heat-affected zone in the welded joints of 13%Cr-4%Ni martensitic stainless steels [online document]. Fatigue & Fracture of Engineering Materials & Structures, Vol. 44, Iss. 12 pp. 3416 – 3430. Available: https://doi.org/10.1111/ffe.13569 [Accessed 17.10.2022]

Ghafoori-Ahangar, R. & Verreman, Y., 2019. Fatigue behavior of load-carrying cruciform joints with partial penetration fillet welds under three-point bending [online document]. Engineering Fracture Mechanics Vol. 215 pp. 211 – 223. Elsevier Ltd. Available: https://doi.org/10.1016/j.engfracmech.2019.05.015 [Accessed 17.10.2022]

Grewal, H.S., Arora, H.S., Agrawal, A, Singh, H. & Mukherjee, S., 2013. Slurry Erosion of Thermal Spray Coatings: Effect of Sand Concentration [online document]. Procedia Engineering, Vol. 68, pp. 484 - 490, ISSN 1877-7058. Available: https://doi.org/10.1016/j.proeng.2013.12.210. [Accessed 17.10.2022]

Hannula, S.-P., Haimi, E., and Lindroos, V., 2020a. Uudistettu Miekk-ojan Metallioppi, Osa I. Helsinki: Teknologiateollisuus ry, 248 p. ISBN 978-952-238-225-2

Hannula, S.-P., Haimi, E., and Lindroos, V., 2020b. Uudistettu Miekk-ojan Metallioppi, Osa II. Helsinki: Teknologiateollisuus ry, 272 p. ISBN 978-952-238-244-3

Hansson, P. & Melin, S., 2008. Simulation of simplified zigzag crack paths emerging during fatigue crack growth [online document]. Engineering Fracture Mechanics, Vol. 75, Iss. 6, pp. 1400 – 1411, ISSN 0013-7944. Elsevier Ltd. Available: https://doi.org/10.1016/j.engfracmech.20 07.07.002 [Accessed 20.10.2022]

Hassanipour, M., Verreman, Y. & Lanteigne, J., 2017. Fatigue threshold at high stress ratio under periodic underloads in turbine runner steels [online document]. International Journal of Fatigue, Vol. 103, pp. 264 – 271, ISSN 0142-1123. Available: https://doi.org/10.1016/j.ijfatigue.2017.06.009. [Accessed 17.10.2022]

Hassanipour, M., Verreman, Y., Lanteigne, J. & Chen, J.Q., 2016. Effect of Periodic Underloads on Fatigue Crack Growth in Three Steels Used in Hydraulic Turbine Runners [online document]. International Journal of Fatigue, Vol. 85, pp. 40 – 48. Available: https://www.researchgate.net/publication/285361628_Effect_of_Periodic_Underloads_on_Fatigue_Crack_Growth_in_Three_Steels_Used_in_Hydraulic_Turbine_Runners [Accessed 17.10.2022]

Heidarpour, A., Tofts, N.S., Korayem, A.H., Zhao, X.-L., & Hutchinson, C.R., 2014. Mechanical properties of very high strength steel at elevated temperatures [online document]. Fire Safety Journal, Vol. 64, pp. 27 – 35, Elsevier B.V. Available: https://doi.org/10.1016/j.firesaf.2014.01.006 [Accessed 03.10.2022]

Hernandez, S., Hardell, J., Winkelmann, H., Ripoll, M. R., & Prakash, B., 2015. Influence of temperature on abrasive wear of boron steel and hot forming tool steels [online document]. Wear, vol. 338-339, pp. 27–35. Available: https://www.sciencedirect.com/science/article/pii/S0043164815003178?casa_token=2YX5zwvfSMEAAAAA:rMAJLTRmMUsbCkL5ubhSGEavKjK9nsrK4Q2FajcS7caMUoymt2bzTOt8zSc4cmniqagqKu0qUA [Accessed 05.10.2022]

Hutchinson, J. W., 1968. Singular behaviour at the end of a tensile crack in a hardening material [online document]. Journal of the Mechanics and Physics of solids, Vol. 16, Issue 1, pp. 13 – 31. Available: https://doi.org/10.1016/0022-5096(68)90014-8 [Accessed 11.01.2022]

ISO, Standards [online] Geneva: ISO – International Organization for Standardization, 2021. Available: https://www.iso.org/search.html?q=12135 [Accessed 28.09.2022]

ISO 12135, 2016. Metallic materials — Unified method of test for the determination of quasistatic fracture toughness. Second edition. ISO: 59 + 45 pp.

ISO 12135, 2021. Metallic materials — Unified method of test for the determination of quasistatic fracture toughness. Third edition. ISO: 65 + 43 pp.

Kanvinde, A., 2016. Predicting Fracture in Civil Engineering Steel Structures: State of the Art [online document]. Journal of Structural Engineering, Vol. 143, 2017. Available: https://doi.org/10.1061/(ASCE)ST.1943-541X.0001704 [Accessed 28.07.2022]

Kawabata, T., Tagawa, T., Sakimoto, T., Kayamori, Y., Ohata, M., Yamashita, Y., Tamura, E., Yoshinari, H., Aihara, S., Minami, F., Mimura, H. & Hagihara, Y., 2016. Proposal for a new CTOD calculation formula [online document]. Engineering Fracture Mechanics, vol. 159, pp. 16 – 34. Elsevier Ltd. Available: https://doi.org/10.1016/j.engfracmech.2016.03.019 [Accessed 12.10.2022]

Khor, W., Moore, P., Pisarski, H. & Brown, C., 2017. Comparison of methods to determine CTOD for SENB specimens in different strain hardening steels [online document]. Fatigue & Fracture of Engineering Materials & Structures, Vol. 41, pp. 551 – 564. Wiley Publishing Ltd. Available: DOI: 10.1111/ffe.12718. [Accessed 22.10.2022]

Kirk, M.T. & Dodds, R.H., 1993. J and CTOD estimation equations for shallow cracks in single edge notched bend specimens [online document]. ILLINOIS UNIV AT URBANA DEPT OF CIVIL ENGINEERING. Available: https://apps.dtic.mil/sti/citations/ADA261679 [Accessed 22.10.2022]

Koster, M., Kenel, C., Stutz, A., Lee, W.J., Lis, A., Affolter, C., & Leinenbach, C., 2013. Fatigue and cyclic deformation behavior of brazed steel joints [online document]. Materials Science & Engineering: A, Vol. 581, pp. 90 – 97, Elsevier B.V. Available: http://doi.org/10.1016/j.msea.2013.05.083 [Accessed 26.08.2022]

Krum, S., Pešlová, F., Horník, J., & Puchnin, M., 2017. Structural Changes of Hot Work Tool Steel due to Heat load [online document]. Solid State Phenomena, vol. 270, pp. 34 – 38 Available: https://doi.org/10.4028/www.scientific.net/SSP.270.34 [Accessed 29.09.2022]

Leinenbach, C., Schindler, H.-J., Baser, T., Rüttimann, N. & Wegener, K., 2010. Quasistatic fracture behaviour and defect assessment of brazed soft martensitic stainless steel joint [online document]. Engineering failure analysis, Vol. 17 Iss. 3, pp. 672 – 682. Available: https://doi.org/10.1016/j.engfailanal.2009.05.002 [Accessed 05.10.2022]

Liaw, P. K. (chairperson), Impact Toughness Testing and Fracture Mechanics, 2000. In: Kuhn, H. & Medlin (edit.), D.: ASM Handbook Volume 8 – Mechanical Testing and Evaluation, 2000. Ohio, US: ASM International, 998 p. ISBN: 0-87170-389-0

Lipiäinen, K., Ahola, A., Skriko, T. & Björk, T., 2021. Fatigue strength characterization of high and ultra-high-strength steel cut edges [online document]. Engineering structures Vol. 228. Available: https://doi.org/10.1016/j.engstruct.2020.111544 [Accessed 24.08.2022]

Lynch, S., 2019. A review of underlying reasons for intergranular cracking for a variety of failure modes and materials and examples of case histories [online document]. Engineering Failure Analysis Vol. 100 pp. 329 – 350. Elsevier Ltd. Available: https://doi.org/10.1016/j.engfailanal.2019.02.027 [Accessed 20.10.2022]

Mackenzie, A.C., Hancock, J.W. & Brown, D.K., 1977. On the influence of state of stress on ductile failure initiation in high strength steels [online document]. Engineering Fracture Mechanics,Vol. 9, Iss. 1, pp. 167 – 188, ISSN 0013-7944, Available: https://doi.org/10.1016/0013-7944(77)90062-5. [Accessed 20.10.2022]

MacKenzie, S., 2008. Overview of the Mechanism of Failure in Heat Treated Steel Components [Online document]. Ohio: ASM International. Failure Analysis of Heat Treated Steel Components pp. 43 – 86. ISBN: 978-1-62708-284-6 Available: https://doi.org/10.31399/asm.tb.fahtsc.t51130043 [Accessed 17.10.2022]

Mandal, G., Dey, I., Mukherjee, S., & Ghosh, S.K., 2022. Phase transformation and mechanical properties of ultrahigh strength steels under continuous cooling conditions [online document]. Journal of Materials Research and Technology vol. 19, 2022, pp. 628 – 642. Elsevier B.V. Available: https://www.sciencedirect.com/science/article/pii/S2238785422006949 [Accessed 06.10.2022]

Mandolfino, C., Lertora, E., Davini, L., & Gamboro, C., 2013. Investigation on gas metal arc weldability of a high strength tool steel [online document]. Materials & Design, Vol. 56, 2014, pp. 345 – 352. ISSN 0261-3069. Elsevier Ltd. Available: https://doi.org/10.1016/j.matdes.2013.11.042 [Accessed 23.09.2022]

Martin, M.L., Fenske, J.A., Liu, G.S., Sofronis, P. & Robertson I.M., 2010. On the formation and nature of quasi-cleavage fracture surfaces in hydrogen embrittled steels [online document]. Acta Materialia Vol. 59, pp. 1601 – 1606, Elsevier Ltd. Available: https://doi.org/10.1016/j.actamat.2010.11.024 [Accessed 22.11.2022]

Melo, G. F., Bose Filho, W. W., Alvarenga, R. F. S., Paes, M. T. P., Ferreira, D. C. F., & Franco, S.D., 2019. Structural Integrity of HSLA Steels under Hydrogen Embrittlement Condition. [online document] Brazil: Offshore Technology Conference, 2019. Available: https://doi.org/10.4043/29962-MS [Accessed 05.10.2022]

Neimitz, A., Dzioba, I., & Pala, T., 2014. Master Curve of High-Strength Ferritic Steel S960-QC [online]. Key Engineering Materials, vol. 598, pp. 178–183. Available: https://doi.org/10.4028/www.scientific.net/KEM.598.178 [Accessed 07.10.2022]

Newman Jr, J.C., James, M.A., & Zerbst, U., 2002. A review of the CTOA/CTOD fracture criterion [online document]. Engineering Fracture Mechanics 70 (2003) pp. 371 – 385, Pergamon. Available: https://doi.org/10.1016/S0013-7944(02)00125-X [Accessed 29.02.2022]

Nowacki, J., Sajek, A., & Matkowski, P., 2016. The influence of welding heat input on the microstructure of joints of S1100QL steel in one-pass welding [online document]. Archives of Civil and Mechanical Engineering, vol. 16, 2016, pp. 777 – 783. Elsevier Sp. Available: https://doi.org/10.1016/j.acme.2016.05.001 [Accessed 30.09.2022]

Ozgowicz, W., & Kalinowska-Ozgowicz, E., 2008. Investigations on the impact strength of constructional high-strength Weldox steel at lowered temperature [online document]. International Scientific Journal, vol. 32, 2008, pp. 89 – 94., World Academy of Materials and Manufacturing Engineering. Available: http://delibra.bg.polsl.pl/Content/28698/BCPS_32400_-_Investigations-on-th_0000.pdf [Accessed 26.09.2022]

Paucar Casas, W., Henke, S. & Novicki, N., 2009. Fracture toughness of CA6NM alloy, quenched and tempered, and of its welded joint without PWHT [online document]. Welding International Vol. 23, pp. 166 – 172. Available: DOI: 10.1080/09507110802543344 [Accessed 17.10.2022]

Pijpers, R.J.M., Kolstein, M.H., Romeijn, A., & Bijlaard, F.S.K., 2007. Fatigue Experiments on Very High Strength Steel Base Material and Transverse Butt Welds [online document]. Advanced Steel Construction Vol. 5, No. 1 (2009), pp. 14 – 32. Available: http://www.ascjournal.com/down/vol5no1/vol5no1_3.pdf [Accessed 26.08.2022]

Presno-Vélez, A., Bernardo-Sánchez, A., Menéndez-Fernández, M., & Fernández-Muñiz, Z., 2019. Multivariate Analysis to Relate CTOD Values with Material Properties in Steel Welded Joints for the Offshore Wind Power Industry [online document]. Energies 12 (20), MDPI. Available: https://www.mdpi.com/1996-1073/12/20/4001 [Accessed 29.09.2022]

Suresh, S., 1991. Fatigue of materials. Second edition. Cambridge : Cambridge University Press, 1998. 679 p. ISBN-13 978-0-521-57046-6

Ribeiro, M.B.A., Souza, A.J., & Amorim, H.J., 2021. Investigation of Surface Roughness Generated by End Milling of Toolox 44 [online document]. Available: https://www.researchgate.net/publication/357073873_INVESTIGATION_OF_SURFACE_ROUGHNESS_GENERATED_BY_END_MILLING_OF_TOOLOX_44_R [Accessed 05.10.2022]

Rice, J. R., Rosengren, G. F., 1968. Plane Strain Deformation near a Crack Tip in a Power-Law Hardening Material [online document]. Journal of the Mechanics and Physics of solids, Vol. 16, pp. 1 – 12. Available: https://www.researchgate.net/publication/281009672_Plane_strain_deformation_near_a_crack_tip [Accessed 11.01.2023]

Roa, C. V., Valdes, J. A., Larrahondo, F., Rodríguez, S. A., & Coronado, J. J., 2021. Comparison of the Resistance to Cavitation Erosion and Slurry Erosion of Four Kinds of Surface Modification on 13-4 Ca6NM Hydro-Machinery Steel [online document]. Journal of Materials Engineering and Performance, Vol. 30(10), pp. 7195 – 7212. Available: https://link.springer.com/article/10.1007/s11665-021-05908-9 [Accessed 17.10.2022]

Sarafan, S., Wanjara, P., Gholipour, J., Champliaud, H. & Mathieu, L., 2017. Mechanical properties of electron beam welds in heavy-section UNS S41500 martensitic stainless steel [online document]. The International Journal of Advanced Manufacturing Technology, Vol. 91, pp. 4141 – 4150. Available: DOI: 10.1007/s00170-017-0099-2 [Accessed 17.10.2022]

Sarafan, S., Wanjara, P., Lévesque, J.-B., Gholipour, J., Champliaud, H. & Mathieu, L., 2020. Through-Thickness Residual Stresses, Microstructure, and Mechanical Properties of Electron Beam-Welded CA6NM Martensitic Stainless Steel after Postweld Heat Treatment [online document]. Advances in Materials Science and Engineering, vol. 2020, Article ID 7194214, 16 pages, 2020. Available: https://doi.org/10.1155/2020/7194214 [Accessed 17.10.2022]

Schindler, H.-J., Leinenbach, C., and Baser, T., 2009. Cyclic Fracture Behaviour of Brazed Martensitic Stainless Steel Joints [online document]. Conference Paper: 12th International Conference on Fracture (ICF12) Ottowa, Canada. Available: https://www.dora.lib4ri.ch/empa/islandora/object/empa%3A8785/datastream/PDF/Schindler-2009-Cyclic_fracture_behaviour_of_brazed-%28published_version%29.pdf [Accessed 05.10.2022]

Schneider, J., Kienzler, A., Deuchert, M., Schulze, V., Kotschenreuther, J., Zum Gahr, K.-H., Löhe, D., & Fleischer, J., 2008. Mechanical structuring, surface treatment and tribological characterization of steel mould inserts for micro powder injection moulding [online document]. Microsystem Technologies 14, 2008, pp. 1797 – 1803. Springer Nature Switzerland AG. Available: https://doi.org/10.1007/s00542-008-0620-5 [Accessed 05.10.2022]

Schneider, J., Kienzler, A., & Schulze, V., 2011. Influence of surface condition on wear behavior of μPIM mould inserts made of tool steel and cemented carbide [online document]. Microsystem Technologies 17, 2011, pp. 273 – 280. Springer-Verlag. Available: https://doi.org/10.1007/s00542-011-1238-6 [Accessed 05.10.2022]

SFS-EN ISO 15653, 2018. Metallic materials. Method of test for the determination of quasistatic fracture toughness of welds. Second edition. Finnish Standards Association SFS: 34 + 18 pp.

Shih, C.F., 1981. Relationship between the J-integral and the crack opening displacement for stationary and extending cracks [online document]. Journal of the Mechanics and Physics of solids, Vol. 29, No.4, pp. 305 – 326. Available: https://doi.org/10.1016/0022-5096(81)90003-X [Accessed 11.01.2023]

Thibault, D., Bocher, P., Thomas, M., Lanteigne, J., Hovington, P. & Robichaud, P., 2011. Reformed austenite transformation during fatigue crack propagation of 13%Cr-4%Ni stainless steel [online document]. Materials Science & Engineering Vol. 528 pp. 6519 – 6526. Available: https://doi.org/10.1016/j.msea.2011.04.089 [Accessed 17.10.2022]

Tagawa, T., Kawabata, T., Sakimoto, T., Kayamori, Y., Ohata, M., Yamashita, Y., Tamura, E., Yoshinari, H., Aihara, S., Minami, F., Mimura, H. & Hagihara, Y., 2014. Experimental measurements of deformed crack tips in different yield-to-tensile ratio steels [online document]. Engineering Fracture Mechanics, Vol. 128, pp. 157 – 170. Elsevier Ltd. Available: https://doi.org/10.1016/j.engfracmech.2014.07.012 [Accessed 22.10.2022]

Tagawa, T., Kayamori, Y., Ohata, M., Handa, T., Kawabata, T., Yamashita, Y., Tsutsumi, K., Yoshinari, H., Aihara, S. & Hagihara, Y., 2010. Comparison of CTOD standards: BS 7448-Part 1 and revised ASTM E1290 [online document]. Engineering Fracture Mechanics, Vol. 77, pp. 327 – 336. Elsevier Ltd. Available: https://doi.org/10.1016/j.engfracmech.2009.02.009 [Accessed 22.10.2022]

Thibault, D., Bocher, P., Thomas, M., Gharghouri, M. & Côté, M., 2010. Residual stress characterization in low transformation temperature 13%Cr-4%Ni stainless steel weld by neutron diffraction and the countour method [online document]. Materials Science & Engineering: A, Vol. 527 pp. 6205 – 6210. Available: https://doi.org/10.1016/j.msea.2010.06.035 [Accessed 17.10.2022]

Thibault, D., Gagnon, M. & Godin, S., 2014. Bridging the gap between metallurgy and fatigue reliability of hydraulic turbine runners [online document]. IOP Publishing, IOP Conf. Series: Earth and Environmental Science 22. Available: doi:10.1088/1755-1315/22/1/012019 [Accessed 17.10.2022]

Tomerlin, D., Kozak, D., Damjanović, D., & Katinić, M., 2022. Structural life analysis method applied to hydraulic press welded frame construction [online document]. Welding in the World, vol. 66, 2022. International Institute of Welding. Available: https://doi.org/10.1007/s40194-022-01375-5 [Accessed 06.10.2022]

Trondl, A. & Sun, D.-Z., 2015. Modelling of Strain-Rate Dependence of Deformation and Damage Behavior of HSS- and UHSS at Different Loading States [online document]. Germany, Würzberg: 10th European LS-DYNA Conference 2015. DYNAmore GmbH. Available: https://www.dynalook.com/conferences/10th-european-ls-dyna-conference/2%20Crash%20I%20-%20Failure/03-Trondl-FraunhoferIWM-P.pdf [Accessed 20.10.2022]

Van Stone, R.H., Cox, T.B., Low, J.R., Jr., & Psioda, P.A., 1985. Microstructural Aspects of Fracture by Dimpled Rupture [online document]. International Metals Reviews, 30 (1), pp. 157–180. Available: https://doi.org/10.1179/imtr.1985.30.1.157 [Accessed 20.09.2022]

Vasco-Olmo, J.M., Díaz, F.A., Antunes, F.V., & James, M.N., 2019. Characterisation of fatigue crack growth using digital image correlation measurements of plastic CTOD [online document]. Theoretical and Applied Fracture Mechanics, Vol. 101, pp. 332 – 341. Elsevier Ltd. Available: https://doi.org/10.1016/j.tafmec.2019.03.009 [Accessed 18.10.2022]

Wallin, K., 2011. Fracture Toughness of Engineering Materials – Estimation and Application. Warrington, UK: EMAS Publishing, 543 p. ISBN 0-9552994-6-2, 978-0-9552994-6-9

Wallin, K., Pallaspuro, S., Valkonen, I., Karjalainen-Roikkonen, P., & Suikkanen, P., 2015. Fracture properties of high performance steels and their welds [online]. Engineering fracture mechanics, vol. 135, 2015, pp. 219 – 231. Elsevier B.V. Available: https://doi.org/10.1016/j.engfracmech.2015.01.007 [Accessed 07.10.2022]

Wang, C. H., 1996. Introduction to Fracture Mechanics [online document]. Melbourne, Australia: DSTO Aeronautical and Maritime Research Laboratory. DSTO-GD-0103. Available: https://doi.org/10.13140/RG.2.1.1444.2408 [Accessed 08.03.2023]

Wang, C. H., 1996. Engineering library, Plastic Yielding at Crack Tip [online document]. Engineering library.org. Available: https://engineeringlibrary.org/reference/fracture-mechanics-plastic-yielding-at-crack-tip [Accessed 08.03.2023]

Wciślik, W. & Pała, R., 2021. Some Microstructural Aspects of Ductile Fracture of Metals [online document]. Materials 14: MDPI Available: https://doi.org/10.3390/ma14154321 [Accessed 22.09.2022]

Wiednig, C. & Enzinger, N., 2017. Toughness evaluation of EB welds [online document]. Welding in the World, Vol. 61, pp. 463 – 471. Available: DOI: 10.1007/s40194-017-0422-4 [Accessed 17.10.2022]

Wulpi, D.J., 1999. Understanding how components fail – 2nd edition. Ohio, US: ASM International, 293 p. ISBN: 0-87170-631-8

Zhu, X.–K., and Joyce, J. A., 2012. Review of fracture toughness (G, K, J, CTOD, CTOA) testing and standardization [online document]. Engineering Fracture Mechanics, Vol. 85, 2012, pp. 1 – 46. Available: https://doi.org/10.1016/j.engfracmech.2012.02.001 [Accessed 17.10.2022]